Author: Janssen, Kjeld G.H.
Title: Nanofluidic tools for bioanalysis : the large advantages of the nanoscale
Issue Date: 2013-12-19

Nanofluidic tools for bioanalysis: The large advantages of the nanoscale

Proefschrift

ter verkrijging van
de graad van Doctor aan de Universiteit Leiden,
op gezag van de Rector Magnificus prof.mr. C. J. J. M. Stolker,
volgens besluit van het College voor Promoties
te verdedigen op donderdag 19 december 2013
klokke 8:45 uur

door

Kjeld Gertrudus Hendrikus Janssen
Geboren te Nijmegen
in 1979

Promotiecomissie

Promotores:

Prof.dr. Thomas Hankemeier
Prof.dr. Jan C.T. Eijkel

Co-promotor:

Dr. Heiko J. van der Linden

Overige leden:

Prof.dr. Meindert Danhof (LACDR, Universiteit Leiden)
Prof.dr. Gert Desmet (Free University of Brussels, Belgium)
Prof.dr.ir. Johannes G.E.M. Fraaije (LIC, Universiteit Leiden)
Dr. Sumita Pennathur (University of California Santa Barbara)
Dr. Niels R. Tas (MESA+, Universiteit Twente)
Dr. Paul Vulto (LACDR, Universiteit Leiden)

The research described in this thesis was performed at the Division of Analytical Biosciences of the Leiden Academic Center for Drug Research, Leiden University, the Netherlands

This research has been financially supported by NanoNed and the Netherlands Metabolomics Centre.

Nanofluidic tools for bioanalysis: The large advantages of the nanoscale
Kjeld G. H. Janssen
PhD Thesis Leiden University with summary in Dutch
ISBN/EAN `978-90-74538-80-0`

Typeset by $\LaTeX\,2_\varepsilon$
Printed by Drukkerij te Sligte B.V., Enschede (2013)

Front cover artist: Gilberto Gennero
This cover is an artist's impression of the sepration technique dz-ITP (Chapter 4 of this thesis), indicating a microchannel with 4 concentrating analytes in front of a barrier created by the presence of a nanochannel. The graph below is from actual data, showing the time evolution of this process. This image was also selected as the cover of the journal *Analytical Chemistry* in which Chapter 4 was published.

Voor mijn ouders

Contents

CHAPTER 1

Introduction and Outline

In this thesis new and miniaturized bioanalytical tools for the life sciences are presented. Two interrelated paths are described in this introduction: on one hand how metabolomics can have an important impact in drug development and treatment, and why this requires the analysis of sample volumes as small as those from single cells. To analyze these minute sample volumes, new separation and detection methods are reported in this thesis: isotachophoresis in nanochannels, depletion zone isotachophoresis, and a surface enhanced Raman spectroscopy sensor. On the other hand, working with nanochannels, has led to the discovery of new unexpected fundamental phenomena, also reported in this thesis for the first time: in nanochannels acidification of buffer solutions up to 1 mol/L occurs, and extreme pressures $>$ 1000 bar can be induced. This introduction provides the rationale, concepts and terms as well as (theoretical) background for this research.

Section 1.1 introduces the potentially large impact of the systems biology approach, and metabolomics in particular, on drug research and treatment. In section 1.2, a gap is identified between the requirements of metabolomics and current separation and detection methods, to analyze samples as small as an aliquot of a single cell. Miniaturization of equipment platforms including Lab-on-a-Chip, are also discussed. A potential solution to bridge this gap is discussed in section 1.3, namely the use of nanochannels for further downscaling. Special properties and challenges in the use of nanochannels are described. Section 1.4 describes electrophoretic separations, which are compatible with minute volume analysis, particularly isotachophoresis. The principles of the new technique of depletion zone isotachophoresis are also described. Section 1.5 explains the optical detection technique of surface enhanced Raman spectroscopy, a technique compatible with the minute volumes and low abundance at which analytes of interest occur in minute samples. The goal and outline of the thesis are described in section 1.6.

1.1 Systems Biology, a new approach in drug research and treatments

In conventional drug research the target for an intervention was often reduced to a single receptor or pathway, which was then modulated with a drug. Although successful for various diseases in the past, this reductionist approach has not proven sufficient to tackle more complex diseases such as cancer[1], multiple sclerosis[2], migraine[3] and rheumatoid arthritis[4] and osteoarthritis[5]. The complexity of these diseases is attributed to the involvement of many pathways and multiple potential targets. This is reflected in not fully understood efficacy variations and various side-effects when studying a group or population of patients when using one single pharmacologically active compound. In drug development, this increases the risk of failing the demanded validation studies in a late stage, as even for an active compound which initially may look promising the efficacy in a wider population is much harder to predict. This higher risk of drugs that will not reach the market and return their investment, directly results in increasing drug development costs. In turn, this makes it less attractive to develop new drugs, so that in the end fewer new drugs reach the market[6]. A new approach to drug research is therefore critically needed.

In answer to this need, the vision of systems biology has recently gained momentum[6]. In contrast to the reductionist approach mentioned in the previous paragraph, the philosophy of systems biology suggests a holistic approach: if the relevant multiple biological processes and their interplay involved are mapped, the disease mechanism can be better understood. In a drug development approach, when starting from a systems perspective, better efficacy and toxicity predictions are expected, resulting in an increase in drug development research efficiency, and corresponding decrease in costs; this approach was recently termed systems pharmacology[7,8].

Another important contribution to what makes a treatment intrinsically complex are differences between individual patients, in genotype and from environmental changes during development. As a consequence there is a variation in efficacy between individuals, affecting not only the development of new treatments, but the application of many existing pharmaceutical treatments as well. A drug might not be effective for certain patients while in yet others it may require a different dosage, be ineffective, or induce unexpected side effects that may even be severely harmful. The treatment of rheumatoid arthritis in the Netherlands is an example of this current approach where the same regime is applied to all patients: first the common drug methotrexate is applied. When not effective in disease modification, the dosage is increased and other drugs (sulfasalazine, leflunomide or hydroxychloroquine) are tried. When still not effective a combination of several drugs is tried (abatacept, rituximab or tocilizumab), before finally drugs of a new generation called biologicals (one of the TNF-alpha blockers) are applied[9]. This trial and error process can take many months, with potentially no improvement in patient condition or unnecessary worsening of the disease and additional patient suffering. This again demonstrates the need for a more direct, evidence-based way for selecting the proper pharmaceutical interventions, to maximize efficacy and minimize side effects, in the clinical practice for the individual[4].

A more direct evidence-based approach can be provided by the systems-biology approach, not only providing indicators for the disease state that can be monitored during treatment of the individual, but also those that provide an early warning before the actual onset of the disease. This accelerates the process of treatment optimization, to the benefit of the patient. First results have for example identified indicators that predict efficacy of rheumatoid arthritis medication[4] in individuals. This case illustrates how the benefits of the systems biology approach need not be limited to the development of new drugs, but can also contribute to the prediction of the efficacy of many existing pharmaceutical treatments. The concept of tailoring a treatment to the individual patient is called personalized medicine[10].

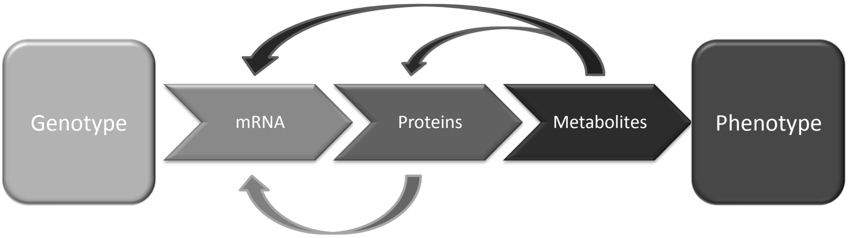

Figure 1.1 Schematic view of systems biology components. This very simplified model shows how genetic information within the DNA is transcribed into messenger RNA (mRNA), which is translated into peptides and proteins, which in turn work among others as catalysts in catabolic and anabolic pathways. The set of all metabolites therefore is an important contributor to the phenotype. In practice this system is much more complex as transcription from the genome is in turn regulated by metabolites, peptides, proteins and mRNA and vice versa. Whereas the genome, in combination with the environment during development, contributes to the phenotype on a lifetime scale metabolites reflect the actual phenotype on time scales from days to sub-second[11].

Figure 1.1 shows a schematic of the major molecular levels of a biological system and their intricate relations. It shows the intermediate steps between the genotype or genome, the collection of genes of the organism, towards the phenotype. An organism's phenotype is the complex of its observable characteristics, from shape down to sub-second variations in chemical composition. This includes the aspects of health and disease. The interplay between genes, transcripts, proteins and metabolites contributes to this phenotype, providing an indication why diseases can be very complex. The relationships presented in Figure 1.1 illustrate the challenges involved in making the systems biology vision for drug development and personalized health a reality as it requires understanding of many of its mechanisms.

Several parts of the biological system have been extensively studied in previous decades. Enormous progress has been made in the field of genetics, with the human genome now being available. Genes determine lifelong effects such as eye color and are strongly related to the propensity to develop some diseases, including cancer and hereditary diseases. For proteins enormous progress has been made in the understandings of their workings. The understanding of the complex interplay between genes and their transcripts however, remains incomplete. At the other end, an organism's biochemical state on day and shorter time scales, is predominantly reflected in its metabolic state (see Figure 1.1). The entire composition of all metabolites, which includes all small molecules which are intermediates and products of metabolism, is called the metabolome. The metabolome includes communication and regulation compounds such as hormones, neurotransmitters and central energy/carbon metabolites such as adenine triphosphate (ATP). Studying the metabolome as a whole is a relatively new field, whereby the comprehensive quantitative and qualitative analysis of the metabolome is called metabolomics[11,12].

Metabolomics is attractive for the evaluation of disease states for two reasons. Firstly, the metabolome reflects the organism's homeostasis, the property of a system to maintain a stable condition and to withstand challenges and perturbation. The metabolome represents an important part of the organism's phenotype as a whole including down to the cellular level, and on a time scale including days down to sub-seconds. This makes the metabolome an attractive indicator for monitoring the influence of medical treatment in personalized health. Secondly, as indicated in Figure 1.1, the metabolome is not only closest to the phenotype, but transcription and protein synthesis are also partly controlled through metabolites. In conclusion, the metabolome is in a unique position to provide an indicator for an individual's health state. Making metabolomics available as a tool for diagnosis of diseases and the prediction of treatment outcome, and thus also enabling personalized health strategies, is the main goal of the research at the Division of Analytical Biosciences (Leiden, The Netherlands) and the Netherlands Metabolomics Centre (NMC). Of course, on the longer term, integration of all available data at different "-omics" levels can only further improve the diagnosis and prediction of the disease outcome.

1.2 Equipment in metabolomics and the impact of miniaturization

1.2.1 Technological challenges in metabolomics measurement equipment

This subsection describes some of the technological challenges in metabolomics research in general, but with the emphasis on minute volume analysis. Discussed is why the field of metabolomics, despite its vast potential, is less far developed than genomics (genome analysis) and peptidomics (protein analysis).

First of all, due to the huge variety in physicochemical properties of metabolites, a full metabolome analysis with a single method or technique is currently not feasible. Today, a full metabolome analysis uses several platforms and takes up to 1-3 hours per sample. Profiling of only the major metabolites in samples where enough volume is available with NMR is faster, and takes only up to 10 minutes per sample. This stands in contrast with genomics, where the target, DNA, is physicochemically relatively homogeneous and can be measured and quantified by e.g. gel electrophoresis. In metabolomics, multiple methods, differing in sample pretreatment, separation and detection are needed. Arguably the result of metabolomics in health and disease may identify clusters of compounds which represent a single biomarker, so that not the entire metabolome needs to be analyzed.

Secondly, in metabolomics there is a large variation in relative abundance of metabolites, and in addition these are found in different compartments and matrices[12]. Metabolomics requires comprehensive analysis of metabolites in different matrices in the organism, from the whole body (e.g. blood), down to organs, tissues and ultimately individual cells. In drug research, an important example of the relevance of metabolomics on the smaller compartments tissues and single cells), is cancer, a disease which may include (highly) differentiated cells. This makes treatment difficult or a cure impossible, unless understanding of processes on the cellular level is included. The variation in matrices presents a huge analytical challenge. An indication of the sample sizes involved on the various levels from organism to sub-cellular level is illustrated in Figure 1.2. In comparison, in DNA analysis the challenge of low amounts has been eliminated by the polymerase chain reaction (PCR), now widely available, which can amplify DNA from even a single cell or one fragment, to detectable amounts. This has contributed to the fact that the entire human genome is now known. At present next generation sequencing has even become available, lowering the time and costs for the analysis of a whole genome significantly further.

Thirdly, to make optimal use of metabolomics, monitoring or time-resolved analysis of the (fast) metabolic processes is highly desirable. If one wants to take longitudinal samples of the same system, the amount of sample and the way in which it is obtained should not be of significant influence to the system. This would not be possible in single-cell genomics where it would simple mean removal of the cell's DNA, killing it.

Fourthly, the amount of information itself and the requirements on analysis and elucidation of the correlations places a high demand on data-analysis in terms of new techniques and computational power. These challenges fall beyond the scope of this thesis.

Note that the first three challenges mutually reinforce the requirements for low sample volume and corresponding small amount of analyte: particularly cells and tissues have a minute volume to begin with, the minimal disturbance needed for a longitudinal analysis constrains the volume that can be sampled and the need for multiple methods can necessitate splitting of this volume. Arguably, in a significant portion of future metabolomics applications, in drug development and personalized medicine, is not expected that a full metabolome analysis of single cells is required. For example, a blood sample may suffice, or a set of biomarkers as a group forms an adequate biomarker, and the technical challenge is correspondingly less. Regardless of the potentially large impact of single-cell metabolomics in the future, it is presently in its infancy with first results of whole cells being published in recent years[13–15] but developing very rapidly as reviewed elsewhere[16]. In conclusion, to establish the potential of longitudinal single cell metabolomics requires integrated analysis methods that can work with minute amounts of analyte.

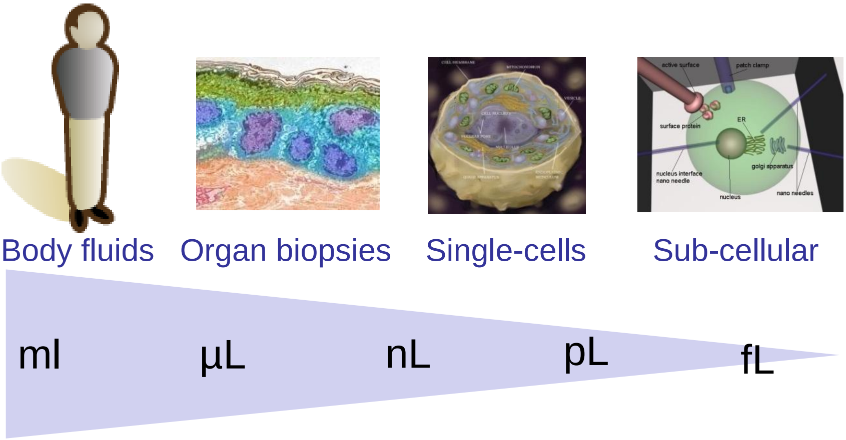

Figure 1.2 Overview of the sample volumes involved in bioanalysis of the various organism compartments. The sample volumes are indicative of the amount that can be extracted without disturbing homeostasis.

1.2.2 Current equipment in metabolomics, separation and detection

Standard analysis methods in metabolomics currently comprise sample preparation, usually followed by separation, and detection/identification of the metabolites of interest, or of all metabolites detectable with a certain method. Usually, methods require 10,000 or more cells, or a few microliters of sample. However, some methods can detect metabolites in principle also in smaller samples, as is shown in Figure 1.4. Current methods for metabolomics are discussed below, particularly their compatibility with minute volume analysis and low absolute amounts of analyte, as needed for analysis down to single cells.

Conventional liquid chromatography (LC) is one of the most commonly used separation techniques in metabolomics, as it is applicable to a wide range of compounds and volumes (although volumes greater than of few tens of microliters are predominantly used in preparative and/or purification applications). The separation mechanism is based on the difference in distribution per analyte, between a stationary phase and a mobile phase[17]. Standardization and a high level of automation of this method is available, making the method relatively easy to implement. The extensive range of LC equipment commercially available includes LC columns, automated systems and standard interfacing with detection instruments and analysis software. Miniaturization of particle sizes in chromatography enables improved resolving power. In order to apply the same linear flow rate as for larger particles[17] however, higher pressures are required, posing a challenge for interfacing and necessitating more powerful pumps. The limits for downsizing of particle sizes are currently about 1 µm. Sample sizes on the order of tens of nanoliters can be analyzed with sufficient sensitivity by miniaturizing also the column inner diameter as demonstrated by nano-LC (Figure 1.3) which uses minute columns and commonly uses small particle sizes[17,18]. Open tubular LC in nanochannels may provide higher separation power[19–21], but experimental challenges limit this technique at the moment to a few specialized research labs.

Electrophoretic separation techniques are compatible with a wide range of sample volumes, and are predominantly utilized in the capillary format[17]. Their separation mechanisms are based on the difference in migration speed of ions in a matrix, e.g. a solvent or gel, under influence of an electric field. Since many metabolites are charged, electrophoretic separation can be applied to a wide range of compounds. Electrophoretic techniques, such as capillary zone electrophoresis (See Section 1.4), also provide significantly higher resolving power compared to most chromatography based techniques[17]. This is due to the absence of several factors that contribute to peak broadening in most LC approaches: 1) Capillary zone electrophoresis (CZE) takes place in an open capillary, whereas in conventional LC the liquid travels in many parallel paths which differ in velocity past the particles. 2) Bulk flow in LC is provided by pressure which has a parabolic flow profile, which contributes to peak broadening, whereas electro-osmotic flow in electrophoretic techniques has a flat flow profile. The downscaling of pressure-driven methods is challenging due the correspondingly higher pressures needed. This requires pumps that can supply the higher pressures precisely and robustly, and imposes higher demands on pressure resistance of connections and injection methods. Although commercially available, these systems are not standard and more expensive. Contrary to LC, implementation of miniaturized CE separations only requires a smaller cross-section while most other experimental conditions and equipment can remain the same. However, the consequences for detection (Figure 1.4) are not straightforward due to the decreasing analyte amounts and are considered separately in section 1.2.3. Furthermore, miniaturization has been shown to improve electrophoretic techniques, predominantly because it allows the use of higher field strengths. Downscaling causes a reduction in heat generation, where heat can cause bubble formation in the liquid and gradients of physicochemical properties in a capillary resulting in band broadening. Higher field strengths also enable faster separations with improved efficiency, as the dispersive effects from diffusion become smaller[17]. Electrophoretic techniques are therefore more suited for metabolomics of ultrasmall samples than LC as they provide the small volume compatibility and resolving power required.

Despite the advantages of electrophoretic techniques over LC, CZE as the most applied electrophoretic technique remains far less popular than LC due to several disadvantages, of which the following two are considered the most relevant: 1) in CZE, by nature of the separation mechanism, each analyte zone arrives at the detector at a different speed, affecting the observed length of the zone. The migration velocity is very sensitive to changes in temperature ($\approx$ 1-2% per degree Celsius[22]), making quantitative analysis and identification[a] more challenging compared to LC, where the flow speed can be set constant. 2) CZE is performed in capillaries and small channels to prevent excessive heating. Although the compatibility with small volumes can be considered an advantage of CZE, this also proportionally reduces the loadability, when not hyphenated with preconcentration techniques, considered a drawback as it challenges detection for dilute analytes. Fortunately, the powerful electrophoretic technique of isotachophoresis suffers neither of these disadvantages, as detailed in section 1.4.2.

Figure 1.4 shows the most common detection techniques used for metabolomic analysis and an indication of their compatibility with smaller peak volumes, which are obtained when downscaling analytical methods. NMR is often used for profiling of the most abundant metabolites without prior separation, and for identification of (often isolated) compounds[12]; it is currently not suited as a fast online or inline detector for the profiling of low-concentration metabolites in a wider set of samples due to among others a lack of a sufficiently robust in-line interface. Mass spectrometry (MS) is the most generic detection technique, as MS can selectively detect a wide range of metabolites with good sensitivity. Furthermore, high resolution MS supports identification of the detected metabolites via determination of the elemental composition, if the mass resolution of a compound is high enough;

---

[a] Conventionally, e.g. in CE-UV, peak area is used in quantification and as slower zones are seen as broader peaks, experimental variations in speed likewise affect quantification accuracy[22].

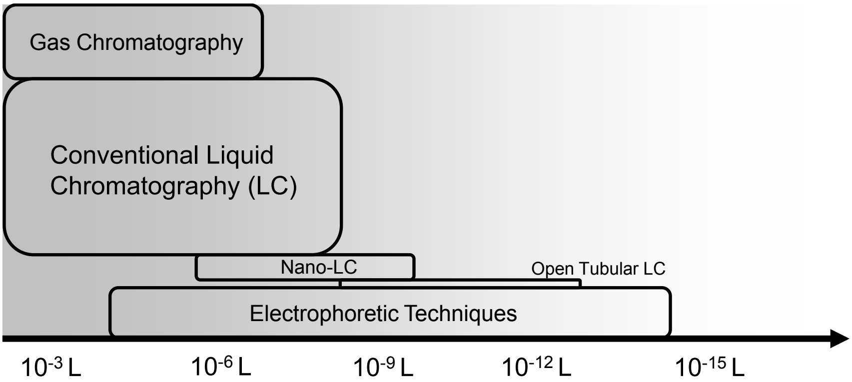

Figure 1.3 Typical separation techniques in metabolomics and the sample volume range in which they can be operated under optimal conditions. On the abscissa an estimate of the possible sample volume is given at which a method can be used with good performance whereas the height provides a tentative indication of how extensively the technique is presently used.

identification is further supported by controlled fragmentation of compounds and determining the elemental composition of these fragments. MS can be used as in-line detector with GC, LC, nano-LC and many electrophoretic techniques including capillary zone electrophoresis (CZE)[12]. Not surprisingly therefore, mass spectrometry is the most used detection technique in metabolomics. Conductometry, measuring the local conductance of the eluate, is non-specific and provides relatively poor detection limits. Amperometric detection is very sensitive but only for a select few electroactive metabolites such as dopamine[23]. Fluorescence detection is very specific and highly sensitive, most metabolites however requires labeling however, and when combined with laser illumination, detection limits down to single molecule can be provided for a selected few compounds[24].

1.2.3 Miniaturization of analysis methods & instruments: advantages and challenges for metabolomics

Halfway the 1970's, technology from the semiconductor industry made it possible to machine channels with dimensions on the order of micrometers. This enabled the downscaling of analysis platforms, with one of the first examples being a gas chromatograph scaled down to a single chip, composed of minute channels in 1979[25]. It was recognized that integrated fluidic microchannel structures, so-called microfluidic chips, enabled a hitherto unprecedented control of minute volumes of liquids[26,27] Microfluidics has since developed into a still expanding interdisciplinary research field characterized by the use of fluidic channels with dimensions on the order of micrometers. The growth of this research field was stimulated because the significant benefits towards bio-analysis were recognized early on. Obviously the intrinsic small size of the platform allows the

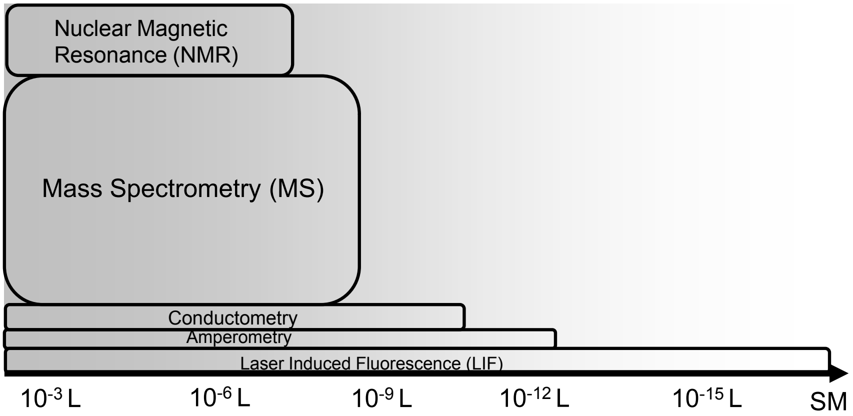

Figure 1.4 Detection methods in metabolomics and the optimal peak volume at the detector, i.e. the volume in which a peak introduced into the detector can be well measured. It should be noted that the peak volume is not the same as the sample volume, but can be smaller or larger. On the abscissa an estimate of volume compatibility is given down to the single molecule (SM) level, whereas the height provides a tentative indication of the applicability or current use of the technique for metabolomics.

manipulation of liquid volumes on the order of several microliters down to nanoliters, greatly reducing reagent use and sample sizes correspondingly. Even more important, networks of these channels in a so-called microfluidic chip allow the integration, automation and standardization of complex methods in a single fluidic chip. This so called Lab-on-a-chip concept can in principle improve speed, robustness and operator-friendliness of analytical methods. Using advanced microfabrication techniques, very complex devices can be made allowing a high degree of fluidic control[28,29]. Lastly, in combination with an in-line detection method a complete miniaturized analysis platform can be realized, a so-called micro total analysis system (µTAS).

In general, miniaturization poses a challenge to the sensitivity of most detection techniques. A detection method is needed that is suitable for low amounts of molecules, and applicable in-line with micro- or even nanochannels. For the larger microfluidic systems, MS interfacing meets most detection needs[12], although it has to be mentioned that mass spectrometry as yet has not been miniaturized successfully to the footprint of the above mentioned liquid-manipulation and separation modules. Conductometric detection is also often encountered in microfluidics, as the required electrodes can be built into the chip, thereby fully integrating the detection[30]. Laser-induced fluorescence (LIF) detection has so far been the method of choice for most microfluidic and nanofluidic systems because of its excellent detection limits[24], and its ease of use as an in-line detector in combination with transparent chips (e.g. glass). Unfortunately most metabolites require fluorescent labels, necessitating the integration of a successful labeling step. Also only a limited amount of different labels can be used, making LIF less suited for metabolomics profiling. Surface enhanced Raman spectroscopy (SERS) is an optical detection technique that provides specificity for unlabeled (bio)molecules in the form of vibrational signature spectra, and for a few compounds single molecule detection limits have been reached[31] (see section 1.5). These advantages over other detection techniques such as LIF make SERS attractive as a detection technique for miniaturized analysis in e.g. metabolomics. Unfortunately, SERS is currently not compatible with in-line detection, due to irreversible binding of analytes to the SERS surfaces, a challenge addressed in Chapter 5.

Microfluidic separations have been applied to DNA fragments, proteins and metabolites[32–36]. Notable commercially available bio-analytical platforms based on microfluidic chip devices include the Agilent® 2100 Bioanalyzer for the analysis of DNA, RNA and proteins. The company Fluidigm® provides a chip platform for single cell gene expression, targeted DNA sequencing, DNA polymerase chain reaction (PCR) and for protein crystallization[29]. On the field of personalized health a lab-on-a-chip platform was developed by Medimate®, which enables the measurement of the pharmaceutical agent lithium in a drop of blood, in a few minutes, by patients themselves[30].

In section 1.2.1 the technological challenges for different types of metabolomics analyses were identified: the needs were stipulated for smaller volume analysis, integration of multiple methods, increased speed and/or cost reduction. In principle, miniaturization holds the promise to address all these aspects. Microfluidics provides minute sample compatibility, ease of use, automation and standardization. Particularly electrophoretic techniques were identified to be well suited for miniaturization, and in addition, downscaling may even improve the resolving power of electrophoretic techniques.

1.3 Nanofluidics

1.3.1 Nanochannels in separation science

The final frontier of miniaturization is the use of channels with at least one dimension smaller than a micron, so-called sub-micron channels or nanochannels. Nanochannels may ultimately approach the dimension of a water molecule (3 Ångström), and are studied in the field of nanofluidics[37–42]. Nanochannels have been made possible by means of technology translated from the semiconductor industry[43], with an example given in Figure 1.5. Integration into a fluidic chip yields a promising analysis platform, capable of liquid manipulation on the picoliter to femtoliter scale. This provides a means to handle and manipulate minute biosamples as required for single-cell and sub-cellular analysis (Figure 1.2). So far, liquid chromatography[44,45] and zone electrophoresis[46,47] have been successfully demonstrated and studied in a nanofluidic environment. The advantages of downscaling electrophoretic separations in microchannels also apply to nanochannels[42] as detailed in section 1.4.3.

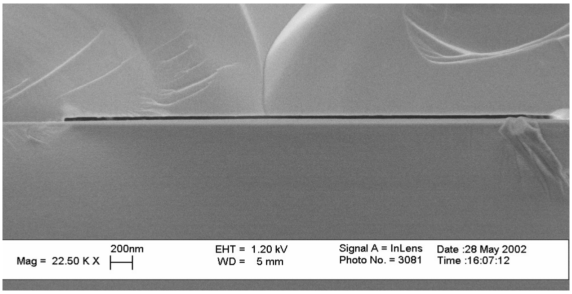

Figure 1.5 Scanning electron microscopy image of a cross-section of a nanochannel. The channel is 40 µm wide and 50 nm in depth[43].

Nanochannels however, are not just smaller channels. Due to their high surface-to-volume ratio, surface effects are more pronounced or even dominant compared to the liquid[37–41], with the most relevant phenomenon being related to the electrochemical double layer (EDL)[48]. This EDL is theoretically detailed in Chapter 2 of this thesis. The influence of surface effects on electrophoretic separations is discussed in the introduction of Chapter 3. The increased relevance of these surface effects differentiates nanofluidics from microfluidics, creating unique challenges and opportunities, making chemical analysis in nanochannels an exciting and fruitful field of research.

1.3.2 Nanofluidic concentration polarization

The concentration polarization effect, is a good example of a unique opportunity offered by the use of nanofluidics in Lab-on-a-Chip devices. It forms the basis of the novel separation technique depletion-zone isotachophoresis, described in chapter 4 of this thesis. Concentration polarization is known from the field of membrane physical chemistry and nanochannels function as a single membrane pore to cause concentration polarization. Since its first demonstration at a micro-nanochannel interface by Pu et al[49], concentration polarization has been studied by several groups[39,50,51]. In Figure 1.6 the principle is schematically shown. In a nanochannel the countercharge from the walls in the double layer provides a significant contribution to the total amount of ions in the solution, shifting the ratio between co- and counter-ions. Under an applied electric field the asymmetric conduction by positive and negative ions induces the effect of concentration polarization. The charge asymmetry in the nanochannel as a function of ionic strength and pH, and hence the amount of ions depleted per unit current at its interfaces with a microchannel, is described by a model in Chapter 2.

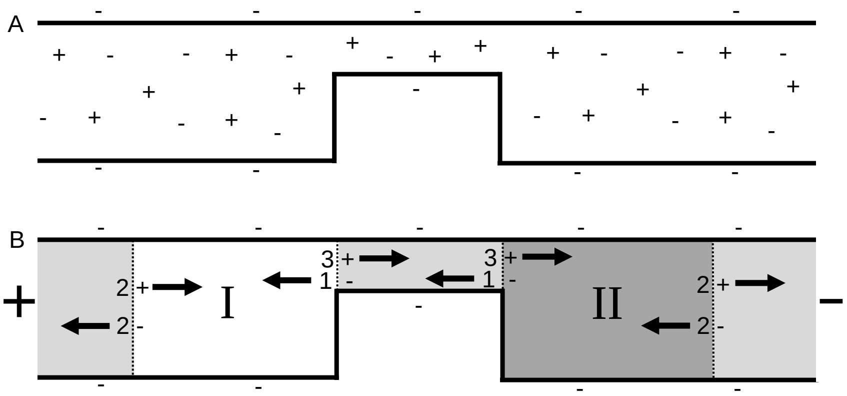

Figure 1.6 Principle of concentration polarization. Depicted is a nanochannel that connects two microchannels. The surface charge is in this system is negative. A) The system is filled with a solution of a monovalent salt. In the narrower nanochannel the counter ions of the surface charge significantly contribute to the total amount of ions in the solution, yielding a positive to negative ion concentration ratio of 3:1 in the solution. In the microchannel the contribution of the surface charge contribution is negligible and the ratio is 1:1. B) Under application of an electric field a current of 4 elementary charges per unit time is carried by negative and positive ions equally in the microchannel. In the nanochannel the asymmetric distribution of ions results in a correspondingly asymmetric charge transport. Summation of the ions transported in region I yields a net result of 1 salt ion pair being depleted per time unit. In zone II the net result is the enrichment by one salt ion pair per time unit. Over time the net effect of this charge asymmetry in the nanochannel leads to expanding depletion and enrichment zones

1.4 Electrophoretic separation techniques

1.4.1 Principles of electrophoretic techniques

Electrophoretic separation is based on the migration of ions in liquids effectuated by an applied electric field, a principle established by Friedrich Kohlrausch in 1897[52]. Each ionic species i has a different velocity, v_i, in an electric field, E, according to its electrophoretic mobility μ_i:

$$v_i = qE/6\eta\pi R = \mu_i E \tag{1.1}$$

with q the charge of the ion and R its effective hydrodynamic radius in a liquid of viscosity η. The most straightforward separation technique that exploits the difference in μ_i of each ion is zone electrophoresis (ZE)[17]. In capillary-ZE (CZE), a sample is injected at the inlet of a capillary, commonly by pressure; next, under influence of a subsequently applied electric field each ionic species migrates at a velocity according to its mobility. Detection of the separated ions can be performed with optical methods along the capillary or at the capillary end with for example mass spectrometry or electrochemical detection[17].

Electrophoretic techniques are particularly suited to miniaturization[32–35] as they benefit amongst others from improved heat dispersion as already described above. Electrophoretic separation techniques that have been successfully applied in microchannels include zone electrophoresis, iso-electric focusing and isotachophoresis (ITP)[32–35]. With the advent of nanochannel fabrication technologies[43] the nanofluidic domain is receiving increasing attention. So far, zone electrophoresis[46,47] and isoelectric focusing have been successfully demonstrated in a nanofluidic environment[46,47]. Despite the benefits the use of nanochannels is less popular than the use of microchannels, although the advancement of fabrication techniques has mostly closed the gap with microchannels. Arguably this is due in part to detection limits becoming a limiting issue, while also for many applications downscaling further than microfluidics is not necessary. An expansion towards nanofluidic technology in future applications is expected for the analysis of metabolites or other biomolecules in individual cells or even smaller, in organelles.

1.4.2 Isotachophoresis

Isotachophoresis is an electrophoretic separation technique that also provides the advantage of focusing[53–56]. Isotachophoresis is effectuated by placing the sample (consisting of diluted analyte ions) next to a zone of fast ions of high concentration (the leading electrolyte, LE) and applying a voltage difference. As a consequence the sample ions undergo isotachophoretic focusing and separation as detailed in Figure 1.7. After some time an equilibrium is achieved when all ions move at the same velocity (Figure 1.7B), hence the name iso-(same)-tacho-(speed)-phoresis (migration). At equilibrium the analytes will have reached a concentration C_i, the so-called plateau concentration, related by a factor k to the LE concentration, C_{LE}:

$$C_i = kC_{LE} \tag{1.2}$$

The factor k depends among others on the mobility of the analyte and the co- and counterion mobilities in the leading electrolyte.

Isotachophoresis concentrates a sample zone containing a mixture of analytes at low concentration into a sequence of concentrated zones of these ions. In conventional ITP, a second electrolyte is added behind the sample, chosen to have ions with a lower mobility than those in the sample, a so-called trailing electrolyte (TE), as detailed in Figure 1.8. The LE is chosen to have a concentration as high. and the trailing as low as practical, for instance as reported by Jung et al[57]. These authors used 1 mol/L NaCl as LE and 5 mmol/L HEPES, pH 5.3 as TE, demonstrating a concentration increase by a factor of 2 million. The added benefit of a high concentration LE, besides causing a very high final plateau concentration for analytes, is that the voltage will drop predominantly over the sample and trailing zone, and the correspondingly high local field will maximize the focusing speed.

When available in sufficient amounts, a maximum concentration is reached and analytes are separated in neighboring zones, in so-called plateau mode ITP.

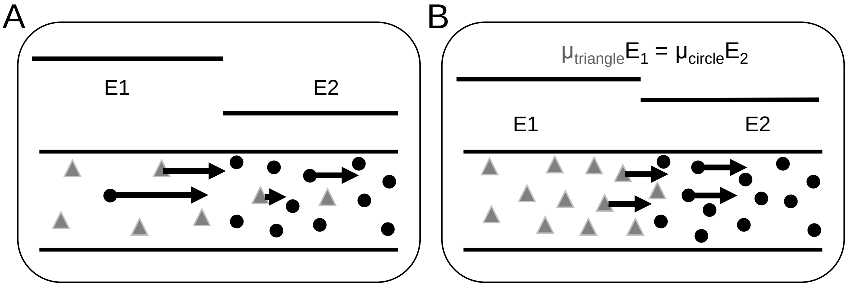

Figure 1.7 Principle of isotachophoresis. A) Sample ions (triangles), are positioned next to a high concentration of co-ions (ions with the same charge sign) of the leading electrolyte (LE), selected for having a higher electrophoretic mobility (counter-ion contributions are neglected). The electric fields in each zone induces migration velocities (Eq 1.1) as schematically depicted by the arrows. The sample ions move faster in the sample zone than the leading ions in the leading zone, as the concentration of leading ions is higher, and therefore the local conductivity higher and the field strength lower. Consequentially the sample ions increase in concentration at the interface which sharpens. B) In equilibrium (after migrating further along the channel) the ion velocities have normalized, with the sample ions having reached their plateau concentration, and a corresponding electric field is reached (Eq 1.2).

The plateau concentration depends amongst others on the concentration of the leading electrolyte (LE), (see Eq 1.2) and the mobility of the analyte[53–56]. In conventional separations the resolution between analytes is expressed as the distance between the, assumed Gaussian distributed, peaks relative to a measure of their width. In ITP however zones always partially overlap, in the form of a diffused zone, and the ability to distinguish trace analytes in their individual zones depends on the length of a zone, relative to their interfaces. Therefore, resolving power in ITP can be expressed in terms of the length of the plateau zone normalized by the characteristic length of diffused zone[58–60]. Since the length of a plateau zone is proportional to the absolute amount of trace analyte, the separation efficiency of ITP in equilibrium is also proportional to the absolute amount of analyte. Note that this makes the resolving power in ITP independent of the initial analyte zone width or the sample volume, as opposed to for instance zone electrophoresis.

If not enough absolute amount of analyte is present, the plateau concentration is not reached, and analytes focus as peaks (so-called peak mode ITP) which may partially or even completely overlap with neighboring peaks or zones[58].

1.4.3 Benefits of the miniaturization of isotachophoresis

ITP particularly benefits from miniaturization, as the length of the ITP plateau zones, which are a measure of resolving power, increase proportionally with decreasing channel cross-section, if the amount of analyte is kept constant, as described extensively by Bagha et al[60]. This inherent downscaling benefit originates

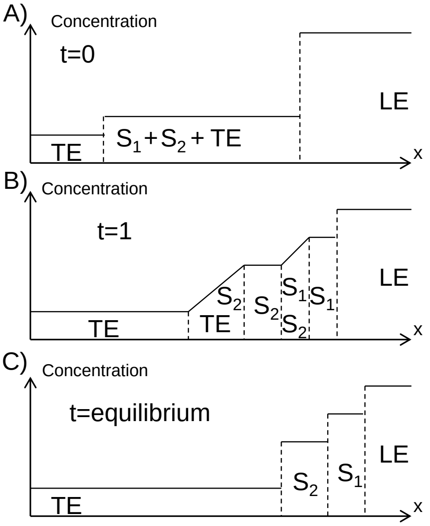

Figure 1.8 ITP focusing over time for two analytes. Assumed is a minimal EOF (not shown), so that displacement (towards the right) is due to net migration. Assuming ground at the origin, this figure is equally applicable to describing ITP for positive analytes and a negative potential at x or the reverse. The E field is inversely proportional to the concentration (not shown here, but for reference see Figure 1.7). A) Initial state. The sample analytes, assumed dissolved in trailing electrolyte, are interposed between leading electrolyte (LE) and trailing electrolyte (TE) B) After application of an electric field along the axis of the separation channel, focusing is ongoing. Part of the sample ions S_1 and S_2, have reached their plateau concentration (Eq 1.2), but full separation is not complete. C) ITP in equilibrium, with the analytes fully focused and resolved.

from the fact that ITP is a concentration-driven focusing technique that focuses up to a plateau (Eq 1.2); in smaller cross-sections therefore a smaller amount of analyte is needed for the same concentration per length. Or phrased differently: the same amount of analyte forms a longer zone illustrated in Figure 1.9 . Optimal use of this advantage is made in case of low abundant analytes and if the detector is concentration sensitive. In case of detectors sensitive to the absolute amount per cross-section, better detection limits are achieved with larger cross-sections (e.g. a longer path length in optical detection), but the poorer separation requires that the detector is capable of distinguishing simultaneously arriving compounds.

An important proof-of-principle of ITP downscaling has been given by Walker et al.[61], who were the first to demonstrate ITP in a microfluidic device. Many applications of ITP in the microfluidic chip-platform have been reported since, as extensively reviewed elsewhere[33,62–64]. Jung et al. reported concentration factors of up to a million times, achievable due to downscaling to microfluidic dimensions[57]. Isotachophoresis in nanochannels is assessed for the first time in Chapter 3 of this thesis, for the purpose of ultra-small sample analysis such as that from a single cell.

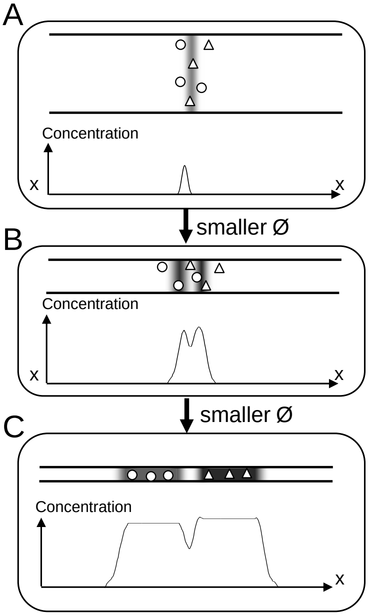

Figure 1.9 Theoretical schematic of the effect of downscaling the channel cross-section on the resolution of ITP of two analytes of constant absolute amount. LE and TE concentration (not shown) and field strengths are assumed constant; all subfigures are for ITP in equilibrium. The two analytes and their constant amounts are indicated by the 3 circles and triangles each. Upon downscaling of the cross-section from A to B to C, correspondingly less ions are needed to achieve the plateau concentration per length. A & B correspond to peak mode equilibrium, with no separation, C Equilibrium in plateau mode with the two compounds each in its own zone corresponding to an improved separation vs. B.

1.4.4 Depletion zone isotachophoresis (dzITP)

A synergy between ITP and the nanofluidic effect of concentration polarization can provide a new hyphenated separation and focusing technique, dzITP. An important simplification compared to conventional ITP is that now only a single background electrolyte is needed, that doubles as the leading electrolyte. The zone depleted by the nanochannel provides a function similar to the terminating electrolyte, from whereupon the rest of the process in the channel can be described in analogy to ITP principles. Several of dzITP's potential applications and benefits are described in Chapter 5 of this thesis.

The working principle of dzITP can be described as a combination between ITP and concentration polarization in a microchannel perpendicular to a CP-induced by a tangential nanochannel. In a classical nanofluidic pre-concentration device, ions are focused due to a local gradient in the electric field induced by a depletion zone[65] (For details on the depletion zone see section 1.3.2 & Figure 1.6). In such a device however, a form of ITP can be induced: dzITP. The principle of dzITP is illustrated in Figure 1.10. In short, the depletion zone locally increases the electric field along the microchannel. While bulk flow, in this case by EOF, is constant along the microchannel, locally the individual migration velocity of ions is not, as a result of this difference in E-field; In the depletion zone migration is dominant over EOF while elsewhere the EOF is dominant. This creates a focusing condition at the interface between the leading electrolyte containing sample ions and the depletion zone, at the location where electromigration is exactly balanced by the EOF. This location is very stable and can be positioned by the applied potentials.

The depletion rate is a function of the charge asymmetry in the nanochannel per unit current (see section 1.3.2). The excess op positive ions, responsible for the charge asymmetry in the nanochannel, may be predicted based on the results reported on nanochannel deprotonation in Chapter 2, which give the amount of charge per surface area as a function of pH and ionic strength.

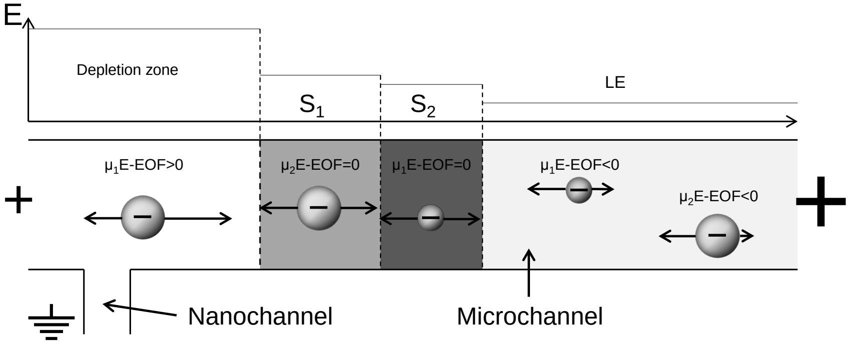

Figure 1.10 Principle of depletion zone isotachophoresis (dzITP) described by means of two negative analytes during the focusing and depletion process. The lower part of the graph shows part of a chip with an H-shaped channel pattern, comprising a nanochannel connecting two microchannels with reservoirs for fluidic and electrical connections at the ends (not shown). Indicated are the potentials applied, with ground on the nanochannel side and two different positive voltages at the microchannel ends. The gradient along the microchannel induces an EOF along the microchannel in the negative direction (right to left). In the top part of the figure indications for the electric fields per region are shown. The depletion zone created by the nanochannel (see section 1.3.2 & Figure 1.6, for details) has a large E-field (in practice several tens of times that of the LE zone). Indicated for two analyte ions (the LE ions are not shown) are the velocity contributions per zone. In the LE zone the EOF is dominant and the net velocity of analytes is negative transporting them towards the nanochannel. In the depletion zone the field is high, and migration of sample ions is positive. In the intermediate region the velocity of EOF matches that of the individual migration, and focusing occurs in order of mobility, as in ITP.

Depletion zone isotachophoresis belongs to the family of counter-flow gradient focusing techniques (CFGF)[66], more specifically to the electric field gradient focusing branch to which also other gradient focusing techniques such as gradient elution isotachophoresis (GEITP)[67], belong. These methods are characterized by a gradient in electric field strength along a microchannel in the presence of an opposing bulk flow, and each analyte is focused at a unique location based on its electrophoretic mobility. What sets dzITP apart from other gradient-focusing techniques such as gradient elution isotachophoresis (GEITP)[67], is that the depletion zone takes on a role similar to that of the trailing electrolyte so that only one electrolyte (a leading electrolyte) is needed in dzITP vs. e.g. GEITP. For negative analytes furthermore only EOF is needed to generate bulk flow, with the very high field in the depletion zone ensuring that there is a stable focusing position for any analyte. Technically the depletion zone is not a trailing electrolyte, as the mobility of its co-ion is not lower than that of the analytes, but explicitly the opposite, as it needs to function as leading ion.

The combination of depletion zone and focusing has been reported in literature before, in different configurations, as reviewed elsewhere[68]. For example in bipolar electrode focusing, where the depletion zone is locally induced by electrodes in the channel, also plateau concentrations as function of background electrolyte were reported[69]. Another example by which a depletion zone can be induced is by means of a Nafion membrane, either replacing the nanochannel in the configuration by means of a junction in a capillary[70], or in a chip[71], or placed locally on the bottom of a microchannel (filling only part of the height)[72]. What sets dzITP apart from other depletion zone focusing techniques is the crucial realization, that from the depletion zone onwards the interfaces between subsequent (higher mobility) analytes and interfaces the principles of ITP apply (See Figure 1.8) and as a consequence the toolbox of depletion zone focusing can be used in combination with that of ITP, as examples given in Chapter 5 of this thesis will show. This realization has apparently not occurred in other groups, most likely as they used only one analyte.

1.5 Surface-enhanced Raman spectroscopy

Surface enhanced Raman spectroscopy (SERS) is a special form of Raman spectroscopy, a technique that can detect very low amounts of molecules. Since it also is a form of vibrational spectroscopy it provides fingerprint spectra. Furthermore, particularly relevant for downscaling is that in SERS the signal originates from the sample volume up to some tens of nanometers from a surface. This makes SERS by its nature a detection principle suitable for nano-scale detection. These qualities make SERS a strong candidate for the integration in an analysis platform for minute metabolomic samples. Disadvantages include that a SERS surface needs to be integrated in the system and that currently irreversible binding of analytes and/or matrix compounds readily fouls the surface. This fouling makes it not compatible with inline use although off-line applications have been abundantly reported for some decades[73]

The use and principles of Raman spectroscopy and SERS are detailed below. To make SERS suited as a dynamic biodetector for multiple analytes, fouling as mentioned above should be prevented. This is the motivation for the evaluation of a thin (to allow SERS), anti-fouling coating, to turn a SERS substrate into a sensor responsive to concentration as well as concentration changes in time. This SERS sensor concept we have called SERSOR, and it is the subject of Chapter 5 of this thesis.

1.5.1 Raman & surface-enhanced Raman spectroscopy

In Raman spectroscopy a sample is irradiated using a laser of well-defined wavelength, and the energy of the scattered photons measured. Most of these photons will scatter away without a change in energy, so-called Rayleigh scattering, but some, approximately 1 in 10^6 photons will have exchanged energy with the vibrational levels of the samples molecules, so-called Raman scattering. The principle of Raman scattering is theoretically described below.

In practice, Rayleigh scattering is filtered out and the residual Raman spectrum resolved by diffraction and imaged on a CCD. The vibrational information in the spectrum is directly related to the functional groups of a molecule and can provide a fingerprint. In addition Raman spectroscopy is quantitative as the amount of scattering observed correlates with the molecular concentration. Last but not least Raman spectroscopy, unlike infrared-absorption spectroscopy, which is another vibrational technique, is not hindered by measuring in water. Acquiring fingerprint spectra and the possibility of measuring in solution make Raman spectroscopy highly attractive in bioanalysis. An example of a Raman measurement of some metabolites is shown in Figure 1.11.

Detection limits of Raman spectroscopy depend strongly on the molecular species, or more specifically its type of functional groups as well as wavelength and power of the laser used, but typically they are in the sub-millimole per liter range for biomolecules. In case of lower concentrations or corresponding very low abundance as in miniaturized systems, the detection limit of Raman spectroscopy is therefore challenged. In 1974 however, an enhancement of the Raman signal was observed on roughened silver or gold metal electrodes[74]. This significant enhancement is maximized when the metal is rough on the order of some tens of nanometers, preferably from the group of the coinage metals, and greatly decays with distance from the surface, d, on the order of d^{-12}.

The technique, called surface-enhanced Raman spectroscopy which makes use of this principle has greatly improved detection limits compared to normal Raman spectroscopy while still providing fingerprint spectra. These detection limits can equal the detection limits of LIF, reaching down to a single molecule for a select few compounds and generally providing nmol/L-µmol/L detection limits for many endogenous (unlabeled) biomolecules. An example of a SERS measurement of the biomolecule adenine is given in Figure 1.12 using silver metal colloids.

Importantly, this interaction requires the proximity of the molecule near the metal surface, at a distance on the order of tens of nanometers. For this reason SERS is a nanoscale detection method by nature (as detailed below in section

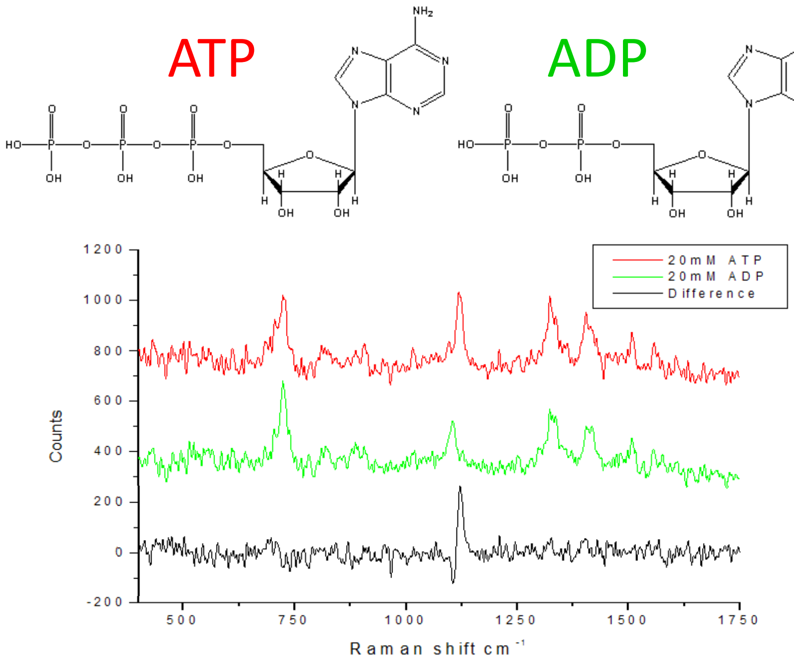

Figure 1.11 Raman scattering measurement of 20 mmol/L of ATP and ADP. On the x-axis the energy lost between emitted and scattered photons to the vibrations of the molecule is given, a Stokes shift, in so-called Stokes-Raman spectroscopy, Despite the similarity between ATP and ADP the difference in the spectrum, related to the phosphate groups is readily apparent upon straightforward substraction. Measured using a solid-state laser emitting at 785 nm, 10 s exposure time.

1.5.1). In addition, the SERS-active metals gold and silver adsorb analytes on their surface, which is even more beneficial for the detection limit. Unfortunately, this corresponds to fouling when dynamic measurements are required or surface competition when multiple analytes are to be detected, preventing calibration and quantitative measurements.

Principles of Raman spectroscopy

Consider a molecule in an incident oscillating electric field E (e.g. a laser light source), at frequency ω_I. This field induces a dipole moment P:

$$\vec{P} = [\alpha]\,\vec{E} \tag{1.3}$$

with:

$$\vec{E} = E_0 \cos(\omega_I t) \tag{1.4}$$

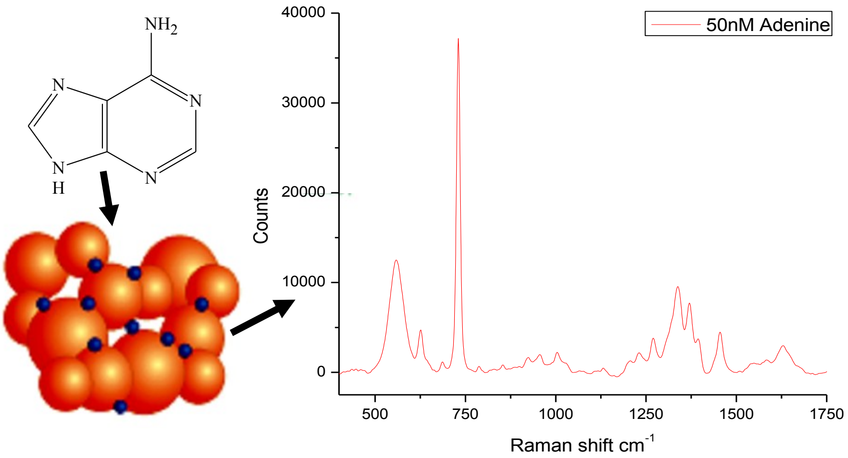

Figure 1.12 Surface-enhanced Raman measurement of adenine 50 nmol/L. The signal from adenine (blue particle) is enhanced by the proximity to silver particles (orange spheres) of 30-100 nm in size.

with α the polarizability (a 3x3 tensor), a characteristic describing the properties of the molecule's electron cloud. It indicates how much the electron cloud will shift in an electric field and affects the strength of the induced dipole.

If energy is absorbed in a vibrational level that changes the dipole moment P (with α constant), this corresponds to a net shift of the electron cloud, for instance in the linear molecule CO_2: O-C-O excited to the asymmetrical vibration from O—C-O to O-C—O. This process corresponds to those vibrations observed in infrared absorption spectroscopy. A change in corresponds to a symmetric perturbation of the electron cloud, so there is no net change in the polarization. This corresponds to Raman scattering. For instance in CO_2 the molecule can be excited to the symmetrical vibration O-C-O to O—C—O. More complex molecules can have a simultaneous change of both P and α, and can be observed in both IR and Raman scattering.

Raman scattering can both lose and absorb vibrational energy from the molecule, so-called Stokes and Anti-Stokes Raman respectively. In this work exclusively Stokes Raman is used. When a volume containing N molecules is probed, the total Stokes Raman signal I_{SR} is proportional to the Raman cross section σ^R and the incident laser intensity I_0. In formula:

$$I_{SR} = NI_0\sigma^R \tag{1.5}$$

Note that this relation illustrates why Raman is quantitative, since the signal scales directly with the amount of molecules N.

Principles of surface-enhanced Raman spectroscopy (SERS)

The principle of the enhancement is attributed to the metal, which has a much larger chance of interaction with the photon, mediating the energy exchange between photons and molecule[75,76]. An incoming photon induces a dipole oscillation in a metal, with roughness on the order of tens of nanometers, carried by displacement of surface electrons, a so-called surface plasmon. This surface plasmon in turn produces an electric field. A molecule near the surface will feel a total field from both the laser and the induced dipole,

$$\vec{E}_T=\vec{E}_0+\vec{E}_{dip} \tag{1.6}$$

The enhancement is defined as the ratio between the total field with and without the metal present:

$$A=\frac{\vec{E}_T}{\vec{E}_0} \tag{1.7}$$

This enhancement factor must be taken into account not only for the enhancement of the field of the laser $A(\omega_L)$, from laser to metal particle and metal particle to laser: $A(\omega_L)A(\omega_L)$, but also for the enhancement of the Raman scattered field $A(\omega_R)A(\omega_R)$, from molecule to particle and from particle to photon. Equation 1.5 then becomes[77]:

$$I_{SR}=NI_0\sigma^R\left|A\left(\omega_R\right)\right|^2\left|A\left(\omega_L\right)\right|^2 \tag{1.8}$$

Where ISR is the total Stokes Raman signal, N the molecules probed, σ^R the Raman cross section and the incident laser intensity I_0. This energy exchange is by far the most efficient through dipole interactions. As metal structures with roughness on the order of tens of nanometers support these exclusively (exact size varies per metal), this is therefore the optimal size range.

The strength of the induced field, E_T, scales strongly with the amplitude of the plasmon oscillation, which in turn depends on the relative freedom of the electrons in the metal which corresponds to the conductance. The coinage metals, silver, gold and copper have the highest conductance of all metals. They are in the same row of the periodic table, and share the property of having a full d shell while the s shell has only one electron. In physics this comprises the definition of a noble metal. This s electron grants the high conductance: in ascending order copper gold and finally silver provide the strongest enhancement.

An approximation of the enhancement factors in Equation 1.8 can be given for nanorough surfaces and as a model for the colloids used in Chapter 5, by means of describing the enhancement factor for a small spherical metal particle[77], equation 1.7 then becomes:

$$A\left(r,\omega\right)=\frac{\vec{E}_T}{\vec{E}_0}\approx 1+\left(\frac{\varepsilon\left(\omega,R\right)-\varepsilon_m}{\varepsilon\left(\omega,R\right)+2\varepsilon_m}\right)\left(\frac{R}{R+r}\right)^3 \tag{1.9}$$

with R the radius of the particle, r the distance between molecule and metal, $\varepsilon(\omega, R)$ the dielectric function of the metal depending on ω and the radius of the particle R (which explains why ε_m the dielectric constant of the metal, The approximation of eq 1.9 illustrates the experimentally observed strong decay of SERS signal with distance from the surface. Namely, the enhancement $A(r, \omega)$ drops with increasing distance d as $\approx\ r^{-12}$. At approximately 100 nm, equation 1.9 is reduced to 1, corresponding to normal Raman.

1.6 Goal & Scope of this thesis

Life sciences research, and especially metabolomics, will benefit greatly through the development of improved bioanalytical separation techniques. New approaches enabling the analysis of minute volumes of complex composition are therefore urgently required. Small-volume analysis can be achieved by miniaturization in fluidic chips, not in the least as the resolving power of both chromatographic and electrophoretic techniques can improve upon downscaling. Analysis of complex samples is possible by making use of the potential provided by Lab-on-a-Chip platforms, which can in principle provide standardized, automated and also faster analyses and integrated detection. Electrophoretic separation techniques provide the greatest resolving power and can become more effective upon downscaling; this is particularly true for isotachophoresis and trace analytes as explained in the previous subsection. This makes the smallest practical channels available, nanochannels, of great interest to explore for this purpose.

The goal of this thesis is to make analysis devices smaller, more efficient, and simpler to use for the analysis of small biosamples, specifically in metabolomics. For this purpose, nanochannels were utilized for electrokinetic separations and especially isotachophoresis and the new fundamental nanofluidic phenomena encountered were studied and reported. Nanochannels are not just smaller channels; many of their properties are still unknown, belonging to the field of nanofluidics with phenomena relevant whenever a dimension approaches the nanoscale including e.g. nanopores, biological ion channels, nanocavities etc. This makes the study of nanochannels, from the perspective of a platform to study nanofluidics, an interesting field of research. Possible limits of downscaling by nanochannels are also explored in this thesis.

In Chapter 2, a fundamental property of silicon oxide nanochannels, relevant when miniaturizing separations, is experimentally investigated for the first time and theoretically modeled. Namely, in nanochannels the surface-to-volume ratio is so large that the acidic glass is able to titrate solutions contained in them. To illustrate the scale and relevance of this effect: a 50 nm deep channel easily titrates 1 mol/L of buffer. This effect is relevant for the understanding of the electrochemical double layer on silicon oxide surfaces in general, including capillaries and (micro)channels. When downscaling devices to perform separations in nanochannels, this effect can be a dominant factor. A model to predict this behavior was established, and used in the further chapters to assist in the design of miniaturized isotachophoresis.

In Chapter 3 the limit in miniaturization of isotachophoresis (ITP) is explored, by assessing the performance of ITP in sub-micron channels and nanochannels for sub-picoliter metabolomic samples. Successful focusing and separation of a biosample representing approximately 5% (0.4 pL) of the volume of a typical human cell was demonstrated. This represents the smallest application of ITP to date. Furthermore, a hitherto unknown fundamental effect was discovered that provided a practical, fundamental limitation on the further downscaling of ITP: electrocavitation. Electrocavitation is also considered relevant on its own as a new phenomenon for the study of cavitation of liquids.

Chapter 4 presents the new technique of depletion zone isotachophoresis (dzITP), a successful synergy of nanofluidic phenomena and a microfluidic analysis method. The effect of concentration polarization induced by a nanochannel was used to create a depletion zone which in turn acts as the trailing electrolyte for ITP in a perpendicular microchannel. This technique enabled ITP with a single electrolyte, an important simplification of ITP, whose complexity until now hampered the widespread application of this powerful separation technique. In addition, dzITP provides a far greater control of the separation process compared to conventional ITP. This significant improvement of ITP resulting in dzITP provides a new separation technique that is very attractive for the sample preparation or analysis of complex samples such as in metabolomics.

In Chapter 5 the first steps in the development of a SERS based sensor are reported. Protecting the surface with a coating of polyethylene glycol gives the SERS surface the capability of being re-usable. This SERSOR concept was developed particularly with the purpose of inline detection of unlabeled biomolecules. A proof of concept is provided but coating robustness remains to be improved.

In Chapter 6 the results of the research described in this thesis are summarized and general conclusions and perspectives are provided.

CHAPTER 2

Solution Titration by Wall Deprotonation During Capillary Filling of Silicon Oxide Nanochannels[a]

2.1 Abstract

This paper describes a fundamental challenge when using silicon oxide nanochannels for analytical systems, namely the occurrence of a strong proton release or proton uptake from the walls in any transient situation such as channel filling. Experimentally, when fluorescein solutions were introduced into silicon oxide nanochannels through capillary pressure, a distinct bisection of the fluorescence was observed, the zone of the fluid near the entrance fluoresced, while the zone near the meniscus, was dark. The ratio between the zones was found to be constant in time and to depend on ionic strength, pH and the presence of a buffer and its characteristics. Theoretically, using the Gouy-Chapman-Stern model of the electrochemical double-layer, we demonstrate that this phenomenon can be effectively modeled as a titration of the solution by protons released from silanol groups on the walls, as a function of the pH and ionic strength of the introduced solution. The results demonstrate the dominant influence of the surface on the fluid composition in nanofluidic experiments, in transient situations such as filling, and changes in solvent properties such as the pH or ionic strength. The implications of these fundamental properties of silicon oxide nanochannels are important for analytical strategies and in particular the analysis of complex biological samples.

---

[a] Published as: Kjeld G. H. Janssen, Hanh T. Hoang, Jan Floris, Jeroen de Vries, Niels R. Tas, and Jan C. T. Eijkel and Thomas Hankemeier, *Analytical Chemistry*, **80**, 8095-8101 (2008).

2.2 Introduction

The fabrication and application of nanochannels have gained considerable interest in the past few years. Using bonding, 1D nanochannels are mostly formed by shallow etching of trenches in silicon (or glass) wafers followed by bonding to glass (or silicon) cover wafers to form enclosed channels[43,78]. 2D nanochannels can be fabricated using nanolithography[79–81], surface- and bulk- machining[82,83] and electrospinning[84]. Nanochannels are created in various types of materials such as silicon (silicon oxide, silicon nitride), glass and polymers[85,86]. An extensive review on fabrication was made by Mijatovic et al.[87].

Channels with such small dimensions are of interest because due to the extremely high surface to volume ratio, (electrical) interface effects between the fluid and channel wall surfaces become dominant[42]. For example, S. Pennathur et al.[88,89] described a novel nanoscale electrophoretic separation method in a theoretical and experimental study on the electrokinetic transport in nanochannels. Pu et al.[49] demonstrated an ion-enrichment and ion-depletion effect when an electric field was applied across two reservoirs connected by 60 nm deep channels.

Less known, the surface chemistry of silicon oxide has a large influence on solutions in nanochannels. It has been known for a very long time that the silanol groups present on silica are capable of protonating the solution in contact with it. Actually, this effect has been used to assess the presence of silanol groups on silica beads in chromatographic columns via the indicator methyl red which colors red at a pH below 4.4[90].

2.2.1 General description of the phenomenon and hypothesis.

In this paper we demonstrate that a solution introduced into an empty silicon oxide nanochannel is acidified and dissolved substances protonated. For this purpose we measured the fluorescence of solutions of fluorescein, which has a strong pH-dependent fluorescence, introduced in empty channels through capillary pressure. During filling, two distinct zones were observed, with the zone of the solution starting from the entrance showing fluorescence, while in the zone near the flow front no fluorescence was observed, as shown in Figure 2.1. The movie belonging to this experiment, showing the filling of the nanochannel and the progression in time of the two zones, has been provided in the electronic supporting information at the ACS publications website belonging to the paper this chapter is adapted from, Movie S-1.

To study this phenomenon in more detail we varied pH, buffer concentration and ionic strength and determined for various solution compositions the ratio of the lengths of the fluorescing and dark zones. From this ratio we calculated the number of protons released per m^2 and compared these data with a model based on oxide surface chemistry theory[91] which predicts the amount of released pro-

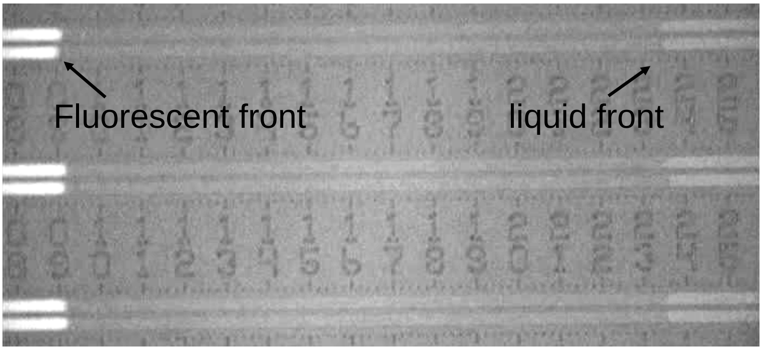

Figure 2.1 Typical image of fluorescence observed in nanochannels during filling. In this experiment, (experiment. no. 1 of Table 2.1, screenshot of Movie S-1), the partial filling of parallel channels, 20 µm wide and 40.5 nm deep, taken at t = 5 s, are shown. From left to right the channel is filling from the reservoir, which is outside the image shown. Fluorescence is observed in the filled zone, from x = 0 to x = 0.92 mm, but not in the zone from x = 0.92 mm to 2.36 mm.

tons. The results obtained describe an effect relevant for nanofluidic experiments because they indicate the influence of the surface chemistry on fluid composition such as pH and wall charge in transient situations.

2.2.2 Considerations of relevance of other nanochannel effects.

Ion exclusion of the negatively charged fluorescein was first considered as a possible explanation of the observed phenomenon, but discarded since the phenomenon became more pronounced with increasing ionic strength. For the same reason also the generation of a streaming potential was discarded as an explanation. Straightforward retention due to adsorption to the wall, as in thin layer chromatography, which could become significant due to the high surface to volume ratio, can also be ruled out. S. Pennathur et al.[89] in fact demonstrated experimentally that fluorescein effectively travels faster instead of slower through silicon oxide nanochannels as compared to microchannels, due to exclusion of the negative ion from the double layer. A final argument to support the titration theory is that experiments we performed with a pH-insensitive dye (Alexa, molecular probes; data not shown) showed no significant lagging of the fluorescent front.

2.2.3 Chip manufacture.

Chip devices containing micro- and nanochannels were fabricated based on the approach of Haneveld et al[43]. Nanochannels and microchannels (including rulers for filling observation) were manufactured in the bottom-side silicon wafers by wet chemical etching and reactive ion etching, respectively. After etching, a dry thermal oxide of 20 nm thickness was grown on the silicon wafers to ensure adequate surface hydrophilicity for capillary filling of the nanochannels. The etch depths of the channel structures were measured with a mechanical surface profiler (Dektak 8, Veeco Instruments Inc., Plainview, NY, USA). The processing of the top-side Borofloat glass wafers consisted of powder blasting of access holes followed by thorough wafer cleaning to remove residue from the abrasive powder blasting particles. Prior to prebonding the top and bottom wafers were Piranha cleaned. This step was followed by fusion bonding at 400°C for 4 hours, to ensure identical starting conditions for the experiments. For a layout of the channel structure, see Figure 2.2. Directly prior to the experiments the wafers were conditioned by heating for 2 hours at 400°C, to ensure identical starting conditions for the experiments.

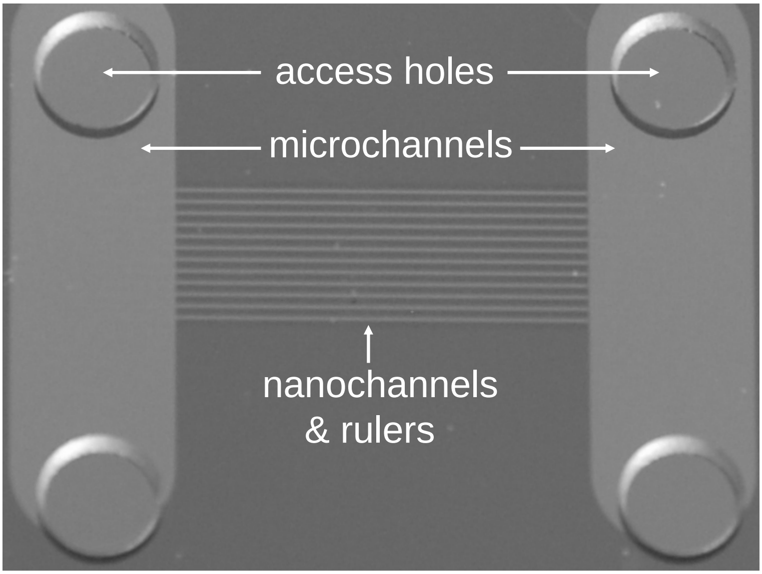

Figure 2.2 Chip layout seen from the top. Vertically, the microchannels connecting the two pairs of access holes can be seen and between them the rulers positioned along the nanochannels are visible. The nanochannels are 50 nm deep and 20 µm wide, the microchannels are 20 µm deep, 15 mm long and 4 mm wide.

2.2.4 Fluorescence measurements.

To probe the pH in the nanochannels, we used the fluorescent activity of disodiumfluoresceine (Sigma-Aldrich, St. Louis, MO, USA). Depending on the pH, fluorescein can have a double or single negative charge or be neutral; the single negatively charged form has a pK$_a$ of 6.68 and the neutral form has an apparent pK_a of 4.34[92]. When the molecule is excited at 488 nm and emission is measured at 514 nm, the molar response of the ion having a valence of -1 is only 5.7% and that of the neutral form 0.8%[93] in comparison to the ion having valence -2; therefore the emission can be used as an indicator of the local pH.

Measurements were done on a fluorescence microscope (Leica DM LM, Wetzlar, Germany), using a 100 W mercury lamp, an I3 filter cube and a 510 nm dichromatic mirror. Movies were taken with a CCD camera to record the movement of the solutions entering the empty nanochannels and analyzed using Pinnacle software (Pinnacle, Mountain View, CA, USA). From the parallel channels one was selected for measurement, as differences between parallel channels were small (see Fig 2.1).

2.2.5 Composition of the introduced solutions.

To buffer the solutions, 2-amino-2-(hydroxymethyl)propane-1,3-diol (TRIS) was used, having a pK_a of 8.06 (Merck & Co., Inc., Whitehouse Station, NJ, USA). To influence the ionic strength, various amounts of potassium chloride (KCl) (Sigma-Aldrich, St. Louis, MO, USA) were added. The composition of the solutions introduced in the channels were all made in deionized water (0.7 µS/cm) and are described in Table 2.1.

Table 2.1 Composition of the solution, the height (h) of the channel and the measured pH for the various experiments.

Expt	(mol/L) of			h(nm)	pH
	Tris	HCl	KCl		
1	0	0	0	40.5	7.3
2	0	0	0	49.0	7.4
3	0	0	0.1	48.0	7.1
4	0	0	0.1	49.0	7.2
5	0	0	0.2	52.8	7.2
6	0	0	0.2	44.0	7.1
7	0	0	0.5	47.8	7.1
8	0	0	0.5	47.0	7.0
9	0.2	0.073	0	50.0	8.6
10	0.2	0.073	0	50.3	8.4
11	0.2	0.073	0.1	49.8	8.4
12	0.2	0.073	0.2	50.3	8.4
13	0.2	0.073	0.5	45.5	8.5
14	0.2	0.073	0.5	48.4	8.4
15	1	0.364	0	49.5	8.5

2.3 Theory

2.3.1 Capillary filling.

The walls of the nanochannels in the chip device are assumed to have hydrophilic silanol groups. When liquid comes into contact with such a nanochannel, the liquid is pulled into the empty channel by capillary forces creating a pressure gradient ΔP (Pa),

$$\Delta P = \frac{-2\gamma\cos\theta}{h} \tag{2.1}$$

with γ the gas liquid surface tension (Nm^{-1}), θ the contact angle and h the channel height. The position, x(m), of the liquid front in a nanochannel at any point in time, t(s), is given in accordance with the Washburn equation for a rectangular channel with the condition: width $>>$ height[94,95], and viscosity μ (Pa·s):

$$x = \sqrt{\frac{\gamma h t \cos\theta}{3\mu}} \tag{2.2}$$

2.3.2 Experimental amount of protons released.

We explain the phenomenon observed in Figure 2.3, as follows. As the aqueous solution is introduced into the nanochannel from the reservoir, protons are released from the wall into the solution, lowering the pH as well as protonating compounds in the solution. When the fluid flows along the channel, the front of the fluid continuously comes into contact with a new section of the wall, with which it anew establishes equilibrium, again taking up protons. This process continues until the fluid in the liquid front reaches a pH corresponding to the point of zero charge (pzc) of SiO_2, which is on the order of $pH_{pzc} = 2-3$. At a pH of the fluid below this pH_{pzc} the wall will no longer release protons. On the other hand, the zone of fluid behind the front comes into contact with a wall already in equilibrium with a solution of this composition. As a result, the fluorescein is no longer protonated, and the zone near the entrance will maintain its fluorescent activity (see Figure 2.3).

We assume infinitely fast (de)protonation reactions ($\propto$ fs) and we calculated the diffusion time, from the wall to the center of the channel, using Einstein-Smoluchowski[96], to be 35 ns. Therefore for our experiments we assume the onset of radial equilibrium due to the small dimension of the channel to be infinitely fast. The time scale of the axial diffusion of protons ($\propto 1000$ s for an average diffusion distance of half the channel length) is 1 order of magnitude larger than the timescale of filling the channel ($\propto 100$s). For our calculations we will assume that the pH change from that of the introduced solution to the pH_{pzc} occurs abruptly at the fluorescent front. In the Results and Discussion we will show the validity of this assumption based on experimental results (see Figure 2.3).

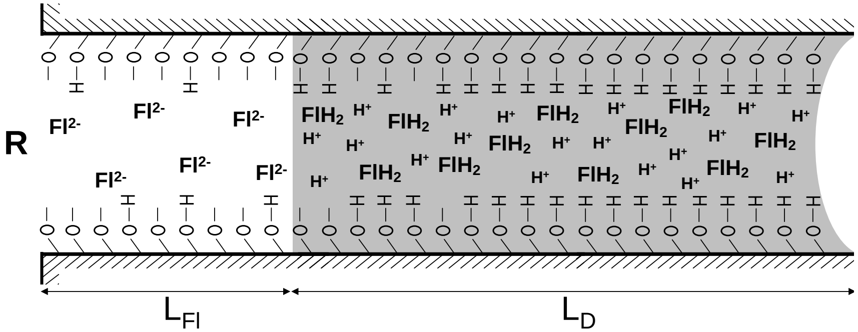

Figure 2.3 Axial cross-section of a filling nanochannel. R indicates the reservoir from which the nanochannel is filled. L_{Fl} and L_D correspond to the fluorescent and dark zone of the channel, respectively. In the fluorescent zone the pH is that of the introduced solution where fluorescein is present mainly as doubly charged anions (Fl^{2-}). The fluid in the dark zone contains an excess of protons, with $pH = pH_{pzc}$ and fluorescein is mainly present as the uncharged fluorescein molecule (FlH_2), having negligible fluorescence.

We denote the length of the fluorescent and dark zone as L_{Fl} and L_D respectively as shown in Figure 2.3. The protons released from the walls in the fluorescent zone of the channel are responsible for protonating the fluorescein in the dark zone, so that L_{Fl} can be used to deduce the released number of protons, $N_{H^+_{released}}$ via

$$N_{H^+_{released}} = N_S \Theta^- L_{Fl} 2(h+w) \tag{2.3}$$

where Θ^- is the fraction of the surface groups that is negatively charged, N_S the total number of SiOH sites, taken to be $4.6 \cdot 10^{18}$ groups per m^2 [97], h (m) is the measured height and w (m) the width of the channel; see also Table 2.2 for a description of the general variables in the equations.

The amount of protons absorbed by the solution in the dark zone (L_D), $N_{H^+_{absorbed}}$, can then be expressed using the number of protons necessary to change the pH from its initial value to the point of zero charge, B_S (in mol/m^3), as

$$N_{H^+_{absorbed}} = N_A B_S L_D h w \tag{2.4}$$

with N_A Avogadro's constant. B_S includes the concentration of protons needed to protonate fluorescein and the concentration required to establish a pH equal to pH_{pzc}. If a buffer is present, the concentration of protons needed to protonate the buffer is calculated based on the composition according to Table 2.1, e.g., 0.2 mol/L Tris buffer brought to pH 8.4 with 0.072 mol/L HCl requires 0.128 mol/L of protons.

Typical results for the position of the fluid front and fluorescent front are given in Figure 2.4. The linear relationship between the position of the fluid front and the square root of time is in good agreement with the Washburn equation (2.2)

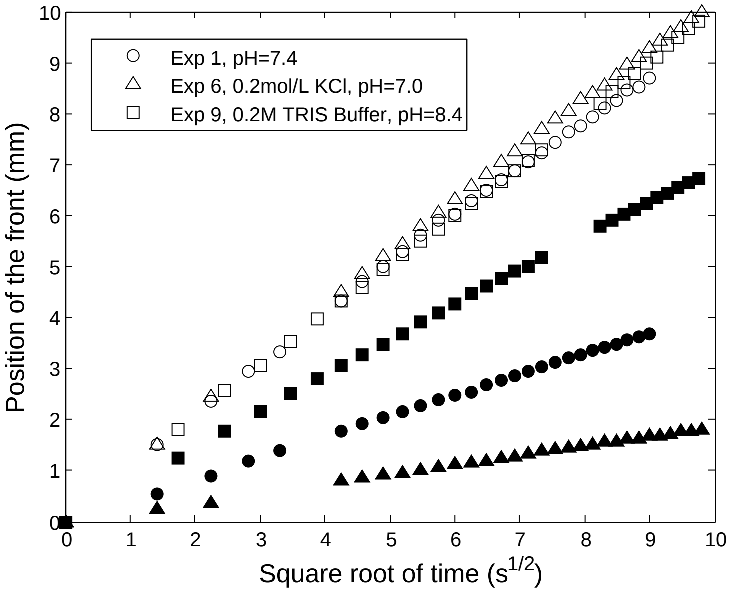

Figure 2.4 Position of the meniscus (empty symbols) and the fluorescent front (filled symbols) versus the square root of time for experiments 1, 6 and 9. All graphs could be linearly fitted using a least squares method with a value of $R^2 > 0.99$.

and earlier results reported by Tas et al[95]. A constant ratio between the positions of the meniscus and the fluorescent front is observed, with the fluorescing zone of the channel linearly dependent on the amount of channel filled. This means that the ratio L_D/L_{Fl} is constant per experiment and can be used to characterize it. For example, the experiments 1, 6, and 9, (shown in Figure 2.4) have a ratio of 0.41, 0.18, and 0.70, respectively. This actually supports our assumption that axial proton diffusion does not have a significant effect on our experiments. If this would be the case, this would show up as a nonlinearity of the plot of the fluorescent front against time toward the end of the experiment, which is not seen in the data.

We can derive the number of protons released per area of wall, $N_{H^+_{exp}}$, as a function of the observed ratio of dark and fluorescent zones, by equating the absolute amounts of released and absorbed protons (eqs 2.3 and 2.4) and using $h << w$:

$$N_{H^+_{exp}} \equiv N_S \Theta^- = N_A B_S h \frac{1}{2} \frac{L_D}{L_{Fl}} \tag{2.5}$$

Equation 2.5 provides an experimental expression for the amount of released protons.

2.3.3 Theoretical amount of protons released.

We will now construct a theoretical model to describe the theoretical amount of released protons which can be verified by comparing it to the experimental data. When the channel is filled with an aqueous solution it interacts with the silanol groups as described by the following surface reactions

$$SiOH_2^+ \rightleftharpoons SiOH + H_S^+ \tag{2.6}$$

characterized by the dissociation constant K_{a1} and

$$SiOH \rightleftharpoons SiO^- + H_S^+ \tag{2.7}$$

characterized by the dissociation constant K_{a2} and with H_S^+ the concentration of protons at the surface. pK_{a2} has been reported to be 6.7[98] and pK_{a1} has been reported to be -1.9[99].

When protons are released into solution, this induces a negative potential on the silicon oxide surface, Ψ_0, and a surface charge σ_0. The surface charge depends on the amount of SiOH sites, N_S, the dissociation constants K_{a1} and K_{a2} and the proton activity at the surface $a_{H_S^+}$ and is given by[91]:

$$\sigma_0 = qN_S \left(\frac{a^2_{H_S^+} - K_{a1}K_{a2}}{a^2_{H_S^+} + K_{a1}a_{H_S^+} + K_{a1}K_{a2}} \right) \tag{2.8}$$

The negative potential affects the distribution of ions in the solution directly near this surface such that there is a region containing its counter charge. This system of charged wall and the region containing the counter charge density of ions in solution is known as the electrical double layer (Figure 2.5).

At some distance from the surface, at least several Debye lengths, the bulk solution is characterized by its bulk number concentration of ions, n^0 (m^{-3}, for a 1:1 ion equal to the ionic strength) and bulk pH, pH_B. The difference in proton activity between surface and electroneutral bulk is according to Boltzmann

$$pH_S = pH_B + \Psi_0 \frac{q}{2.3kT} \tag{2.9}$$

with k Boltzmann's constant, q the elementary charge, and T temperature. This equation can be used to express measured bulk pH into σ_0 via eq 2.8 and demonstrates the dependence of σ_0 on pH_B. The combination of Poisson's equation with Boltzmann's equation also gives an expression for the surface charge[48]:

$$\sigma_0 = \sqrt{8kT\varepsilon\varepsilon_0 n^0} \sinh\left(\frac{q\Psi_0}{2kT}\right) \tag{2.10}$$

This equation demonstrates the dependence of σ_0 on the ionic strength n^0 and it can be used to calculate Ψ_0. The charge on the electrolyte side of the double

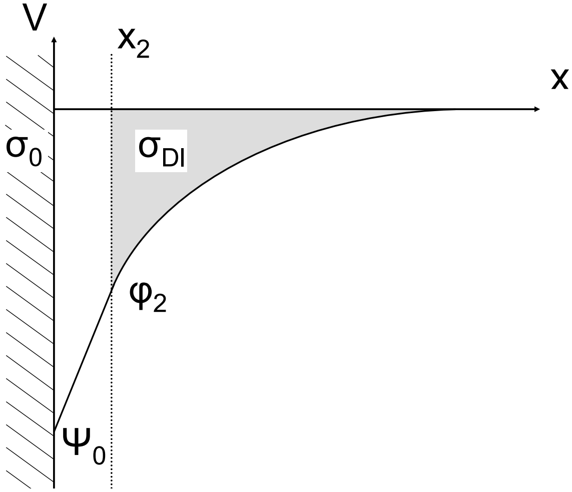

Figure 2.5 Schematic representation of potential V versus the distance x from the silicon oxide wall. Ψ_0 is the potential at the wall. x_2 is the position of the Stern plane, the plane of closest approach of ions toward the surface, having the potential ϕ_2. The region from the wall to the Stern plane is called the Stern layer. σ_0 (eq. 2.8 and eq. 2.13) indicates the surface charge per m^2 from deprotonated silanol groups at x=0. σ_{Dl} is the countercharge to σ_0 per m^2 (eq. 2.11), composed of ions located in the area beyond the Stern plane, the so-called diffuse part of the double layer (gray region).

layer, σ_{DL} is equal and of opposite sign to the surface charge σ_0 and can be described as a function of a double layer capacitance C_{DL} (in F/m^2) and the surface potential Ψ_0:

$$\sigma_{DL} = -C_{DL}\Psi_0 = -\sigma_0 \tag{2.11}$$

For our model we make use of the refinement of double layer theory as proposed by Stern[48]. Ions have a finite size and the closest distance they can approach the surface, equal to the radius of an ion, is the so-called Stern plane. This causes the potential drop across the double layer to have a discontinuity (Figure 2.5). Directly near the surface the double layer is described by the potential drop across the Stern plane from Ψ_0 to ϕ_2. The capacitance of the Stern layer, C_{Stern} (in F/m^2) is therefore given by:

$$C_{Stern} = \frac{\sigma_0}{\Psi_0 - \phi_2} \tag{2.12}$$

Beyond the Stern plane the surface charge density in the diffuse layer of counter ions is now described by:

$$\sigma_0 = \sqrt{8kT\varepsilon\varepsilon_0 n^0}\sinh\left(\frac{q\phi_2}{2kT}\right) \tag{2.13}$$

and the capacitance of the diffuse part of the double layer, C_{Diff} is given by:

$$C_{Diff} = \frac{\sigma_0}{\phi_2} \tag{2.14}$$

The double layer capacitance is given by the Stern and diffuse layer capacitances placed in series[48]:

$$C_{DL} = \frac{1}{C_{Stern}^{-1} + C_{Diff}^{-1}} \tag{2.15}$$

To describe titration experiments of SiO_2 surfaces, colloid experiments typically take values for C_{Stern} of 0.8 to 1.4 F/m^2 [100]. It has also been argued that for a porous well ordered planar surface values for C_{Stern} between 0.8 to 1.7 F/m^2 should be assumed[100]. As these values for C_{Stern} vary considerably and strongly affect our model, we used C_{Stern} to fit the measurement results (2.5), with the constraint of one C_{Stern} for all experiments.

From the above eqs 2.8 to 2.15 we can derive σ_0 via an iteration procedure (see footnote [b]), and therefore the amount of protons released per surface area into the bulk solution:

$$N_{H^+_{theory}} = \frac{\sigma_0}{q} \tag{2.16}$$

which can be fitted to $N_{H^+_{exp}}$ (eq 2.5). An overview of constants and parameters used for fitting is given in Table 2.2.

2.4 Results & Discussion

2.4.1 Theoretical results.

Our theoretical model shows how the capacity of the solution to take up protons, via a buffer and via fluorescein itself, affects the position of the fluorescent front. More buffer for this reason leads to a larger fluorescent zone. The model shows how a higher pH of the introduced solution increases the amount of protons per nm^2 to be released (eq 2.9, a higher pH induces a more negative surface potential effectuated by proton release). It also shows how the ionic strength affects proton release (eq 2.13, for a more in depth explanation see footnote [c]) as is seen in

---

[b] The iteration procedure, has the ionic strength and measured pH (Table 2.1), as well as the surface properties stated above (Table 2.2), as input parameters. Choosing a starting value for Ψ_0, it is entered into Boltzmann's equation (eq 2.9) giving the surface activity of protons, which is used to calculate σ_0 (eq 2.8) and subsequently applied to yield ϕ_2 (eq 2.13). Finally a new value for Ψ_0 is calculated from $\Psi_0 = \phi_2 + \sigma_0 / C_{Stern}$ (eq 2.12) and reentered into the Boltzmann equation(eq 2.9). The stable value for σ_0 is then used for equation 2.16.

[c] The effect of the ionic strength is demonstrated by the Debye-Hückel approximation[48] of C_{Diff} as $C_{Diff} = \varepsilon / \lambda_D$, with λ_D the Debye length. A higher ionic strength, n_0, decreases the Debye length and increases C_{Diff}, leading to a larger negative surface charge density and a larger proton release to titrate the solution.

Table 2.2 Constants and parameters used in fitting the data.

Constants	description	value
q	elementary charge	$1.6022\text{x}10^{-19}$ C
k	Boltzmann's constant	$1.38\text{x}10^{-23}$ J/K
ε_0	permittivity of free space	$8.8542\text{x}10^{-12}$ C^2/Nm^2
N_A	Avogadro's constant	$6.022\text{x}10^{23}$ mol^{-1}
Experimental variables		Remarks
T	temperature	297 K
ε	relative permittivity of water	80, in presence of salt
N_S	silanol groups per m^2	$4.6\text{x}10^{18}$ [97]
h	measured channel height	Table 2.1
pH_B	measured bulk pH of introduced solutions	Table 2.1
L_D	length of dark zone	Figure 2.4
L_{Fl}	length of fluorescent zone	Figure 2.4
Calculated variables		Remarks
pH_S	calculated pH at the surface	eq 2.9
pH_{pzc}	pH at point of zero charge of SiO_2	average of pK_{a1} & pK_{a2}
n^0	ionic strength in the bulk	m^{-3}, derived from Table 2.1
B_S	required protons to titrate from pH_B to pH_{pzc}, includes those for fluorescein, and any buffer.	mol/m^3 derived from Table 2.1 & pH_{pzc}
$N_{H^+_{exp}}$	amount of protons released per m^2 of wall	calculated from experiment, see eq 2.5
Ψ_0	surface potential in V, calculated with fitted variables and Table 2.1	solved numerically, see footnote [b] p37
ϕ_2	potential at the Stern plane in V calculated with fitted variables and Table 2.1	solved numerically, see footnote [b] p37
σ_0	surface charge in C/m^2, calculated with fitted variables and Table 2.1	solved numerically, see footnote [b] p37
$N_{H^+_{theory}}$	theoretical amount of released protons per m^2 of wall	derived from σ_0 eq. 2.16
Fitted variables		Remarks
pK_{a1}	dissociation constant eq. 2.6	-1.9 [99] selected for the fitting of Fig.2.7
pK_{a2}	dissociation constant eq. 2.7	fitted
C_{Stern}	Stern capacitance in F/m^2, affects H^+_{theory}, eq. 2.16	fitted

our experiments. Hereby the buffer ions are incorporated in the determination of the ionic strength. Figure 2.6 shows the theoretically calculated amount of deprotonated groups as a function of pH and ionic strength. Using this model we fitted our experimental results.

2.4.2 Fitting results.

The parameter space we investigated to fit the data was pK_{a2} = [4 to 7.5] and pK_{a1} = [-2.4 to 0]. Each pair of pK_a values was used to fit the data of the unbuffered and buffered results, under the constraint that C_{Stern} is equal for all data, using eqs 2.8 to 2.15 according to the iteration procedure described in footnote [a] p37. As

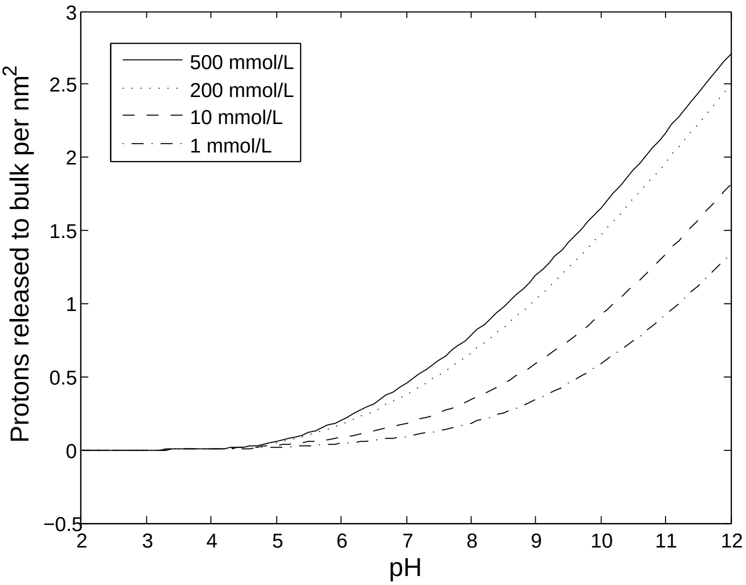

Figure 2.6 Theoretical amount of deprotonated silanol groups per nm^2 as a function of pH. The different curves, belonging to 1, 10, 200, and 500 mmol/L of KCl, show the effect of the ionic strength on proton release, with more salt inducing a higher release, which will be observed as a shorter fluorescent zone.

a side note, interestingly, it appears that the fitting results could be described by the empirical relation C_{Stern} = 2.32x10$^{-4}e^{3.77pH_{pzc}}$ (R^2 = 0.99) and therefore many pairs of dissociation constants pK_{a1} and pK_{a2} yielded a good fit as long as they gave the same pH_{pzc}.

Figure 2.7 shows measured data points as well as fitted curves, displaying the amount of released protons as a function of ionic strength. To generate Figure 2.7, we chose pK_{a1} = -1.9 based on literature[99], which yielded a dissociation constant pK_{a2} = 6.77 close to the literature value of 6.7 reported by Davis et al.[98], accepting a somewhat high C_{Stern} of 2.30 F/m^2.

High values of C_{Stern} (greater than 1.7 F/m^2) for a nonporous surface can be attributed to complexation of ions in solution with silanol groups[98]. This is because ionic complexation has been reported to shift the point of zero charge[101] from its value as the mean of the pKa's, when only protons are the potential determining ions, to another value. According to our empirical relation a slight difference in pH_{pzc} results in a significant change in C_{Stern}, e.g. compared to $pH_{pzc} = 2.44$ with $C_{Stern} = 2.3$ F/m^2, $pH_{pzc} = 2.36$ yields $C_{Stern} = 1.7$ F/m^2. A second explanation for high values of C_{Stern}, according to Hiemstra et al.[100] is the silicon oxide surface having a less condensed surface structure and the presence of reactive surface groups protruding from the surface.

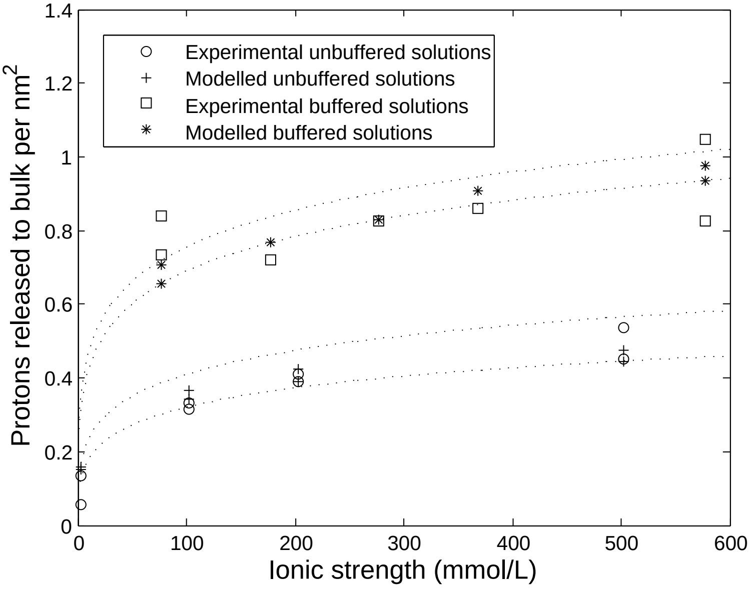

Figure 2.7 Results of the experiments, $N_{H^+_{exp}}$, fitted with the model, $N_{H^+_{theory}}$. Fits were made using the input and fitting parameters from Tables 2.1 and 2.2, with the dissociation constants pK_{a1} = 6.77 and pK_{a2} = -1.90 and therefore a pH_{pzc} = 2.44. A value of C_{Stern} = 2.30 F/m^2 led to the optimal fit with R^2 = 0.93 for the unbuffered solutions and R^2 = 0.37 for buffered solutions. The data point for the buffered solution at an ionic strength of 386 mmol/L has a buffer strength of 1 mol/L, the others 0.2 mol/L. The dashed lines indicate the modeled values corresponding to the extremes of pH in the introduced solutions, from top to bottom, pH = 8.6, pH = 8.4, pH = 7.4, and pH = 7.0.

A good fit was achieved for the solutions containing fluorescein and KCl, R^2=0.93, and a lesser fit was found for the solutions containing TRIS buffer R^2=0.37, due to the spread in experimental results (See variation in duplicate experiments in Figure 2.7).

Figure 2.7 shows that the variation in amount of released protons is reasonably explained by the variation in ionic strength and the pH of the filling fluid. On the other hand the buffer concentration in the filling fluid does not affect the released amount of protons per wall area (apart from its contribution to the ionic strength). This is indeed expected since the model gives an amount of protons released per wall area based only on the equilibrium with an infinite solution of the initial pH and ionic strength. Though the buffer concentration affects the ratio between the dark and fluorescent zone, this is incorporated in eq 2.5, leading to an amount of protons released per wall area independent from buffer concentration.

2.4.3 Buffer effects.

Figure 2.7 shows a large spread in the duplicate measurements of several buffered solutions. This is probably caused by substantial variations in the buffer composition. Inspection of Table 2.1 shows that the measured pH of the Tris-buffered solutions varied between 8.4 and 8.6, though all solutions were prepared by adding 0.072 mol/L HCl to a 0.2 mol/L Tris solution. These pH differences would indicate substantial differences in buffer capacity of the resulting solutions, affecting the value of B_S and $N_{H^+_{exp}}$ (eq 2.5).

2.4.4 Fluorescence front.

The results show a release of approximately 0.8 protons per nm^2 for the solutions around pH = 8.5, and 0.4 protons per nm^2 for the unbuffered solutions, pH = 7-7.4. We would like to stress the effect that such an amount of released protons has in shallow channels of 50 nm in height and arbitrary width. For a released amount of 0.5 protons/nm^2, 1 proton is released into the 50 nm^3 between the two walls or 0.02 protons per nm^3 (corresponding to a concentration of 33 mmol/L). To titrate a solution of 0.6 molecules per nm^3 (1 mol/L) the solution therefore has to pass only 30 nm of channel.

Together with the very fast equilibration in radial direction, this can explain our observation of a sharp fluorescence boundary for example in Figure 2.1. The argumentation for this is as follows: the protons diffusing axially into the fluorescent zone will be buffered by the solution, whereas fluorescein and/or buffer molecules that diffuse into the dark zone will be instantly protonated. Even if axial diffusion contributes significantly to proton transport relative to the flow of solution, this transient zone between dark and fluorescent regions will be the first to be in contact with undeprotonated wall and become protonated to pH_{pzc}. This effectively conserves the sharpness of the boundary between the dark and fluorescent zones, as is observed in our experiments.

2.5 Conclusion

A new phenomenon was observed unique to nanofluidics, namely a decrease in the fluorescent activity of fluorescein during capillary filling. The observed dark and fluorescent regions can be explained by acidification of the solution via deprotonation of the silanol groups at the wall. This mechanism could be verified by establishing a model based on the double layer theory and fitting this to the data. This mechanism represents a unique way to titrate a solution without adding additional counterions and to study the properties of a surface.

As chemical analysis in nanochannels is a growing field of research, the understanding of the effects of the nanostructure walls, due to a high surface to volume ratio, on the solution pH and the resulting changes in wall potential are of great significance. Importantly, this will occur in all transient cases, which means not only during filling but also when the solution pH or ionic strength is changed. This will be especially important for the analysis of biological samples because of its complex matrix composition. Fortunately, these effects can be modeled as demonstrated in this study.

2.6 Acknowledgements

Support from Nanoned (flagship Nanofluidics) is gratefully acknowledged. We also acknowledge Dr. Heiko van der Linden for useful comments on the manuscript.

CHAPTER 3

Limits of miniaturization: Assessing ITP performance in sub-micron and nanochannels[a]

3.1 Abstract

The feasibility of isotachophoresis in channels of sub micrometer and nanometer dimension is investigated. A sample injection volume of 0.4 pL is focused and separated in a 330 nm deep channel. The sample consists of a biomatrix containing the fluorescently labeled amino acids glutamate and phenylalanine, 20 attomoles each. In a 50 nm deep channel, isotachophoretic focusing is successfully demonstrated. Separation of the two amino acids in the 50 nm deep channel however, could not be performed as the maximum applicable voltage was insufficient. This limit is imposed by bubble formation that we contribute to cavitation as a result of the mismatch in electro-osmotic flow, so called electrocavitation. This represents an unexpected limit on miniaturization of ITP. Nonetheless, we report the smallest isotachophoretic separation and focusing experiment to-date, both in terms of controlled sample injection volume and channel height.

---

[a] Published as: Kjeld G. H. Janssen, Jiajie Li, Hanh T. Hoang, Paul Vulto, Richard J. B. H. N. van den Berg, Herman S. Overkleeft, Jan C. T. Eijkel, Niels R. Tas, Heiko J. van der Linden and Thomas Hankemeier, *Lab On a Chip*, **12**, 2888, (2012).

3.2 Introduction

The last three decades, major efforts have been invested in the miniaturization of elecktrokinetic separation techniques, such as zone electrophoresis, iso-electric focusing and isotachophoresis[32–35]. With the advent of nanochannel fabrication technologies[43] emphasis has shifted towards the nanofluidic domain. So far, liquid chromatography[44,45] and zone electrophoresis[46,47] have been successfully demonstrated in a nanofluidic environment.

Isotachophoresis (ITP) particularly benefits from downscaling as the resolution in equilibrium increases with decreasing channel cross-section, for a given amount of analyte. This inherent benefit originates from the fact that ITP is a concentration driven focusing technique. In equilibrium, the achieved concentration depends on the absolute amount of analyte, independent of initial concentration or sample volume. When available in sufficient amounts, a maximum concentration is reached and analytes are separated in neighboring zones, so called plateau mode ITP. The plateau concentration depends amongst others on the concentration of the leading electrolyte (LE) and the mobility of the analyte[53–56]. In ITP the resolving power can be expressed as a signal-to-noise ratio (SNR) given by the length of the analyte plateau zone normalized by the characteristic length of diffused zone boundaries[58,60]. Upon downscaling the cross-section of an ITP channel, a correspondingly lower absolute amount of analyte is required to achieve the same ITP equilibrium concentration and separation. Therefore, with the absolute amount conserved, downscaling the cross section by a certain factor, the same amount of compound will occupy a correspondingly longer section of channel, thereby improving resolution and signal to noise ratio for ITP in equilibrium by the same factor. In case of a detector based on absolute amount per length of channel a trade-off needs to be considered between better separation of compounds vs a lower signal per channel length and longer analysis times. If not enough absolute amount of analyte is present, the plateau concentration is not reached, and analytes focus as peaks (so-called peak mode ITP) that may overlap partially or even completely[58]. Sufficient downscaling will then allow these compounds to be focused at a higher concentration in equilibrium or even to form plateaus and be separated.

An important proof-of-principle of ITP downscaling has been delivered by Walker et al.[61], who were the first to demonstrate ITP in a microfluidic device. Since then, many applications of ITP in the microfluidic chip-platform have been reported, as extensively reviewed elsewhere[33,62,63]. Jung et al. showed that concentration factors up to a million times can be achieved due to downscaling to microfluidic dimensions[57]. A systematic theoretical and experimental study demonstrating the advantages of cross-section miniaturization on ITP was performed in microchannels[60]. Electroosmotic flow (EOF) profiles in nanochannels are parabolic[38]. Parabolic flow increases dispersion in microchannels, and for ITP specifically, it increases dispersion from EOF mismatch due to ion density gradients[102,103]. In nanochannels, however, the contribution to dispersion from parabolic flow profiles becomes advantageously insignificant, as reflected in the low Peclet number associated with this scale[46].

Notwithstanding the inherent gain of miniaturization on isotachophoretic performance the micrometer threshold has, to our knowledge, not been crossed in peer-reviewed publications. This stagnation may be explained by the many complications that occur when dealing with sub-micrometer channels, as this scale is dominated by nanoeffects[37–41]. The very large surface-to-volume ratio in a nanochannel increases the influence of the electrochemical double layer (EDL)[48]. When channel dimensions approach that of the EDL, electrophoretic separations of ionic analytes are affected, as separation also occurs based on valence, rather than on mobility only[46,47,104]. The extremely large surface to volume ratio favors chromatographic effects as exploited in nano-chromatography[44]. This influences the apparent electrophoretic mobility and diffusion rates of ions[105] and ampholytes[106]. Furthermore, the surface of siliconoxide nanochannels (e.g. glass) dominates the pH of the solution, as demonstrated by a lowering of the solution pH by 6 units despite the presence of a 1 mol/L TRIS buffer[107].

Since many boundary conditions of isotachophoresis are affected by downscaling to sub-micrometer dimensions, a reconsideration of experimental conditions is required. An important observation is that positive-mode ITP in a negatively charged nanochannel (i.e. glass) can be expected to be seriously hampered due to analyte-wall interactions. Conventionally, ITP ion density gradients are preferably chosen as large as possible to maximize the focusing efficiency, e.g. 1 mol/L for the LE versus 5 mmol/L for the TE[57]. In nanochannels this ratio needs to be as small as possible to circumvent wall-induced titration effects[107]. On the other hand, the fact that ITP is a focusing technique renders it more resilient against nanofluidic dispersion effects than any other electrokinetic separation technique.

In this work we demonstrate the feasibility of ITP in sub micrometer and nanochannels. We present an experimental framework that allows direct translation of conventional capillary separation protocols to sub-micrometer platforms. We show that this approach enables focusing and separation of attomole quantities of amino acids, from a controlled volume of injected sample. Finally, the limits on ITP miniaturization were explored in nanochannels, yielding the discovery of a fundamental boundary on ITP downscaling imposed by the nanoscale dimension.

3.3 Experimental

3.3.1 Chip design & fabrication

Chip devices were made from borofloat glass wafers (SCHOTT AG, Mainz, Germany). In the bottom-side wafer, nanochannels and rulers were made by HF etching[43]. The nano and sub-micron channels were 50 nm deep and 10 µm wide and 330 nm deep and 3 µm wide, respectively. Chip devices consisted exclusively of one channel depth. The depths of the channels were measured with a Dektak 8 mechanical surface profiler (Veeco Instruments Inc. Plainview, USA). Access holes were powderblasted in the bottom-side and top-side wafers. This allows fluidic and electric interfacing from opposite sides. Wafers were placed for several hours in an ultrasonic bath with deionized water. Then the wafers were transferred into 100% HNO_3 and left for 15 min, followed by thorough rinsing with water and finally spin-drying. The wafers were aligned, contacted and fusion bonded at 600 °C for 4 hours. Immediately prior to experiments, the wafers were pre-conditioned at 400 °C for 2 hours in air, improving reproducibility between measurements.

Figure 3.1 shows the layout of the chips. The configuration of channels and access holes incorporates T-junctions (Figure 3.1) that allow a sample volume to be interposed between a leading electrolyte (LE) and a trailing electrolyte (TE) and selection of different injection volumes. A 400 µm injection length corresponds to a volume of 0.2 pL and 0.4 pL, for the nano and sub-microchannel respectively.

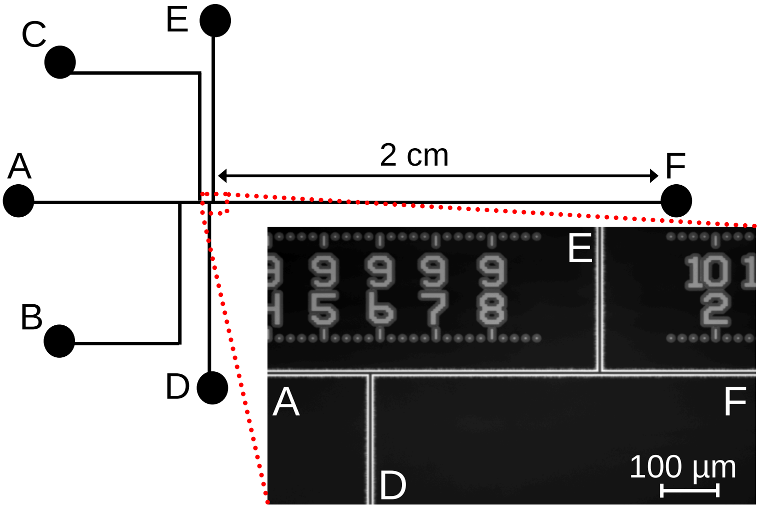

Figure 3.1 Schematic layout of the nanofluidic-ITP chip. A-F designate the access holes, approximately 1 mm in diameter, for placement of electrodes and fluidic access. The insert shows a brightfield image of the injection area where channels D and E intersect with the separation channel, 400 µm apart. The ruler etched along the separation channel, has 20 µm spacing between minor divisions, with the numbers at the major divisions indicating hundreds of microns.

3.3.2 Setup

For on-chip nano-ITP experiments, brightfield and fluorescence imaging was performed with a Olympus BX51WI microscope, equipped with a longpass filter cube (488 nm excitation, 518 nm emission) and a 10x magnification lens, numerical

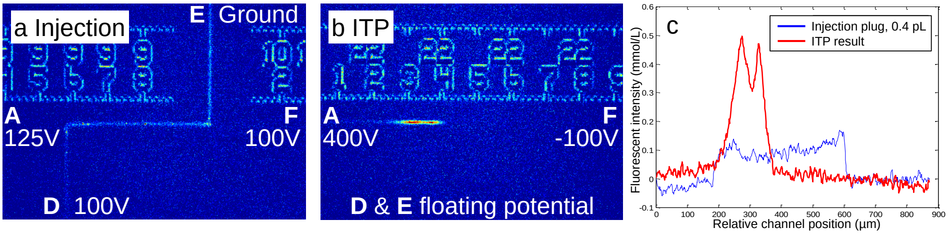

Figure 3.2 On-chip ITP results in 330 nm deep channels for 0.4 pL of yeast matrix spiked with Glu-FITC and Phe-FITC. The letters A, D, E and F refer to the sample reservoirs designated in Figure 3.1, with corresponding voltages applied. a) An injection plug was successfully inserted in between of a leading (left side) and trailing electrolyte (right side). b) Isotachophoretic focusing and separation of Glu-FITC and Phe-FITC into distinguishable peaks. c) Overlay of the injection plug and the separation profile scaled to concentration.

aperture 0.25 (Olympus Corporation, Tokyo, Japan). Electric potentials were applied and monitored using a HSV488 6000D power supply (LabSmith inc., Livermore, USA), controlled through the included Sequence software. Images and movies during experiments were acquired with a Hamamatsu Orca-ER CCD camera and included HoKaWa software (HAMAMATSU Photonics K.K., Japan). Digital (pre) processing and analysis of the data, images and movies was performed using Matlab (MathWorks Inc., Natick, USA).

A custom-built chip interface provided a standardized electrode arrangement from below and reservoirs from the top, aligned with the chip's access holes. The reservoirs were sealed to prevent evaporation and minimize interaction with CO_2 as this influences ITP experiments[108,109].

The movie frames from fluorescence experiments shown in this paper were false coloured for intensity. Intensity profiles from such images were extracted along the separation channel A-F (Figure 3.1), creating an intensity graph.

3.3.3 Isotachophoresis procedure

The amino acids glutamate and phenylalanine labeled with fluorescein isothiocyanate (FITC) were selected as analytes (see Appendix 3.7.1 for labeling and purification procedure). The electrophoretic mobilities of those analytes were determined with capillary zone electrophoresis (see Appendix 3.7.2). Test analytes were spiked to a biomatrix of metabolites extracted from hydrolysate of delipided yeast biomass of *P. pastoris* (see Appendix 3.7.3). The ITP protocol was developed in conventional capillary format (see Appendix 3.7.4). The leading electrolyte (LE) was 10 mmol/L of NaCl and the trailing electrolyte (TE) 5 mmol/L of HEPES. Both electrolytes were adjusted to a pH of 9.50 with sodium hydroxide, verified with a Hanna HI 4521 pH meter (HANNA instruments Inc. Woonsocket,

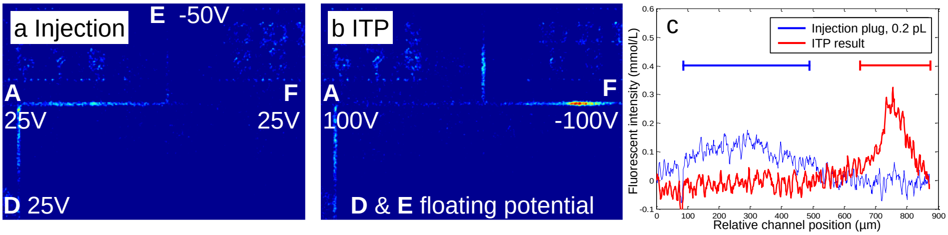

Figure 3.3 On-chip ITP results in 50 nm deep channels for 0.2 pL of yeast matrix spiked with Glu-FITC and Phe-FITC. The letters A, D, E and F refer to the sample reservoirs designated in Figure 1, with corresponding voltages applied. a) An injection plug is successfully inserted in between of a leading (left side) and trailing electrolyte (right side). b) Isotachophoretic focusing of Glu-FITC and Phe-FITC. c) Overlay of the injection plug and the focused zone scaled to concentration. The blue and red bar designate the injection plug length and focused ITP zone length, respectively.

USA) and stored under argon until used [b]. The sample consisted of 70:20:5:5 (v:v:v:v) of TE, yeast cell extract in DMSO, and the fluorescently labeled amino acids phenylalanine and glutamate solutions (1 mmol/L solution in DMSO), respectively. The final concentration of analytes in the sample was 50 µmol/L.

Trailing electrolyte was placed in reservoir F (Figure 3.1), whereupon the channels were filled by capillary action[95], typically within a few minutes. When the chip was completely filled, TE was also applied in well E, LE in well A and the sample solution in well D, wells B and C were left empty. The electrolyte arrangement characteristic for conventional ITP, with the sample volume interposed between the leading and trailing electrolyte was achieved by means of EOF and the double T-structure (Figure 3.1). The appropriate voltage settings on the reservoirs for sample plug formation and those for ITP were obtained empirically and incorporated in an automated protocol of the Labsmith Sequence software. For details and development of the injection procedure see Appendix 3.7.5.

3.4 Results & Discussion

3.4.1 Isotachophoresis in sub-micrometer channels

Figure 3.2 demonstrates an injection, isotachophoretic focusing and separation of 0.4 pL of amino-acid spiked yeast extract in a sub-micron channel (330 nm deep). In order to enable quantitative interpretation of the results we adapted the classical T-injection strategy from electrophoresis chips to our nano-ITP platform. The injection approach used (Appendix 3.7.5) enabled us to achieve a precisely defined injection volume of 0.4 pL as can be seen in Figure 3.2a. This injection

---

[b] Note that HEPES is not in its buffering domain and therefore cannot be considered a buffer, nor is NaCl a buffer. Although buffers should normally be used, this was done to evaluate potential titration from the nanochannel, see introduction

volume was 300,000 times smaller than that used in the experiments in capillary (0.12 µL) and constitutes absolute quantities of 20 attomole of each labeled amino acid. Figure 3.2b shows the downstream focusing and separation of the fluorescently labeled Glu-FITC and Phe-FITC. The fluorescent intensities in the CCD images in Figure 3.2a,b, were extracted and scaled to concentration (see overlay Figure 3.2c). The area under the curve of the sample plug and focused peaks were compared. It was found that the peak area of the ITP result was in roughly qualitative agreement with that of the plug, indicating that the complete injection plug has been focused and no significant losses have occurred.

Figure 3.2 clearly shows that separation was achieved. The profile appears to correspond to peak mode ITP equilibrium. In order to verify this, we injected a larger sample volume of 3.2 pL (Appendix 3.8.1), which showed higher peaks instead of broader plateaus. Separation in peak mode is typically poor. Nevertheless we observe clear distinguishable peaks. The explanation for this is that the biomatrix provides spacer compounds which focus in between the two fluorescent analytes. This was verified by injecting a larger volume (Appendix Figure 3.9) as well as by conventional capillary ITP (Appendix Figure 3.6).

The above result indicates that translation of conventional ITP protocols to sub-micrometer channels is feasible. As a side result, to our knowledge, this work demonstrates for the first time the implementation of a cross T injection for isotachophoresis. Larger injection volumes can easily be facilitated on a chip. An elegant way to incorporate larger sample volumes for ITP is by means of a large cross section followed by a smaller one, combining the higher sample volume compatibility of the larger one with the improved resolving power of the smaller one. This approach was already introduced by Everaerts et al.[53] and its theory and benefits were recently studied extensively[60]. This geometry can be applied for instance to offset dilution from pretreatment, diffusion or world-to-chip interfacing[110] in order to conserve the amount of analyte and still make use of the improved focusing and separation in a nanochannel. A nanochannel as demonstrated here could well be used as the small cross-section part of such a geometry.

The miniaturization of analysis techniques for sub-pL sample volumes is of great importance in biological and clinical applications. Firstly, extraction of such small volumes is expected to reduce invasiveness; lower sample consumption allows increased temporal resolution of processes measurements and/or multiple parallel studies on conventional sample volumes. Particularly the analysis of single cells is an important example, promising unprecedented insights in cell biology[111,112]. Whole cell analysis has motivated the miniaturization of analysis platforms[113,114], for which electrophoretic techniques were successfully applied[115–119]. The results in this paper, for absolute quantities of 20 attomole of each analyte in a biomatrix can be directly translated to whole cell ITP analysis of a 25 µm cell, for analytes at a concentration of $\approx$ 2.5 µmol/L. However, to study a cell's intracellular time-resolved metabolism, in e.g., cellular division, apoptosis, differentiation, or its response to drugs and stress, time resolved analysis

Figure 3.4 Brightfield image of bubbles in a 50 nanometer deep channel, visible as brighter regions, formed during ITP, during ITP at 500 V. in the 50 nm deep channel.

of sub-cellular aliquots is required. Thus the bioanalyis of sub picoliter sample volumes and resolving the correspondingly low amounts of analytes is an important challenge. The 0.4 pL of injection volume demonstrated here corresponds directly to a sample volume of 5% from a 25 micron cell. Analysis of such minute quantities and volumes as shown here represents the achievement of an important downscaling milestone and indicates that nano-ITP has great potential as the separation component in a single cell or subcellular aliquot analysis platform.

3.4.2 Isotachophoresis in nanochannels

To investigate the limit of downscaling, we performed ITP in a fluidic chip consisting exclusively of nanochannels (50 nm deep) (see Figure 3.3 and Appendix 3.8.3). Concentrations and composition of sample were identical to those used in Figure 3.2. As can be seen in Figure 3.3a and b, sample injection could be performed followed by isotachophoretic focusing. Unfortunately we were not able to inject the complete sample volume. Based on the overlay in Figure 3.3c, we estimate an injection loss of 42%. A separation into separate peaks could not be observed for the voltages used here. Application of higher voltages (500 V) in this channel depth lead to bubble formation in the channel (see Figure 3.4).

Given the extremely high surface to volume ratio and corresponding efficient heat transfer plus the fact that we did not observe bubble formation at this voltage in larger channels, allows the conclusion that this phenomenon is unlikely to result solely from Joule heating effects. The phenomenon of bubble formation is likely explained by cavitation, induced by extreme pressure gradients originating from EOF mismatch between electrolyte zones in nanochannels. As such it may not only affect ITP in nanochannels, but other techniques using concentration gradients as well. First findings on electrocavitation have been reported[120], and a full paper is in preparation.

Table 3.1 compares conditions and results achieved for the sub-micron channels and the nanochannels. For 200 V, isotachophoretic focusing, but not separation, was demonstrated in sub-micron channels (Appendix Figure 3.10) as well as in nanochannels (Figure 3.3). In sub-micrometer channels both focusing and separation could be achieved for potentials of 500 V. In the nanochannels such higher voltages lead to the formation of bubbles, and separation could not be demonstrated. The 500 V applied for 330 nm deep channels also represents an upper limit, above which bubble formation occurred. This corresponds to 75% of the electric field used in capillary ITP (Appendix 3.7.4). Nonetheless, in contrast to the nanochannels, the applicable potential was still sufficient for separation. These results indicate that a limit of downscaling for ITP using standard protocols is reached.

Table 3.1 Summary of ITP settings for sub-micron and nanochannels and their corresponding performance.

Channel depth	Injected vol.	Potential	Focusing	Separation
330 nm	0.4 pL	200 V	yes	no
330 nm	0.4 pL	500 V	yes	yes
50 nm	0.2 pL	200 V	yes	no
50 nm	0.2 pL	500 V	bubble formation	bubble formation

3.5 Conclusions & Perspectives

In this paper we have investigated the scalability of conventional ITP into the nanofluidic domain. We have shown isotachophoretic focusing and separation in sub-micrometer channels, which, to our knowledge, represents the smallest demonstration of ITP focusing and separation to date, both in terms channel dimension and injection volume. Separation was performed in the presence of a biomatrix, demonstrating real-sample compatibility. Also, the concept of ITP spacers was shown to be conserved. A controlled quantitative injection scheme based on a double-T geometry was for the first time implemented for ITP, demonstrating that quantitative assessment of analyte composition is feasible. Subsequently, we demonstrated isotachophoretic focusing in 50 nm deep channels. Separation, however, could not be achieved as the applicable voltage was restricted by bubble formation in the channel. Despite successfully circumventing known nanodimension complications, we encountered an unexpected limit of ITP efficiency upon downscaling. Future research will focus on a more precise assessment of the restrictions on ITP miniaturization, including the origins of the bubble formation. Last but not least, we have shown the applicability of ITP to subcellular volumes containing attomoles of analyte and will continue our efforts to enable a subcellular analysis platform by means of low volume ITP. Despite the miniaturization limit reported here, ITP remains best positioned for effective downscaling and bioanalysis of ultra low compound quantities.

3.6 Acknowledgements

We gratefully acknowledge Raphaël C.T. Zwier from the Department of Fine Mechanics (Leiden University, The Netherlands) for his skilled and extensive work on the interfacing. Professor Rainer Bisschof (Groningen University, The Netherlands) is thanked for giving us the PACE system. Dr. Tatjana Egorova (Protein Labeling Innovation, Leiden, The Netherlands) is acknowledged for supplying the yeast sample. This project was financed by NanoNed, an initiative of the Dutch Science and Technology Foundation (STW), the Netherlands Metabolomics Centre, the Netherlands Genomics Initiative and the Netherlands Organization for Scientific Research (NWO).

3.7 Appendix, Methods

3.7.1 Fluorophore labeling of amino acids

All chemicals were acquired from Sigma-Aldrich Co. (Zwijndrecht, The Netherlands), unless noted otherwise. Labeling of glutamate, phenylalanine, and leucine with fluorescein isothiocyanate (FITC) was performed as follows. To 0.5 mmol of amino acid an aqueous solution of potassium hydroxide, 1 g/ml, was added in a ratio of 1:1 (weight:volume), followed by addition of 1 ml of ethanol. Under vigorous stirring, on ice, a suspension of FITC, 1 mol/L in ethanol was added to the amino acid 1:1 (mol:mol) together with 1 ml 0.5 mol/L potassium hydroxide and 0.5 mL ethanol. This mixture was left on ice to react for 2 h in the dark under continued stirring. Purification of the reaction product was performed using a Gilson preparative HPLC system (Gilson, Inc., Middleton, USA) equipped with a Phenomex Gemini C18 column, 15x21 mm, 5 micron (Phenomenex, Torrance, USA) using an acetonitrile/water (10 mmol/L ammonium acetate, pH = 8) gradient. Purity of compounds was established with liquid chromatograpy ultraviolet mass spectrometry (LC-UV-MS) and CZE-LIF and found to be $>$99%. After freeze-drying, each purified FITC-amino was dissolved in dimethyl sulfoxide (DMSO), 1 mmol/L, and stored at -80 °C awaiting experiments.

FITC, having a pKa of 6.7[92], fluoresces strongly when negatively charged at valence -2. FITC labeled biosamples are of general interest. FITC-labeled amino acids have been studied with CZE[24,121,122] chip ZE[32,123] and ITP in capillary[124–126] and microchannels[127] as well as other techniques[128]. As unpurified reaction product is used almost exclusively in these publications, the two most abundant fluorescent by-products of this labeling are considered to be of interest and were purified and identified with LC-UV-MS (Data not shown). One reaction by-product consisted of FITC where its isothiocyanate group (-N=C=S) was degraded to an amine, which in turn reacted with FITC thus forming a fluorescent dimer (MW 737). As degraded FITC was low abundant in the reaction mixture this implied that the degradation was slower than the reaction with another FITC molecule. This dimer has an almost 4 times lower fluorescent intensity (at 488 nm excitation, 514 nm emission) compared to FITC, due in part to a shifted fluorescence wavelength optimum. The other abundant by-product (MW 436) was FITC that had reacted with ethanol ($-N=C-S-O-C_2H_5$). FITC is commonly dissolved in ethanol, but our data suggests this should be avoided.

3.7.2 Capillary electrophoresis

A PACE 5000 capillary electrophoresis apparatus equipped with laser-induced-fluorescence detection, operating at 488 nm excitation and 518 nm emission (Beckman Instruments, USA) was used for CZE. CZE was applied to determine the mobilities of the FITC-amino acids as well as establishing their purity for the purpose of fluorescence measurements. The temperature during all experiments

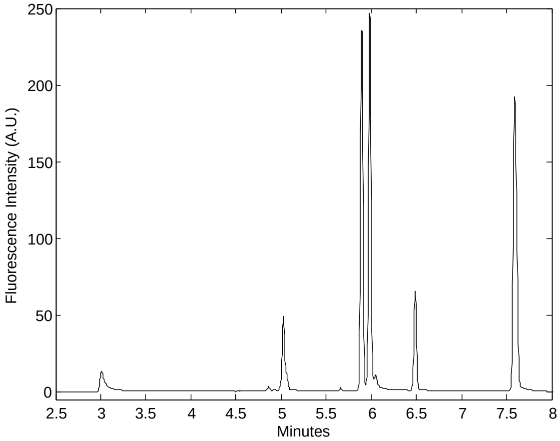

Figure 3.5 Typical CZE electropherogram of labeled amino acids and FITC by-products. From left to right first at 3 minutes the EOF marker bodipy is seen, then FITC-ethanol, leucine-FITC, phenylalanine-FITC , fluorescein amine-FITC and glutamate-FITC, all except FITC-Ethanol at 10 µmol/L.

was maintained at 25 °C by the instrument thermostat. The fused silica capillary (Inacom Instruments, Overberg, The Netherlands) used for CZE had a 50 µm inner diameter and a total length of 56.9 cm measuring 50.3 cm from inlet to detector. Runs were performed at 20 kV, giving a typical current of 14.4 ± 0.1 µA during runs. The background electrolyte was a 10 mmol/L solution of disodium tetraborate ($Na_2B_4O_7$). It was adjusted to pH = 9.50 with sodium hydroxide solution (to ensure maximum fluorescence intensity of fluorescein, as this is pH dependent pKa = 6.7[92]), verified with a Hanna HI 4521 pH meter (milli-pH unit resolution, HANNA instruments Inc. Woonsocket, USA). As a marker for the electro-osmotic flow (EOF) the uncharged fluorophore 4,4-difluoro-4-bora-3a,4a-diaza-s-indacene (bodipy), was added.

CZE of the labeled amino acids and the two reaction by-products was performed establishing their purity for fluorescence measurements (Appendix Figure 3.5). Their calculated electrophoretic mobilities are given in Table 3.2. Based on their mobility phenylalanine-FITC and glutamate-FITC were selected for the ITP protocol, as their difference increased the potential of spacing by compounds in the yeast biomatrix. As ITP electrolytes, chloride was chosen as leading ion, 4-(2-hydroxyethyl)-1-piperazine-ethanesulfonic acid (HEPES) as trailing ion and sodium as the common counterion (See Table 3.2).

3.7.3 Yeast pretreatment for metabolite extraction

To hydrolysate of delipided yeast biomass of *P. pastoris* (YPp(N)-HyBm1, Protein Labeling Innovation PLI, Leiden, The Netherlands) cold (-20 °C) 80:20 methanol:

Table 3.2 Electrophoretic mobilities (µ) and valences at pH 9.5 of the FITC labeled amino acids, FITC by-products and the ions in the ITP electrolytes.

Ion	valence	µ $(10^{-9}\mathrm{m}^2\mathrm{V}^{-1}\mathrm{s}^{-1})$
HEPES[56],(trailing ion)	-1	-21.8
FITC-ethanol	-2	-31.5
Leucine-FITC	-3	-38.4
Phenylalanine-FITC	-3	-39.0
Fluorescein amine-FITC	-4	-42.0
Glutamate-FITC	-4	-47.3
Chloride[55], (leading ion)	-1	-79.1
Sodium[55], (counter ion)	+1	51.9

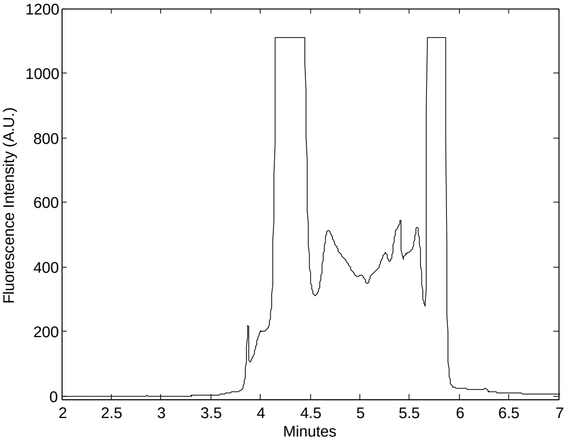

Figure 3.6 Capillary-ITP for a 0.12 µL sample of yeast biomatrix and 5 glutamate-FITC and phenylalanine-FITC both 50 µmol/L. The measurement using LIF shows from left to right, Phe-FITC and Glu-FITC, spaced by the yeast biomatrix, with TE to the left and LE to the right of the sample.

water was added. After placement for 30 minutes in an ultrasonic bath, this mixture was centrifuged and the supernatant collected. This extraction procedure was repeated and the combined supernatants were freeze-dried, after removal of methanol. These extracted compounds were redissolved in dimethyl sulfoxide (DMSO) to 10 mg/mL (relative to the original weight of the hydrolysate prior to pretreatment) and stored at -80 °C awaiting experiments.

3.7.4 Isotachophoresis protocol development in capillary

A PACE 5000 capillary electrophoresis apparatus equipped with laser-induced-fluorescence detection, operating at 488 nm excitation and 518 nm emission (Beckman Instruments, USA) was used for ITP experiments. The temperature during all experiments was maintained at 25 °C by the instrument thermostat.

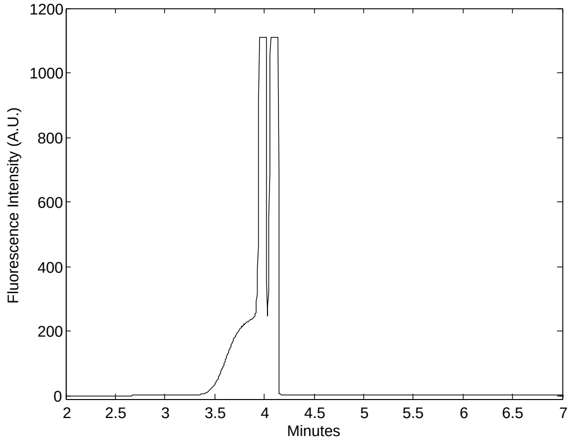

Figure 3.7 Capillary-ITP result for a 0.12 µL sample containing glutamate-FITC and phenylalanine-FITC both 50 µmol/L. The measurement using LIF shows from left to right, Phe-FITC and Glu-FITC, shown to be concentrated so far as to saturate the detector (>250 µmol/L).

The developed protocol for capillary ITP was as follows. ITP electrolytes were introduced into the fused silica capillary (27.22 cm total length, 20.38 cm from inlet to detector, 50 µm ID; Inacom Instruments, Overberg, The Netherlands) by pressure. The capillary was first flushed with trailing electrolyte (TE), 5 mmol/L of HEPES. A plug of sample was then injected, consisted of 80:20:10 TE:pretreated yeast extract:labeled amino acid solutions (v:v:v, final concentration of each amino acid 50 µmol/L) by applied pressure of 0.5 psi for 60 s which according to the Hagen-Poiseulle equation corresponds to a volume of 0.12 µL or 20% of the total capillary (6 cm). Lastly that end of the capillary was placed in a vial with leading electrolyte (LE), 10 mmol/L of NaCl, the other in one with TE. ITP was then induced by applying 5 kV. The electrolytes were prepared anew in deionized water each day, adjusted to pH 9.50 with sodium hydroxide, and stored under argon until used. Vials for experiments were covered with caps containing septa. Although sample ions migrated opposite to the EOF, at pH 9.50 the EOF was dominant. For ITP this is an advantage as more time is available to equilibrate before the analytes pass the detector.

A typical capillary ITP result is shown in Figure 3.6. Equilibrium formation could be concluded from the current during the run[129]. Spacing is seen between the bands of Glu-FITC and Phe-FITC. ITP of just the labeled amino acids only, does not show spacing (Appendix Figure 3.7). ITP of yeast alone shows negligible native fluorescence (Appendix Figure 3.11). From ITP results of each of the amino acids alone (Appendix Figures 3.12 & 3.13), showing single zones, and in the presence of yeast extract (Appendix Figures 3.14 & 3.15) showing added bands for Phe-FITC, it may be concluded that the fluorescence observed in the spacing is from Phe-FITC that interacted with compounds in the yeast biomatrix.

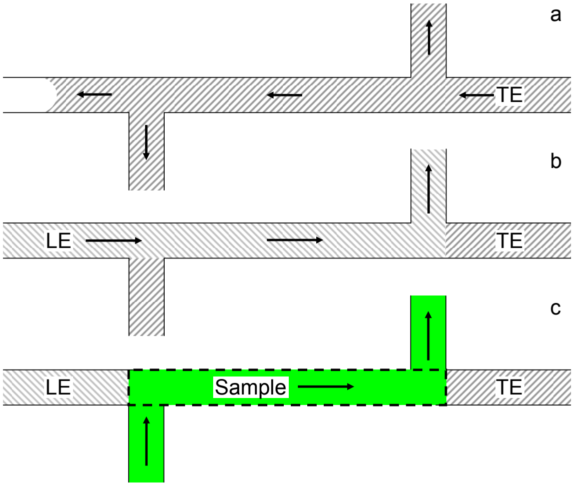

Figure 3.8 On-chip double-T injection for quantitative ITP. a) The chip is filled with trailing electrolyte by capillary filling. b) After placement of the other electrolytes in the wells, leading electrolyte is flushed towards well E, which serves as waste reservoir. c) The sample volume in the nanochannel chip (dashed box), is created by means of an exclusive EOF, from sample well D to waste E. Appropriate empirical voltage settings correspond to contanement of the fluorescence between the side channels. Settings were found to vary per channel depth. After an ITP experiment, the injection plug can be recreated by directly re-applying the sample injection voltages, e.g. those given in Figures 3.2 & 3.3.

3.7.5 Chip injection protocol

Effectively translating quantitative ITP to the nano-chip format requires a well defined sample injection volume, to be interposed between a leading electrolyte (LE) and a trailing electrolyte (TE). Here, on chip T-junctions were used in combination with EOF, see Figure 3.1. The appropriate voltage settings on the reservoirs for sample plug formation and those for ITP, were obtained empirically by observing the effects of manual voltage changes with the fluorescence microscope, see Appendix Figure 3.8 for details. The voltage settings used for the submicron channels are tabulated in Table 3.3 and those for the nanochannels in Table 3.3. These were incorporated in an automated protocol of the Labsmith Sequence software to execute the fast and/or simultaneous stepwise voltage changes required.

Table 3.3 ITP voltage steps used for 3 µm wide, 330 nm deep channels.

Well	Sample plug Figure 3.2a	Pre ITP 100 ms	ITP, Appendix Figure 3.10	ITP final Figure 3.2b
A LE	125 V	125 V	100 V	400 V
D Sample	100 V	0 V	float	float
E TE, waste	0 V	0 V	float	float
F TE	100 V	100 V	-100 V	-100 V

Table 3.4 ITP voltage steps used for 10 µm wide, 50 nm deep channels.

Well	Sample plug Figure 3.3a	ITP Figure 3.3b
A LE	25 V	100 V
D Sample	25 V	float
E TE, waste	-50 V	float
F TE	25 V	-100 V

For a nano-ITP experiment first the sample plug creation step was activated. Typically after a few minutes the plug would reform and traces of fluorescence in the separation channel were removed, allowing repeated experiments. When the stable plug was observed the ITP step was initiated manually. ITP itself was automatically preceded by a pre-ITP step of 100 ms. The pre-ITP step was needed to actively regulate the electrode in well D to zero, when set to float directly the Voltage would decrease to 0 V on a time scale of a few seconds, affecting injection accuracy. Afterwards the Voltage on well A could be increased manually to increase separation, as was done in the results in Figure 3.2b.

Implementation of the voltage settings was non-trivial and only feasible with fast and accurate computer control of the applied voltages. Switching without losing or extracting sample into or from the sidechannels proved the most critical step, being the main source of injection errors.

3.8 Appendix, Results

3.8.1 Large sample volume injections in sub-micron channels

ITP experiments were also performed on larger sample volumes, e.g. 3.2 pL (Appendix Figure 3.9). The ITP result for this larger volume demonstrated increased peak height and spacing, compared to results with smaller sample volumes (Figure 3.2). This indicates that the ITP results in Figure 3.2b & 3.3b correspond to so-called peak mode ITP[58], in contrast to plateau-mode in which case more analyte leads only to broadening of the zones[53,55]. Therefore, if more absolute amount of compound would be injected, even higher equilibrium concentrations can be expected. However, this requires either higher initial concentrations ($>$50 µmol/L) or injecting even larger volumes.

3.8.2 ITP in submicron channels at 200 V

Figure 3.10 shows the result of ITP in a 330 nm deep channel for an applied Voltage of 200 V. This result is with the injection shown in Figure 3.2a, demonstrating that 200 V is sufficient for isotachophoretic focussing but is insufficient to separate

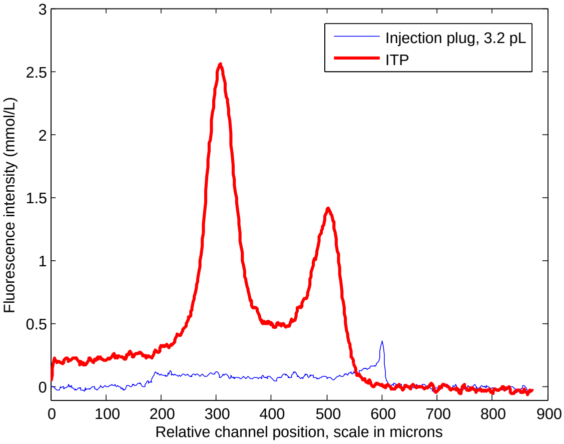

Figure 3.9 ITP result in a 330 nm deep channel. Based on the areas under the curves, the ITP result corresponds to an injection of 3.2 pL. This larger injection volume resulted in higher peaks and more spacing compared to the 0.4 pL sample in Figure 3.2c.

the amino acids. By subsequently increasing the voltage during the experiment to 500 V the separation result shown in Figure 3.2b was achieved.

3.8.3 Movie of nano ITP in a 50 nm deep channel

NanoITP.avi, in false color, background corrected and filtered. Provided in the Electronic Supporting Information of the paper this chapter was adapted from[130]

3.8.4 Additional capillary ITP Figures

Additional Figures as referenced to in section 6.4.

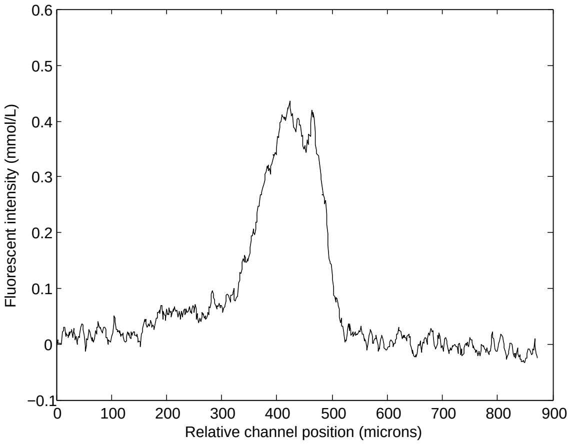

Figure 3.10 ITP foccussing result in a 330 nm deep channel, part of the same experiment as in Figure 3.2. The applied voltage difference of 200V (A = 100 V, F = -100 V).

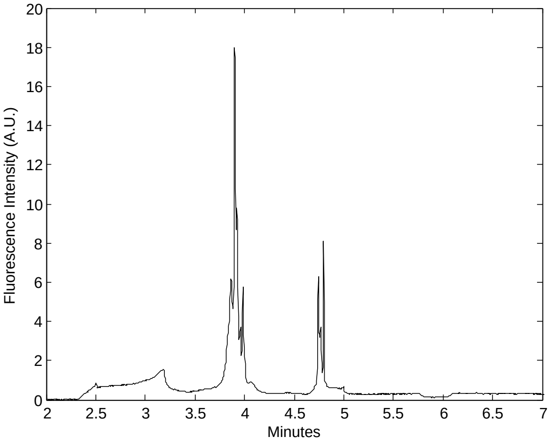

Figure 3.11 Graph showing the capillary-ITP result of yeast extract, same protocol as used for Figure 3.6.

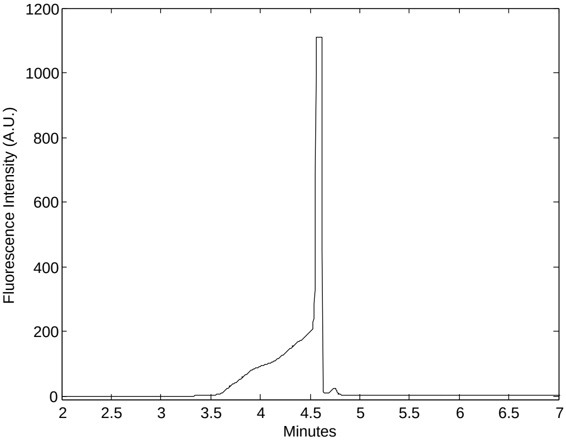

Figure 3.12 Graph showing the capillary-ITP result with 50 µmol/L phenylalanine-FITC same protocol as used for Figure 3.6.

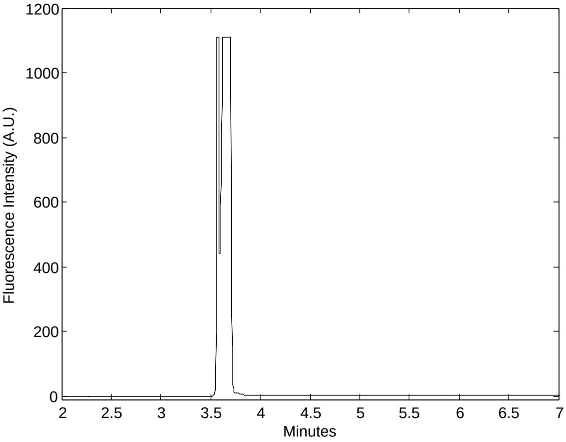

Figure 3.13 Graph showing the capillary-ITP result with 50 µmol/L glutamate-FITC same protocol as used for Figure 3.6.

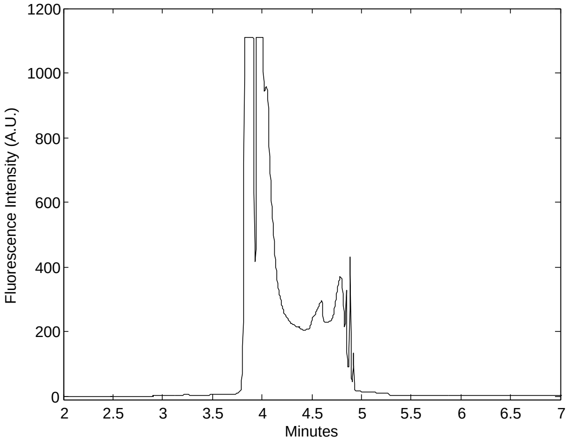

Figure 3.14 Graph showing the capillary-ITP result with 50 µmol/L phenylalanine-FITC in presence of yeast extract, same protocol as used for Figure 3.6. Clearly showing the interaction of phenylalanine-FITC with the biomatrix.

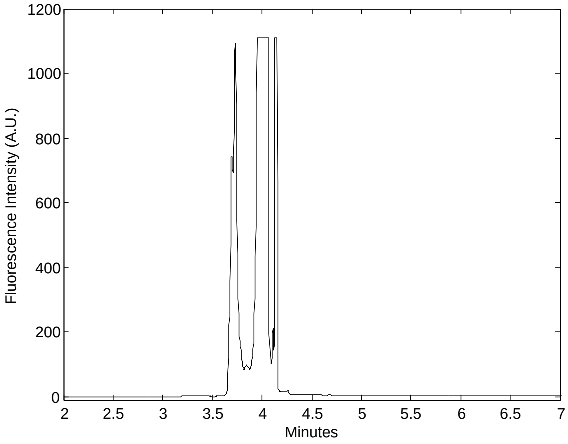

Figure 3.15 Graph showing the capillary-ITP result with 50 µmol/L glutamate-FITC in presence of yeast extract, same protocol as used for Figure 3.6.

CHAPTER 4

Single-Electrolyte Isotachophoresis Using a Nanochannel-Induced Depletion Zone[a]

4.1 Abstract

Isotachophoretic separations are triggered at the border of a nanochannel-induced ion-depleted zone. This depletion zone acts as a terminating electrolyte and is created by concentration polarization over the nanochannel. We show both continuous and discrete sample injections as well as separation of up to four analytes. Continuous injection of a spacer compound was used for selective analyte elution. Zones were kept focused for over one hour, while shifting less than 700 µm. Moreover, zones could be deliberately positioned in the separation channel and focusing strength could be precisely tuned employing a three-point voltage actuation scheme. This makes depletion zone isotachophoresis (dzITP) a fully controllable single-electrolyte focusing and separation technique. For on-chip electrokinetic methods, dzITP sets a new standard in terms of versatility and operational simplicity.

---

[a] Published as: Jos Quist†, Kjeld G. H.Janssen†, Paul Vulto, Thomas Hankemeier and Heiko J. van der Linden, *Analytical Chemistry*, **83**, 7910-7915 (2011)

† Equally contributing authors.

4.2 Introduction

Isotachophoresis (ITP) is a powerful electrokinetic technique for the concentration, separation, purification and quantification of ionic analytes, especially when downscaled to microfluidic devices[33,131]. In 1998, Walker et al. were among the first to demonstrate on-chip ITP using Raman spectroscopy to detect herbicides[61]. Kanianski et al. coupled ITP to capillary electrophoresis (CE) on a chip and showed isotachopherograms of up to 14 analytes[132]. Several reports describe over 10,000-fold concentration[133–135]. Jung et al. even reported millionfold sample stacking using transient ITP[57]. Miniaturized ITP is applicable to a broad range of samples, including toxins from tap water[59], explosive residues[136], proteins[137], DNA from PCR samples[138,139], nucleic acids from whole blood[140] and small RNA molecules from cell lysate[141]. Hybridization of RNA's with molecular beacons by ITP[142] was applied to bacterial rRNA's from urine[143], demonstrating the potential of on-chip ITP for biochemical assays. A major recent achievement was the integration of an ITP chip and laser-induced-fluorescence (LIF) detection into a single handheld device[144]. Nevertheless, ITP has still to come to its full potential, as until now it has not been widely used for bioanalytical applications[145–147]. A major limitation is that ITP requires a sample to be injected between a leading electrolyte and a terminating electrolyte. Compared to e.g. capillary electrophoresis (CE), which uses a single electrolyte only, handling and method development is not straightforward. Another limitation of conventional ITP is that analyte zone positions are difficult to control. This is due to the different conductivities of the ITP zones, resulting in continuous changes of electric field distributions during electromigration. Several stationary ITP strategies have been developed to alleviate this limitation. One such strategy employs a hydrodynamic counterflow, but this has the disadvantage of dispersion due to a parabolic flow profile[148]. A more elegant strategy is balancing the electrophoretic motion of the ITP zones by an opposite electro-osmotic flow (EOF)[149–152]. However, with this method it is still complicated to change analyte zone positions in a controlled manner without changing pH or electrolyte concentrations.

In this paper we overcome the mentioned limitations by a radically different approach which combines the strengths of on-chip ITP with the merits of nanofluidic concentration devices[65,153]. These devices, which have been extensively reviewed by Kim et al.[68], are in fact miniaturized variants of electrocapture devices. Electrocapture is a powerful method which utilizes capillaries with perm-selective membrane junctions for trapping and selective release of ionic compounds[154,155]. In nanofluidic concentration devices, at least two parallel microchannels are connected by a nanochannel, over which an electric field is applied (Figure 4.1a). Asymmetric distribution of anions and cations[107,156] makes the nanochannel perm-selective, leading to concentration polarization[49,50,157]. This causes the formation of a depletion zone in the anodic microchannel. A tangential EOF through this microchannel transports analytes towards the border of the depletion zone, where they are trapped (Figure 4.1b). Various groups have investigated devices based on similar principles[51,158–163], showing that this has become a very active research field within a short time. Potential applications include immunoassays[164–167], enzyme assays[167–169], massive parallelization[170,171] and desalination[172]. Here we employ a depletion zone to induce isotachophoretic separations. To our knowledge, this is the first time such separations are demonstrated in nanofluidic concentration devices. Depletion zone isotachophoresis (dzITP), as we coin this novel approach, is performed with a single electrolyte only. A three-point voltage actuation scheme gives complete control over the position of the zones and the sharpness of their borders, utilizing the fact that the method is quasi-static. The simplicity and versatility of our method makes it a powerful new tool in the electrokinetic focusing and separation toolkit.

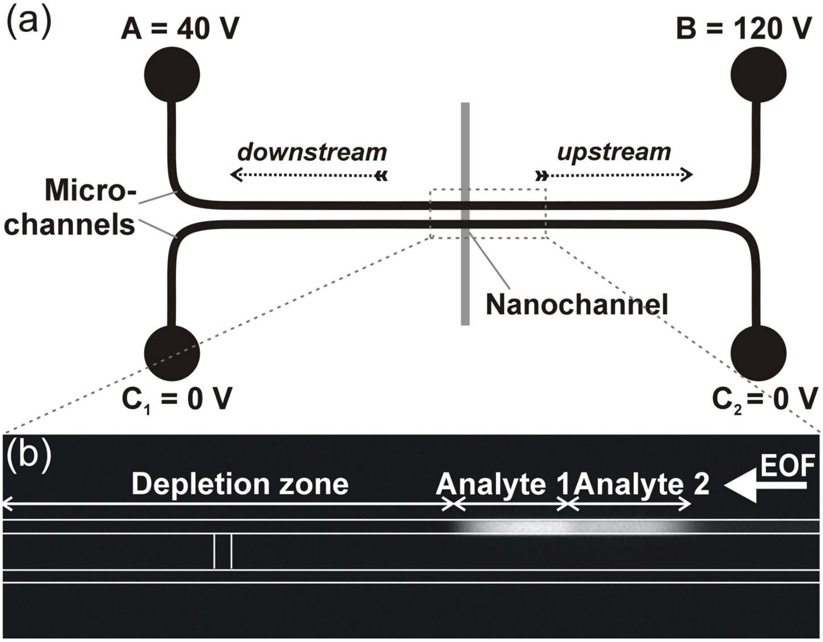

Figure 4.1 a) Chip layout consisting of two microchannels and one nanochannel. An example of three-point voltage actuation is provided: A is the downstream voltage, B the upstream voltage, while the lower channel is connected to ground, as represented by voltages $C_{1,2}$ = 0 V. Downstream and upstream directions are indicated by dashed arrows. b) Example of dzITP separated zones. The channel contains a depletion zone that extends mostly in the downstream channel. Analytes focus at the border of the depletion zone and order themselves in clearly distinguishable zones. Lines that indicate micro- and nanochannels were drawn onto the CCD image.

4.3 Experimental

4.3.1 Chemicals

Lithium carbonate was obtained from Acros Organics (Geel, Belgium); disodium fluorescein was obtained from Riedel-de Haën (Seelze, Germany); 6-carboxyfluorescein was obtained from Sigma-Aldrich (Steinheim, Germany); and sodium acetate was obtained from Merck (Darmstadt, Germany). FITC-labeled amino acids were synthesized as described in Section 3.7.1. In all experiments, 2.0 mmol/L lithium carbonate, pH 10.6 was used as the background electrolyte. Solutions were prepared fresh before experiments.

4.3.2 Chip preparation

Chips were fabricated in Pyrex® wafers using standard lithography techniques and deep reactive ion etching (DRIE). The chip fabrication procedure is described in detail in the appendix Section 4.7.2. The microchannels had 1.7 µm depth and 20 µm width. Microchannel lengths between fluid reservoirs and the nanochannel were 0.91 cm. The nanochannel that connected the two microchannels was 60 nm deep, 25 µm wide and 50 µm long. The chip was prefilled with ethanol to eliminate air trapping, after which the chip was flushed at least 15 minutes with 100 mmol/L NaOH, 15 minutes with demineralized water and 15 minutes with background electrolyte (2.0 mmol/L lithium carbonate). Fluid replacement and flushing was accomplished by leaving the fluid reservoir at one end of a microchannel empty. A combination of capillary action and evaporation of fluid generated a flow which was sufficient to replace all fluid in a microchannel in approximately 3 minutes. Reservoirs were washed 3 times after fluid replacement. After flushing, all channels and reservoirs were filled with the background electrolyte (2.0 mmol/L lithium carbonate).

4.3.3 Setup and microscopy

Access holes were extended with fluidic reservoirs (volume 100 µL) using a custom-build interface that was attached to the chip surface using a vacuum. The fluidic reservoirs were electrically connected using gold electrodes. Two power supplies (ES 0300 045, Delta Elektronika BV, Zierikzee, The Netherlands) were controlled via the analog outputs of an NI USB 6221 data acquisition system using LabVIEW 8.2 software (National Instruments, Austin, TX). For fluorescence microscopy, an Olympus IX71 microscope (Olympus, Zoeterwoude, The Netherlands) was used in combination with an Hamamatsu Orca-ER digital camera and Hokawo version 2.1 imaging software (Hamamatsu Photonics, Nuremberg, Germany). The magnification was 40x. To minimize photobleaching, low lamp intensities were combined with 1.0 second integration times.

4.3.4 Data processing

Spatiotemporal plots (Figure 4.2) were composed using MATLAB®, by adjoining fluorescence profiles obtained from image sequences that were recorded during the experiments. Fluorescence profiles were obtained by averaging 50 image lines and correcting them for background signal. False colors were assigned to represent fluorescence intensity. Raw CCD images were used in Figure 4.3. Fluorescence profiles were obtained from the CCD images and were smoothed by averaging over 5 pixels. Slope values were determined at the inflection points of the smoothed profiles and normalized with respect to the maximum intensity value of the corresponding analyte zone. Locations of the edges of the zones were obtained by determining the position of the inflection point relative to the upstream edge of the nanochannel.

4.4 Results and Discussion

4.4.1 Device operation

4.1a and b show the general device operation for dzITP. The upper channel in Figure 1a, b is the separation channel, this is the channel where isotachophoretic zones are formed during the experiment. Three-point voltage actuation is utilized: to each of the access holes of the separation channel a voltage source is connected, while the other channel is connected to ground. Upon voltage application, concentration polarization takes place: an ion depletion zone forms in the separation channel, while in the other channel an ion enrichment zone forms (not shown here, see ref. 29). Asymmetric voltage application over the separation channel yields an EOF through this channel. The channel arm between the higher voltage and the nanochannel is referred to as the ”upstream channel”, while the arm between the lower voltage and the nanochannel is referred to as the ”downstream channel” (see Figure 1a). Downstream, the depletion zone continues to grow until the fluid reservoir is reached. This process sometimes appears to lead to fluctuations during the first 30-60 seconds of an experiment. In the upstream direction, depletion zone growth becomes balanced by the opposing EOF. When the downstream depletion zone reaches the outlet, the electrical resistance in this channel reaches a more stable value, resulting in a near-stable position for the upstream depletion zone border. At this border, analytes are focused based on a difference in ion density (for detailed theory see Zangle et al.[50]). Meanwhile, analyte concentration and separation into adjacent zones is achieved according to isotachophoretic principles (see Figure 4.1b). The depletion zone serves here as a terminating electrolyte, the background electrolyte takes the function of the leading electrolyte. They define the ionic mobility window of analytes that can be focused. The upper boundary of this mobility window is defined by the mobility of the leading ion in the background electrolyte: analytes with higher mobilities will be transported towards the reservoir. The lower boundary depends on the electric field in the depletion zone, which is very high. For example, Kim et al measured a 30-fold amplified electric field in the depletion zone[173]. Only analytes with very low mobilities are transported through this barrier by EOF transport.

As the current setup is based on a glass chip, the channels have a negative surface charge. Consequently, only anions are focused and separated at the depletion zone border. In order to enable focusing and separation of cations, the surface charge of the device should be reversed by applying a surface coating or by choosing a different substrate.

4.4.2 Discrete and continuous injections

dzITP is demonstrated for both discrete and continuous injections (see Figure 4.2a, b). Fluorescein, 50 µmol/L and 6-carboxyfluorescein, 50 µmol/L were used as analytes; applied voltages were 120 V (upstream) and 40 V (downstream). For discrete injections, only the separation channel was filled with sample, while remaining channels and fluid reservoirs contained background electrolyte only. This resulted in a 309 pL injection volume, as calculated from the microchannel dimensions. Figure 4.2a shows that isotachophoretic separation continues until all analytes from the discrete sample are focused, after which the zone widths become constant. Over time, bending points can be observed in the growth rate of the analyte zones, as indicated by the arrows in Figure 4.2a. These bending points correspond to the exhaustion of fluorescein (arrow I) and 6-carboxyfluorescein (arrow II). Lower mobility compounds are exhausted at an earlier stage than compounds of higher mobility, the reason being that lower mobility compounds have a lower electrophoretic drift to counter the EOF, resulting in a higher net velocity. In continuous injections, the analytes were also placed in the upstream fluid reservoir, providing a practically inexhaustible supply of analytes. Therefore zone broadening was continuous (see Figure 4.2b). Clearly, no bends due to analyte exhaustion were present. Zone broadening speed of the lower mobility compound (fluorescein) is higher than for the higher mobility compound (6-carboxyfluorescein), again due to a higher net velocity. Continuous injections are therefore most advantageous for the extraction and focusing of low-concentration, low-mobility analytes, while discrete injections are useful in the quantitative analysis of multiple analytes.

4.4.3 Four-compound separation

4.2c shows concentration and separation of four compounds. A discrete sample containing fluorescein, 6-carboxyfluorescein, FITC-leucine and FITC-glutamate, 40 µmol/L each, was injected. External voltages were 120 V (upstream) and 40 V (downstream). Within 100 seconds, four zones of clearly distinguishable fluorescence intensity were formed. Standard addition was used to assign the

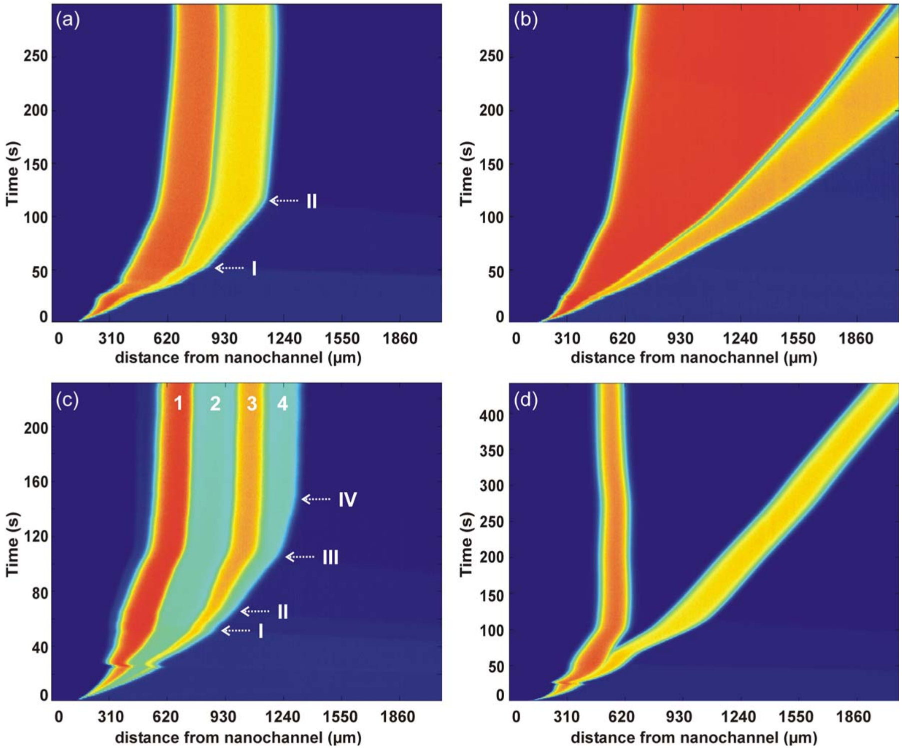

Figure 4.2 Spatiotemporal plots of dzITP separations. a) Discrete injection of fluorescein and 6-carboxyfluorescein. Arrows I and II indicate exhaustion of fluorescein and 6-carboxyfluorescein respectively. b) Continuous injection of fluorescein and 6-carboxyfluorescein. c) Discrete injection and separation of four compounds: fluorescein (1), FITC-leucine (2), 6-carboxyfluorescein (3) and FITC-glutamate (4). Arrows I-IV indicate exhaustion of these respective analytes. d) Discrete injection of fluorescein and 6-carboxyfluorescein combined with a continuous injection of acetate.

four zones to each of the four analytes: a doubled concentration of the respective analyte led approximately to a doubling of the width of the corresponding zone (see appendix 4.7.3). Here, too, bends in the profile coincide with the exhaustion of each of the respective analytes.

4.4.4 Spacer compounds

A combination of a continuous and a discrete injection is shown in Figure 4.2d. The upstream fluid reservoir was filled with electrolyte containing 100 µmol/L sodium acetate as a spacer compound, but no analytes. The separation channel was filled with electrolyte containing 30 µmol/L of both fluorescein and 6-carboxyfluorescein as analytes, but no spacer compound. External voltages were 120 V (upstream) and 40 V (downstream). Initially, fluorescein and 6-carboxyfluorescein are focused in adjacent zones. After 70 seconds, acetate, which has an ionic mobility in between that of fluorescein and 6-carboxyfluorescein, arrives and spaces the two compounds. The fluorescein zone remains focused at the depletion zone border, while the 6-carboxyfluorescein zone is pushed away in upstream direction by the continuously broadening acetate zone. Spacer addition enables baseline separation of fluorescent compounds enabling more precise identification and quantification. Furthermore, a single compound or a specific group of compounds can be selectively transported away from the depletion zone and can eventually be eluted from the system, while other compounds remain at their near-stationary position at the border of the depletion zone. Advantageously, all compounds remain focused during this process. Thus, spacer addition is a powerful method for purification and transport.

4.4.5 Positional stability

A crucial feature of dzITP is the positional stability of the depletion zone border. A near-stationary condition is reached after a rather short period, typically in the order of 100 seconds (see Figure 4.2), in which depletion rate and EOF velocity reach a balance. A discrete injection experiment was performed with 50 µmol/L of both fluorescein and 6-carboxyfluorescein; external voltages were 120 V (upstream) and 40 V (downstream). In this experiment, the depletion zone border shifted less than 700 µm in 1 hour. A previous report on nanofluidic concentration devices indicated a near-zero shift after 3 hours of actuation[65], although under different experimental conditions, indicating that the result reported here could be further optimized. However, the near-stability of the isotachophoretic separations demonstrated here greatly enhances monitoring of focusing and separation processes by microscopy without x/y control of the microscope stage. Additionally, the experimental time range is much larger than for non-stationary ITP methods, allowing higher concentration factors to be achieved.

4.4.6 Three-point voltage actuation

In 4.3 we demonstrate the versatility that is provided by a three-point voltage actuation approach. In Figure 4.3a and b the magnitude of the upstream and downstream voltages was varied, while maintaining the ratio between them. This enables tuning of the extent to which analytes are focused. For low voltages the two zones are barely distinguishable, while for high voltages sharp edges of the zones can be observed. Figure 4.3b shows normalized slope values in fluorescence intensity per µm. The results suggest a linear trend between voltage magnitude and zone sharpness. Analyte zone positions are not greatly influenced by a change of the voltage magnitude as long as the ratio between upstream and downstream voltages is kept constant. In principle this enables a free choice of the maximum field strength and resulting focusing strength. However, small shifts

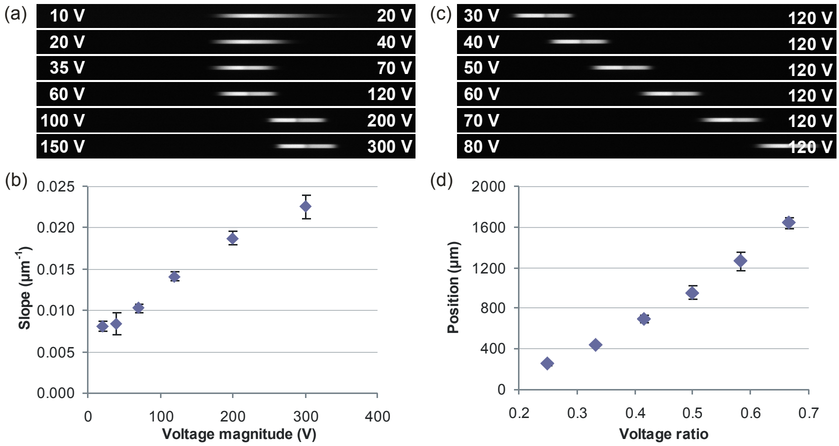

Figure 4.3 Three-point voltage actuation. a) Focusing and separation of fluorescein and 6-carboxyfluorescein at several voltage magnitudes. b) Dependence of focusing strength on the voltage magnitude. Focusing strengths are represented by the steepness of the slopes between the fluorescein plateau and the depletion zone; voltage magnitudes are represented by the upstream voltage. c) Fluorescein and 6-carboxyfluorescein zones at different ratio's between upstream and downstream voltages. d) Distances of the edge between the depletion zone and the fluorescein zone from the nanochannel. Measurements were triplicated and randomized.

in analyte zone positions are observed at higher voltage magnitudes. We measured maximum shifts of 364 ± 21 µm. In Figure 4.3c and d the voltage ratio is varied by means of the downstream voltage. The zones can be shifted over a range of 1.4 mm by varying the voltage ratio between 0.25 and 0.67 (downstream voltage : upstream voltage). Zone positions appear to relate rather linear to the voltage ratio. Separations are maintained, although at increasing ratios defocusing occurs. The 1.4 mm zone shift is accompanied by a decrease of slope values in the order of 0.006 µm^{-1}.

Complete control over analyte zone position and sharpness is a crucial and unique advantage of dzITP over conventional ITP methods. In conventional methods, a single stable position can be obtained by EOF balancing, but during the experiment this position can not be easily changed without changing parameters like pH or electrolyte concentrations. Contrarily, in dzITP this is easily done by tuning the upstream and downstream voltage magnitudes. Real-time image analysis of fluorescent markers can be used as feedback input for three-point voltage actuation, enabling automated zone positioning control. Moreover, great benefit is offered to experimental readout, as analyte zones can be scanned in a precisely controllable manner by steering them along a sensor.

Table 4.1 Comparison of dzITP with conventional ITP methods and nanofluidic concentration devices (NCD). ✓= intrinsic or standard possibility; - = not possible or not demonstrated in literature; m = possible with modification.

Property	ITP	NCD	dzITP
analyte focusing	✓	✓	✓
separation of ions	✓	-	✓
spacer insertion	✓	-	✓
single electrolyte	-	✓	✓
near-stationary	m	✓	✓
voltage controlled zone positioning	-	-	✓

4.4.7 Synergy of dzITP

Table 1 summarizes the synergy that emerges from the combination of ITP and nanofluidic concentration devices, as provided by dzITP. Except for the requirement of multiple electrolytes, dzITP has all key characteristics of ITP: focusing towards plateau concentrations and separation into adjacent zones that are ordered according to ionic mobility. Spacer compounds can be used to segregate adjacent zones. From nanofluidic concentration devices, dzITP takes the single-electrolyte advantage, as well as positional stability. Three-point voltage actuation adds to this synergy the possibility of precise control of focusing strength and zone positioning.

4.5 Conclusion and Outlook

In this paper we have demonstrated isotachophoretic separations employing a nanochannel-induced depletion zone as a trailing electrolyte. dzITP requires only a single background electrolyte to be injected and can be performed easily with both discrete and continuous injections. We demonstrated separations of up to four compounds in clearly distinguishable zones within 100 seconds. A spacer was inserted to improve baseline separation of fluorescent compounds, and to induce selective transport of analytes while maintaining sharply focused zones. Moreover, full control over analyte position and zone sharpness was demonstrated using the unique three-point voltage control of dzITP. Scanning of analyte zones using three-point voltage actuation will enable simple integration of sensors such as surface-enhanced Raman spectroscopy (SERS), surface plasmon resonance (SPR), and conductimetry or electrochemical detection. As dzITP is much easier to use than conventional ITP, integration into a microfluidic platform for everyday laboratory use will be very attractive, as exemplified by the Agilent 2100 Bioanalyzer for on-chip capillary electrophoresis. Integration in hand-held analysis devices, as has been recently done for conventional ITP[144], may find interesting applications in water quality monitoring, explosive detection, point-of-care screening, etc. Future research focuses on coupling of the technique to sampling and detection modules. We see great potential for dzITP in our metabolomics research, particularly for the extraction, preconcentration and quantification of low-abundant metabolites from small complex biological samples. Thanks to its unique combination of voltage-controlled versatility and single-electrolyte simplicity, dzITP holds the promise to become a core component in the electrokinetic chip-based platforms of the future.

4.6 Acknowledgements

We thank Marcel Hesselberth, Daan Boltjes (Leiden Institute of Physics, Leiden University), Jiajie Li (LACDR, Leiden University) and Stefan Schlautmann (MESA+, Twente University) for helpful discussions and support with device fabrication. We thank Richard van den Berg (Leiden Institute of Chemistry, Leiden University) for assistance on the synthesis of FITC-labeled amino acids and Raphaël Zwier (Fine-Mechanical Department, Leiden University) for constructing the chip interface. This project was financed by the Netherlands Metabolomics Centre, the Netherlands Genomics Initiative and the Netherlands Organization for Scientific Research (NWO).

4.7 Appendix

4.7.1 Additional movies

Several movies are available in the electronic supporting information online with the publication belonging to this chapter[174]: Movie 1: dzITP-separation after a discrete injection of four compounds: fluorescein, FITC-leucine, 6-carboxyfluorescein and FITC-glutamate. Movie 2: Discrete injection of fluorescein and 6-carboxyfluorescein combined with a continuous injection of acetate as a spacer. Movie 3: Fluorescein and 6-carboxyfluorescein zones are positioned by using different ratios between upstream and downstream voltages.

4.7.2 Chip fabrication

Photoresists (SU 8-10 and ma-P 1275) and developers (mr-Dev 600 and ma-D 331) were obtained from Microresist Technologies (Berlin, Germany). N-methylpyrrolidone (NMP) was obtained from Rathburn Chemicals (Walkerburn, Scotland). AbsorbMax^{TM} film, fuming nitric acid (100%) and hexamethyldisilazane (HMDS) were obtained from Sigma-Aldrich (Steinheim, Germany). Chips containing micro- and nanochannels were fabricated in 4” Pyrex® wafers (Si-Mat, Kaufering, Germany). The wafers were spin coated with SU 8-10; the wafer was first accelerated to 500 rpm in 5 seconds to allow resist spreading, directly followed by an acceleration to 2000 rpm in 5 seconds, which was maintained for 30 seconds. After spin coating, the resist was allowed to settle for 8 hours at room temperature, after which the resist was prebaked using a hotplate by controlled heating to 95 °C in 8 minutes, followed by ambient cool down. The resist was exposed at 6 mW/cm^2 for 25 seconds in a Suss MA 45 mask aligner (Karl Suss KG, München-Garching, Germany) in which a Hoya UV34 filter (LG optical, Churchfield, UK) was installed to prevent SU 8 T-topping. During exposure AbsorbMax film was attached to the back side of the wafer, to prevent undesired reflections. The microchannel pattern was transferred using a 5” chromium mask (Delta Mask, Enschede, The Netherlands). A post-exposure bake was done by controlled heating to 95 °C in 8 minutes, followed by ambient cool down. Development was done for 3 minutes in mr-Dev 600 developer followed by washing in isopropanol and demineralized water. Using the developed SU 8 resist as a mask, microchannels were etched into the glass wafers by a 1 hour deep reactive ion etching (DRIE) step. DRIE was performed in an Oxford Plasmalab 90+ parallel plate reactor (Oxford Instruments, Abingdon, United Kingdom) using an argon/SF6 plasma. Gas flows were 20 sccm for argon and 25 sccm for SF6. After establishing a stable plasma at 10 mTorr, pressure was set at 2 mTorr. Forward power was 200 W. After etching, the SU 8 resist was stripped by placing the wafers in NMP for several hours at 70 °C, followed by removal of remaining particles in a fuming nitric acid bath. The wafers were rinsed in water, spin-dried, and baked for 5 minutes at 110 °C for dehydration. The wafers were spin coated with HMDS followed by a curing bake at 150 °C for 5 minutes. Next, ma-P resist was spin coated at 1000 rpm for 30 seconds preceded by 10 seconds of acceleration. The resist was prebaked for 5 minutes at 95 °C. Transfer of the nanochannel pattern was performed by an exposure step as performed as described above. Development was done with ma-D 331 developer for 5 minutes. To etch the nanochannels, DRIE was performed with same parameters as described above, except for the etch time, which was 100 seconds. The ma-P resist was stripped with acetone. Resulting micro- and nanochannel depths were 1.7 µm and 60 nm respectively, as measured with a Dektak 150 profilometer (Veeco, Tucson, AZ) and by scanning electron microscopy using a FEI Nova^{TM} NanoSEM apparatus (FEI, Hillsboro, OR). Each etched wafer was bonded with a second pyrex® wafer. In these wafers, fluidic access holes were ultrasonically drilled using a diamond bit. Both wafers were subsequently cleaned in acetone, piranha acid and nitric acid, followed by a 1 minute dip in KOH. A pre-bond was realized upon application of manual pressure, after which direct bonding was performed in an oven (Model P320, Nabertherm GmbH, Lilienthal, Germany). The temperature was ramped to 600 °C in 3 h, which temperature was maintained for 4 h, followed by cooling to room temperature with a rate of 50 °C/h. After bonding, wafers were not diced, a whole wafer was used from which a single chip was selected.

4.7.3 Analyte zone identification by standard addition

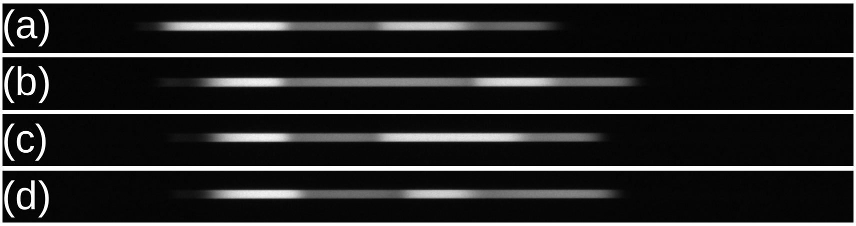

Figure 4.4 Analyte zone identification by standard addition. In each experiment, the four analytes (fluorescein, FITC-leucine, 6-carboxyfluorescein and FITC-glutamate) were present in concentrations of 30 µmol/L, except for the analyte to be identified, which had a concentration of 60 µmol/L. Discrete injections were performed. From left to right, the four zones were identified as follows: a) first zone: fluorescein; b) second zone: FITC-leucine; c) third zone: 6-carboxyfluorescein; d) fourth zone: FITC-glutamate.

CHAPTER 5

From SERS to SERSOR: Investigation of PEG-thiol coatings to make a dynamic Surface-Enhanced Raman Scattering sensOR[a]

5.1 Abstract

A surface enhanced Raman spectroscopy (SERS) substrate, when improved with a coating inert towards the analyte but thin enough to allow surface enhancement of analytes in solution, can operate without irreversible adsorption taking place and can therefore be responsive to changes in analyte concentration as opposed to conventional SERS substrates. The range of use of this powerful detection technique can then be significantly expanded to include re-use, cleaning and calibration. Ultimately this concept of dynamic SERS can provide a chemical sensor, or SERSOR, that not only detects but also identifies unlabeled (bio)analytes in applications such as process monitoring or as a non-invasive detector in-line with separations such as HPLC, or especially, in Lab-on-a-Chip and µTAS systems. Described in this chapter are first measurements of a SERSOR, a SERS active substrate coated with self-assembled monolayers (SAM) of oligo(ethylene glycol) terminated thiol (PEG-SH). Consecutive measurements of water and adenine solutions, a molecule known for its irreversible adhesion, demonstrated no reversibility of adenine signal for the uncoated SERS substrates whereas the coated substrate demonstrated an initial adenine signal reversibility of 90%. Although adequate robustness of the sensor was not yet obtained, the device represents a first step towards the envisioned SERSOR concept.

---

[a] K. G. H. Janssen, S. J. Trietsch, Z. Liu, H. J. van der Linden, J. P. Abrahams and T Hankemeier. Published Patent Application: K.G.H. Janssen and T. Hankemeier, US20130050694 A1.

5.2 Introduction

5.2.1 Surface-enhanced Raman scattering (SERS)

SERS is a detection technique based on Raman scattering, where detection limits of analytes are improved by the proximity of a metal surface, typically silver or gold. The surface features of the metal, typically in the order of tens of nanometers such as for a rough metal surface or for separate nanoparticles or metal colloids[175], supports surface plasmons that when exited by an incident Raman photon induce a very strong localized field. This increases the Raman signal from molecules near the surface, typically within 10 nm[176]. Several recent books and reviews dedicated to SERS are available focusing on practical applications as well as the theoretical understanding of the phenomenon[176–183]. SERS provides a combination between molecular structural information from vibrational spectroscopy, with sensitive label-free detection. The ability of SERS to measure and identify many unlabeled biomolecules including for example glucose, enkaphalin, thrombin and adenine at excellent detection limits allows in principle its application in the biomedical field[182,184,185]. SERS was also successfully applied for off-line detection after various analytical separation methods[186].

Silver and gold irreversibly adsorb many molecules due to their inherent negative surface charge[187,188], particularly the molecules with thiol and amine groups. This adsorption ensures the close proximity of these compounds to the enhancing surface, improving detection limits as molecules accumulate onto the surface over time. However, such irreversible adsorption also has important disadvantages:

1) Substrates cannot be re-used. Therefore calibration is not possible with the same substrate, obstructing quantitative measurements if the substrate characteristics vary.

2) Dynamic measurements in solution are not possible. The signal increases over time until the surface is saturated, and the analytes can be only detected as an integrative signal. Upon a change of the solution composition the signal does not , as opposed to what would be desirable in e.g. chemical process monitoring or for an in-line detection. A measurement therefore does not reflect the current composition of SERS-active compounds in the solution but depends on the whole history of the substrate.

3) Simultaneous detection and identification of multiple analytes is in principle possible with SERS when yielding vibrational spectra that allows them to be differentiated, supported possibly by chemometrics. Irreversible adsorption may obstruct this, due to surface competition between analytes or between analytes and non-SERS active components of the sample matrix.

4) The measurements are invasive. Adsorption implies the extraction of compounds from the measurement solution so that the sample cannot be recovered for a further analysis. In-vivo applications will be invasive as well (even if the adsorption would be reversible).

These four aspects limit the current application of SERS substrates for single-use invasive measurements, and cause it to be at most as an integrative detector, which may be quantitative only if the substrate can be reproducibly manufactured (but used as disposables) and there are no competition effects due to a complex sample composition.

5.2.2 Strategies so far for SERS implementation

Although many processes can already be monitored with Raman spectroscopy, an enhanced detection limit in dynamic process monitoring would be of great value[189]. SERS can provide enhanced detection limits but since the desirable strongest SERS enhancements are achieved by binding to the surface, at the same time this imposes a large constraint on their applicability. Adhesion leads to fouling, restricting the sensor to single use, preventing calibration, in-line use and dynamic measurements. Secondly SERS substrates in a complex mixture are subject to surface competition between analytes and/or matrix compounds, making SERS enhancement strongly susceptible to matrix effects. These challenges have been recognized from the beginning of SERS, and development of a means for dynamic quantitative SERS measurements has been a dominant driving force in SERS substrate development. Several strategies attempt to enable quantitative measurements as well as their limitations are listed below.

The most popular strategy is the reproducible manufacturing of substrates, as this allows measurements with separate but identically performing substrates. A multitude of methods has been applied in manufacturing substrates[190], from colloid deposition[191–200], roughening a flat metal surface electrochemically[201,202], using direct nanofabrication[203] and microfabrication techniques to create an appropriate scaffold for the metal[204–209] in combination with e.g. sputtering and vapor deposition techniques. One SERS substrate yielding reproducible enhancements is commercially available (Klarite ™, D3 Technologies Ltd. UK). Re-use of substrates or dynamic measurements are not possible with this strategy, nor does it offer a solution for the surface competition between analyte and sample matrix and/or other analytes.

A strategy to allow SERS detection in the presence of a complex matrix has been to use surface coatings that have a strong binding preference with the analyte of interest. Such coatings selectively enrich the analyte near the surface as opposed to matrix compounds. This principle was applied in e.g. qualitative protein measurements[210,211] immuno-assays[212] and anthrax markers[213]. A rarely reported coating type which however is of interest for our approach is what can be called unselective enrichment coatings. These coatings have an interaction similar to retention mechanisms as used in reversed phase high performance liquid chromatography (RP-HPLC), and may therefore be potentially reversible and interact with a range of compounds. One work using such a coating reports measurements on benzene and tert-butylbenzene aqueous solutions with n-alkanethiols, on substrates coated with 1-propanethiol (C3) up to octadecanethiol (C18)[214] , although rinsing or reuse was not reported. The only use as a reversible coating in an actual separation was demonstrated with a coating of 1-propanethiol, in GC analysis[215] and as the stationary face in LC for BTEX (benzene, toluene, ethylbenzene, and o-, m-, and p-xylene)[216]. The only downside of this coating approach is that since it may interact reversibly with multiple analytes the affinity and hence signal enhancement is very dependent on the matrix. Hence surface competition occurs when used during a separation, or after. Another coating type uses a coating of reporter molecules, which have a strong inherent SERS signal and high affinity for the analyte of interest. Analyte-induced conformational changes on the coating are measured, allowing indirect detection of the analyte. Reporter molecule coatings have been applied to e.g. Cu^{2+} and Pb^{2+}[217], pH[218–220], lactate[221] and viruses[222]. *In-vivo* experiments have been performed with this approach and include measurements of glucose in rats[200,223] and intracellular pH[224–226]. A review on SERS in cells is also available[227]. With the appropriate coating the binding between analyte and reporter molecule may be reversible, allowing dynamic measurements. In practice this may solve the challenge for a dynamic quantitative SERS substrate, but for one or a few selected compound(s) only. Unfortunately thus, the high selectivity of enrichment when using reporter coatings excludes the capability for the measurement of multiple constituents of a complex mixture. This capability is needed e.g. for a generic detector for SERS active analytes after a separation of unknown compounds. Furthermore the requirement for binding makes these coatings invasive *in-vivo*.

5.2.3 SERS as a sensOR: the SERSOR concept.

We propose to overcome the main constraint on the broad application of SERS by means of a dense coating that is inert towards the analyte(s). This prevents adsorption of compounds and endows the SERS substrate with the ability for dynamic detection with the signal reflecting the concentration. By default this prevents bias from surface competition. Also, this changes the substrate from a disposable into a re-usable one. Most importantly, such a coated substrate may be tested and evaluated before use, or even calibrated. For such a SERS-sensOR device we propose the name SERSOR.

Since SERS enhancement greatly diminishes with distance from the metal surface[177–181], the coating must be as thin as possible, preferably thinner than 10 nm[176]. Since we will measure compounds in solution instead of enriched on the surface of the uncoated substrate this will result in lower detection limits. The properties of the various SERS strategies so far compared to each other and the proposed SERSOR are summarized in Table 5.1.

A SERSOR will have a broad potential in applications such as process monitoring or as a non-invasive detector in-line coupled with separations such as HPLC. As the signal originates from within a few tens of nanometers from the surface, applications include the monitoring of highly localized process in (bio)-chemical reactions[228], relevant for *in-vivo* measurements.

Table 5.1 Properties of the various types of coated SERS substrates (see section 5.2.2). **Analyte** Indicates selectivity of the substrate. **Detection limit** General/average indication, or in case of selectivity vs. intended analyte only. *Depends on the coating thickness. **No surface competition** ”No” indicates that the coating does not disable competition for the surface (either temporarily or permanent) **Dynamic** Whether the SERS response may respond to changes in solution over time, e.g. composition and concentration. †May be dynamic if the affinity is reversible: e.g. pH sensitive reporte coating[224–226]. **Quantitative** Wether the SERS response can be calibrated to reflect concentration. ‡Potentially if the total amount adhering is fixed by selecting the volume of solution e.g. dried (non-dynamic) or: if the accumulation over time from solution can be calibrated.

	Uncoated	Reporter coating	Selective Enrichement coating	Unselective enrichement coating	SERSOR
Analyte	All SERS active	Target compound only	Target compound only	Potentially multiple	All SERS active
Detection limit	Excellent	(Very) good	Good*	Average*	Average*
No Surface competition	No	Yes (Target compound)	Yes (Target compound)	No	Yes
Dynamic	No	Potentially†	Potentially†	Yes	Yes
Quantitative	Potentially‡	Potentially‡	Potentially‡	No	Yes

As SERS is an inherent nanoscale effect, it is well suited for downscaling of analytical systems. A coating, such as for a SERSOR, is not expected to increase the difficulty of downscaling SERS. Therefore, downscaling a SERSOR is primarily a microfabrication challenge for the substrate itself. Of particular interest is that a SERSOR can be implemented in lab-on-a-chip (LOC) and µTAS systems, a field in which the potential for SERS has already been recognized[34].

5.2.4 SERSOR development

Substrates based on silver colloid deposition provide the strongest SERS enhancement[184]. Since it is the target of our research to evaluate a coating for a SERSOR, and not to develop a SERS substrate, an established method of colloid deposition on glass was selected to prepare the SERS substrate[195].

A good candidate for a SERSOR coating, reported to be inert towards biological molecules such as proteins, is a self assembled monolayer (SAM) of oligo(ethylene glycol) terminated thiols (PEG-SH)[229] on gold and silver[230]. Coverage results of coating protocols using PEG-SH have been studied as a function of metal surface roughness[231] and for different solvents[232]. Interestingly, two types of thickness and surface coverage for PEG-SH coatings have been reported in relation with SERS, a dense 25 nm, PEG-SH coating (5 kDA) to block out the environment[233], and a very disperse coverage with a different PEG-SH on colloids to stabilize the particles in solution while explicitly keeping the surface accessible[234]. Neither method is suited for a SERSOR as an optimum thickness and coverage is required in between. However, this research did establish that the complete PEG-SH coating did not appear to influence normal biological behavior in-vivo[233], making a SERSOR compatible with *in-vivo* measurements. In a different field, particular PEG-SH coatings with low molecular weights ($<$750 Da) have been reported to provide a surface coverage dense enough to inhibit the etching of flat gold in an aqueous cyanide etch bath[235]. Notably, thiol based coatings have been reported to adhere more slowly to silver than to gold[236]. In conclusion, PEG-SH may prevent molecules from adsorbing to the surface but can be made thin enough to allow SERS of molecules in solution. It however needs to be evaluated on our non-flat silver substrate.

The goal of this paper is to prove the concept of a SERSOR using an PEG-SH coating on a SERS-active substrate. The investigation will focus on the questions whether this particular coating applied on silver surfaces is sufficiently inert, and dense to prevent small biomolecules from adsorbing while at the same time thin enough to allow sensitive SERS.

5.3 Experimental

5.3.1 Chemicals

Silver nitrate 99.9999%, Sodium Citrate, 3-aminopropyltrimethoxysilane (APTMS), adenine, sulphuric acid and hydrogen peroxide were acquired from Sigma Aldrich (Sigma Aldrich, Zwijndrecht, The Netherlands). Deionized water (DI-water) used was generated by a Milli-Q ®Gradient A10 ®(Millipore, Amsterdam, The Netherlands). When very pure solvent was required, water and MeOH were of UL-CMS grade (Biosolve, Westford, USA). Isopropanol and acetone were obtained from VWR (BASF, VLSI Selectipur grade). Oligo(ethylene glycol) terminated thiol ($CH_3-O-[CH_2-CH_2-O]_3-[CH_2]_5-SH$) was a kind gift from Dr. Nicole Botterhuis(department of supramolecular polymer chemistry, Eindhoven University, The Netherlands). Standard microscope slides were obtained from Menzel (Menzel GmbH & Co. KG, Braunschweig, Germany). SERS measurements were performed with an aqueous solution of 10 mmol/L adenine.

5.3.2 Raman instrumentation

Measurements were performed using a RAMANRXN1® Microprobe (Kaiser Optical Systems Inc., Ecully, France) controlled with the included Holograms®software, equipped with a solid state laser, 785 nm at 200 mW. The Raman system was integrated with an Olympus BX51 microscope with a 60x water immersion lens (Olympus Corporation, Zoeterwoude, The Netherlands). The microscope was equipped with a high-accuracy xyz positioning stage (SCAN IM 120x100, 1 mm lead screw pitch, linear encoders, Märzhäuser Wetzlar GmbH & Co. KG, Wetzlar, Germany) driven by a Corvus high-resolution positioning controller and the included software Winpos (miCos GmbH, Eschbach, Germany). Spectra were acquired by summation of three 1 second acquisitions, with the immersion lens in the analyte solution, focused on the surface of the SERS substrates. Data (pre)processing and analysis of spectra was performed using Matlab (The MathWorks Inc., Natick, USA). A scanning electron microscope (SEM) (Nova 200 NanoSEM, FEI Company™, Hillsboro, USA) was employed to image the colloid distribution on the surface.

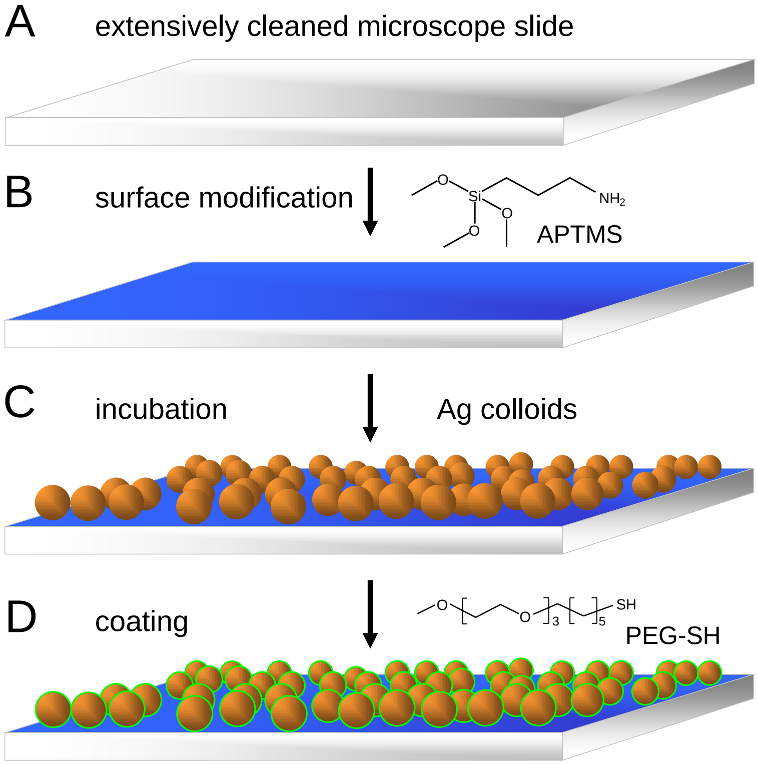

Figure 5.1 SERSOR manufacturing steps. (A) An extensively cleaned microscope slide (B) was modified with 3-aminopropyltrimethoxysilane (APTMS), prior to (C) incubation with a Ag hydrosol to ensure a strong adhesion of the colloids. (D) This SERS-active substrate was then coated with PEG-SH.

5.3.3 SERSOR manufacturing.

A citrate-reduced silver hydrosol was made in ULCMS grade water[237] and its SERS activity confirmed by measurement of adenine (results not shown). These silver colloids were then immobilized onto a microscope slide using the procedure as detailed by Park et al.[195], shown schematically in Figure 5.1A-C. Briefly, microscope slides were cleaned thoroughly by wiping with a tissue and household dish washing soap solution followed by extensive rinsing with DI-water. For further cleaning the slides were then placed in an ultrasonic bath in acetone and then MeOH for 10 minutes each and dried for 20 min at 110 ℃ in an oven to remove organic solvent. After evaporation of all solvent the slides were submerged in piranha solution ($H_2O_{2:}H_2SO_4$ 1:3 v:v for several days (Caution! Piranha acid is very corrosive and potentially explosive upon contact with organic substances. Appropriate safety measures should be taken while handling) to both clean and activate the surface. Afterwards the slides were rinsed with water and stored in MeOH (both ULCMS grade) awaiting further processing. The slides were rinsed with isopropanol and placed in a solution of 8% APTMS in isopropanol (v:v) for 21h. After rinsing with isopropanol the APTMS was annealed on the slides at 110 ℃ in an oven. The trimethoxy silyl group of APTMS reacts with the activated glass surface, and the amine group then present a positive surface charge towards the solution at neutral pH. This positive surface charge facilitates a strong adhesion between the inherently negative Ag colloids[187,188] and the slides. The slides were incubated in undiluted silver hydrosol for 1 day on an orbital shaker, followed by rinsing with water (ULCMS grade). SERS substrates were coated by submersion in an aqueous 1 mmol/L PEG-SH solution for 1 day. Afterwards the coated substrates were rinsed with and stored in water (ULCMS grade), prior to measurements. Uncoated SERS substrates were retained in water (ULCMS grade) for reference measurements.

5.4 Results & Discussion

5.4.1 SERSOR manufacturing

SERS active substrates were successfully produced and coated with PEG-SH. The colloid density on the microscope slides was studied with scanning electron microscopy (SEM) (Figure 5.2). The manufacturing method was relatively quick and simple but the colloid density was found to be inhomogeneous over the microscope slide. The colloid density was found to correlate positively with the SERS signal strength and observed scattering of the laser from the surface. In practice, the laser scattering was successfully used to locate strongly enhancing sites rapidly without analyte, by moving the SERS substrate under the laser spot and observing the reflection intensity by eye.

5.4.2 SERSOR measurements

A SERSOR needs to demonstrate reversibility in analyte signal, in order to measure concentration changes in a dynamic manner. To evaluate the effectiveness of the coating for this purpose, the biomolecule adenine was selected as a test analyte. Adenine has a strong SERS signal and normally adheres irreversible to a silver surface[238], and is therefore a challenging analyte for a SERSOR.

The PEG-SH coated SERS substrate successfully demonstrated surface enhancement of Raman detection of adenine. This was established by placing a solution of 10 mmol/L of adenine on the SERS substrate and measuring the signal with the Raman microscope focused on the surface through the solution using an immersion objective. While with a bare glass slide only, adenine could not be detected, while it was clearly detectable with the SERS substrate.

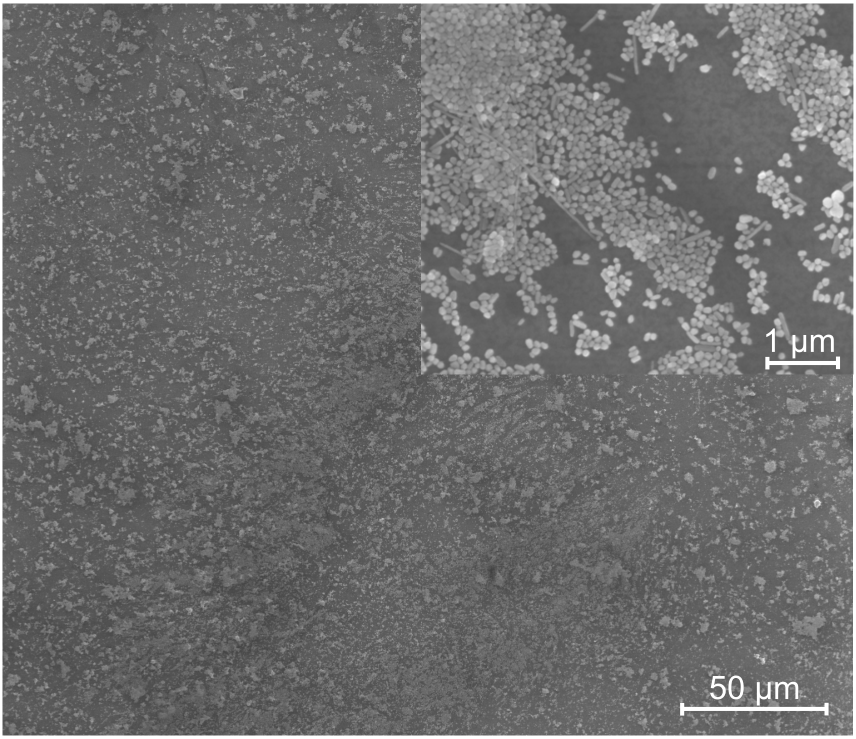

Figure 5.2 SEM image of a SERS substrate coated with PEG-SH. The image shows an area of 300 x 300 µm with the surface covered with silver colloid clusters, associated with the strong enhancements from these locations. The insert shows that clusters are on average 1-2 layers of colloids thick and several microns in size. Also present are silver nanowires several microns in length and tens of nanometers wide.

Subsequent SERS measurements of water, a solution of 10 mmol/L adenine, and after intermediate rinsing with water, again water, were acquired for coated and uncoated SERS substrates. The uncoated SERS substrate showed no significant reduction in signal of adenine after even very extensive rinsing with DI-water (data not shown), as has been previously reported in literature[238]. The spectra of a set of consecutive measurements from an identical position for the PEG-SH coated SERS substrate are shown in Figure 5.3.

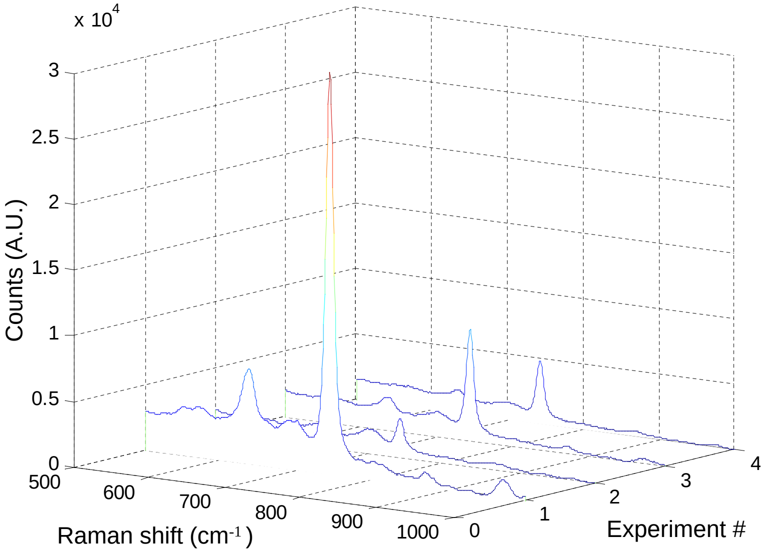

Figure 5.3 Subsequent SERS measurements of adenine and DI-water at an identical surface position of an PEG-SH coated substrate. Experiment No. 1 corresponds to adenine (10 mmol/L), No. 2 DI-water, No. 3 reapplied adenine (10 mmol/L) and No. 4 DI-water. The most intense band, characteristic for adenine, is apparent at 734 cm^{-1}

The PEG-SH coated substrate demonstrated an initial reduction of adenine signal of almost 90% after rinsing with water. When the substrate was exposed again to adenine, the signal of adenine returned (albeit weaker), and was reduced again by rinsing (albeit not entirely). It can be concluded that the coating prevented the irreversible adsorption of adenine to the SERS substrate and was thin enough to allow SERS, as opposed to other PEG-SH coatings that were intentionally thick to obstruct SERS signals from beyond the coating[233]. The positive identification of adenine, while limiting its irreversible adsorption to the SERS substrate demonstrates the feasibility of the SERSOR concept.

As can be seen from the measurement series of Figure 5.3, with consecutive measurements a reduced intensity of the adenine signal and increased carry-over was seen. Immersion in DI-water for 1h as well as extensive rinsing did not affect the carry-over signal strength. This indicates that adenine was attached to the silver and therefore the coating did not completely prevent adsorption to the SERS substrate. The increasing carry-over signal of adenine (Figure 5.3, measurements No. 2 and No. 4) may therefore be explained by decreasing coverage of the coating on the SERS substrate.

The reduced response to adenine during the experiment (Figure 3, experiment No. 1 and No. 3) is a typical result and found in other measurement series we performed, but it is less readily explained, particularly since with uncoated SERS substrates no loss of signal was found, despite rinsing efforts. In further investigation of this observation it was found that the signal of PEG-SH itself, although unaffected by storage for extensive periods in water, is strongly affected by laser exposure for sub-second periods, much shorter than the order of the acquisition time used. We hypothesize that the apparent wear of the coating with consecutive measurements (Figure 5.3), is due to the reaction of silver with the thiol group of the coating, accelerated by irradiating with the laser. This corresponds to silver tarnishing, the well known reaction of silver with sulphur groups, such as in H_2S and SO_2, forming the characteristic black silver sulfide (Ag_2S), known to affect the surface plasmon resonance of silver[239,240]. Although this particular effect is of potential interest for tarnishing studies of silver, it is beyond the scope of this paper and the kinetics were too fast to evaluate effectively with our setup.

5.4.3 Perspectives

For the purpose of the development of a robust SERSOR, improving the present colloid coating protocol is needed in coverage and reproducibility, although colloid coatings of similar quality as we show in Figure 5.2 have been reported[241]. Notably, in a later stage we achieved much improved colloid substrate manufacturing, with a homogeneous colloid distribution and correspondingly a maximum variation in surface signal intensity by a factor of 2. A SEM image of this surface is provided in the appendix Figure 5.4. Unfortunately these new substrates could not yet be tested with the SERSOR coating. A different SERS substrate may also be used, e.g. Klarite, or one of the many other strategies to manufacture substrates (See introduction for a selection reported in literature). A reproducible substrate would enable quantification of the effect of the coating on SERS enhancement. In addition, it will be of interest to study the effect of a coating on the SERS activity of the different surface geometries provided by the various SERS substrate manufacturing methods. Also, the influence of these variations on the coating effectiveness or its application procedure may be investigated.

The particular coating used here for a SERSOR, i.e. thiol chemistry to coat silver, potentially induces unwanted effects. To solve these problems, gold substrates could be used, or a coating relying on other binding principles could be considered such as amine, which also adheres to silver.

For future SERSORs, no single coating can be expected to block the interactions in all applications as the interactions depend on the analyte(s) of interest and its matrix. Therefore, as each application field imposes a different condition on inertness, different customized coatings need to be developed. These can be based on polymers, metals or oxides. A successful SERSOR coating will require optimization of the surface coverage, stability and thinness of the coating on a SERS-active substrate. Lastly the potential of a SERSOR for downscaling is not limited by the coating but manufacturing of the substrate. With state of the art technology we expect that a SERSOR can be integrated in µTAS and Lab-on-a-Chip systems.

5.5 Conclusions

A proof of concept for a dynamic surface enhanced Raman sensor, a so-called SERSOR, was demonstrated. An initial reversibility of the signal of 90% was achieved by coating a SERS active substrate with a non fouling coating that was inert and thin. The coating, PEG-SH, was evaluated with the biologically relevant molecule adenine, a normally strong binding molecule to silver whose signal could not be reduced by rinsing with water. Although further optimization of the coating is needed, this proof-of-concept opens the way for the development of appropriate coatings for applications requiring the measuring of unlabeled (bio)molecules in process monitoring in large reaction vessels, as well as detection in-line with separations in systems, potentially as small as µTAS or lab-on-a-chip.

5.6 Acknowledgements

We gratefully acknowledge prof. Age K. Smilde (University of Amsterdam) for access to the Raman spectrometer. We acknowledge Ing. Marcel Hesselberth from the Department of Condensed Matter Physics, Leiden University, The Netherlands, for measuring the SEM images. We also would like to thank Dr. Nicole Botterhuis, department of supramolecular polymer chemistry, Eindhoven University, The Netherlands, for her kind gift of the PEG-thiol. We acknowledge support from NanoNed and from the Netherlands Metabolomics Centre (NMC) which is a part of The Netherlands Genomics Initiative/Netherlands Organization for Scientific Research.

5.7 Appendix

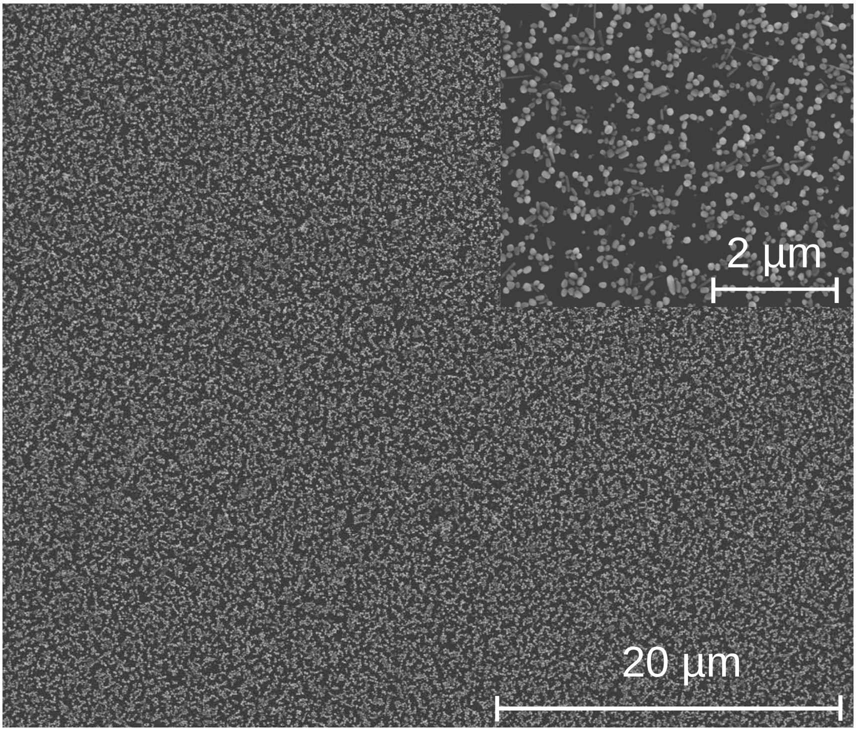

Figure 5.4 SEM image of a SERS substrate. The image shows an area of 50 x 50 µm with the surface covered with silver colloids and fused silica. A much larger area, ≈ 1x1mm showed the same coating state.

CHAPTER 6

Summary, Conclusions & Perspectives

6.1 Goal of the thesis

Metabolomics holds the promise to understand mechanisms of health and disease, by means of elucidating the role of metabolic processes involved. This understanding in turn can accelerate drug development and enable personalized medicine. The proper study of metabolomics however, requires cheaper and faster methods. Additionally, sometimes metabolomics will require the analysis of small to ultra-small samples, such as from single cells, which currently is not at all possible with conventional lab equipment. Ultimately, in order to understand the dynamic processes in the metabolic state of an entire human, an organ, tissue or a cell, time resolved studies will be required, taking samples of body fluids in a longitudinal manner or, when studying individual cells, at the level of individual cells.

A Lab-on-a-Chip platform in principle allows integration of complex separation methods in a miniaturized fashion and in that manner provides a standardized and automated analysis at reduced time and analysis costs. Such an efficient, standardized analysis platform could be also designed to allow the analysis of small sample volumes of complex samples such as a blood droplet to acquire information on the metabolome. Analyzing ultra-small samples volumes such as that of an individual cell, or an aliquot of an individual cell, then requires even further miniaturization.

Miniaturization towards the microscale will also allow sample volumes much smaller than possible with current conventional lab equipment, and it may enhance the resolving power of separations. However, this may require new analytical approaches and not only down-scaling of existing methods. Actually, microfluidics analysis systems are increasingly described in literature, and a few are commercially available, which handle volumes on the order of nanoliters (10^{-9} L).

Analysis on the sub-cellular scale, which is on the order of sub-picoliters ($<10^{-12}$ L) is rarely described in literature and not commercially available yet. For this purpose nanochannels, intrinsically small enough for sub-picoliters, hold great promise. Nanochannels are not just smaller channels; many of their properties are still unknown, making their study, nanofluidics, a fascinating field of research. Electrophoretic separation techniques provide a greater resolving power compared to LC separations, and become even more effective upon downscaling. Notably an electrophoretic separation technique with a very high separation potential is isotachophoresis.

The goal of this thesis is the exploration of nanofluidics for the analysis of minute metabolomic samples in miniaturized analysis devices. In this exploration we included the study of phenomena unique to nanofluidics. This understanding was used not only to bypass side effects while exploring the limit of miniaturization of isotachophoresis, but also to exploit them by the hyphenation of microfluidic ITP with nanofluidic phenomena.

6.2 Solution acidification in nanochannels, a surface charge model

In Chapter 2, the discovery of the unexpected dominant acidity of glass in nanochannels is described. This led to advanced modeling of the electrochemical double layer. The knowledge gained on nanochannels can be used to avoid unwanted titration effects in nanoscale analysis, or to possibly exploit them. The titration model can be used as a tool to study further fundamental nanochannel properties. For instance, in a follow-up of this work the effect of polymers on the surface of a nanochannel was studied by Anderson et al.[242] and recently used to study the influence of energetic surface heterogeneity on proton desorption during capillary filling of silica nanochannels by Piasecki et al.[243] Secondly, it offers the unique opportunity to study the titration of solutions without adding co-ions to the solution and resulting changes in ionic strength, e.g. from chlorine in HCl and sodium in NaOH, as the counter ion is a stationary group on the surface. This titration effect has since even been shown to allow actuation by an externally applied potential on the channel surface to actuate proton release and uptake, and titrate the filling solution[244].

This titration effect may be relevant for all applications in nanofluidic chips where changes in solvent composition occur. Particularly, it has implications for various separation methods when applied in nanochannels: for example in liquid chromatography often solvent gradients are used, and in electrokinetic methods such as field-enhanced sample stacking or isotachophoresis which are based on discontinuities in solvent composition. On the other hand this model can support the understanding of large scale applications that utilize surface interface effects and interactions occurring at the nanoscale, including for instance open-tubular liquid chromatography in nanochannels.

Based on the insights obtained in Chapter 2, new approaches are also possible for the analytical method isoelectric focusing (IEF). Conventionally, this method separates amphoteric analytes, e.g. proteins, by an axial pH gradient. This gradient is imposed by adding a mixture of amphoteric background molecules. The constituents of this mixture are selected such that a continuous range of isoelectric points is present and that each of the compounds have a strong pH buffering capability. The in- and outlet of the channel or capillary are then placed in vials corresponding to the pH extremes of the ampholytes. When an electric field is applied over this mixture, the ampholytes migrate until they have reached a position where their net charge is zero, so that they are ultimately arranged on the order of their isoelectric point. This mixture is generally referred to as carrier ampholytes. Ampholitic analytes such as proteins, stop migrating at the position where the pH corresponds to their isoelectric point. This process simultaneously separates and concentrates these compounds. Unfortunately, the presence of carrier ampholytes can be unwanted or impractical, e.g. in combination with detection methods such as mass spectrometry. As a future prospect to exploit the nanochannel titration effect, the wall buffer capacity in a nanochannel can be used to perform isoelectric focusing (IEF). Nanochannels strongly buffer pH and do so inversely proportional to their channel depth. Potentially a nanochannel with slopes from deep to shallow may therefore induce a pH gradient, from low to high pH respectively, buffered by the wall. If so, such a nanochannel could enable IEF without any carrier ampholytes. The technology needed to make sloping channels with a continuous gradient is to our knowledge not available at this time. A stepped slope ($\approx$ 10 nm step size) however has been demonstrated[245], so selective trapping of compounds in batches may be attempted. A different approach could be the capping of the silanol groups in a standard non-tapered microfluidic or conventionally capillary channel, in a gradient from less to more capping to also achieve a buffer capacity gradient.

The model implicitly describes the charge asymmetry in solution (the number of protons released) in the nanochannel on the surface charge in charges per nm^2, as a function of pH and ionic strength. This in turn can allow prediction on the rate of filtration in membranes[246] and may be used to predict concentration polarization as used in depletion zone isotachophoresis (Chapter 5).

6.3 Isotachophoresis in nanochannels for sub-pL injection volumes

In Chapter 3 nanochannels were used for isotachophoretic separations of 0.2 and 0.4 pL samples to assess the limits of miniaturization. The developed setup demonstrated the feasibility of advanced separations and fluidic control on the nanoscale. The ITP separation was actually achieved for the smallest sample volume so far reported in the literature.

The feasibility of ITP in nanochannels is important for metabolomic analysis of minute sample amounts. ITP, being a focusing technique, can substantially improve detection limits, a crucial aspect for the challenging detection of very low abundant compounds. ITP can simultaneously be considered a sample pretreatment technique, purifying analytes while separating them in their respective zones. Nanochannels in turn can maximize the resolving power of ITP. So in case of low sample amounts, perhaps counter-intuitively, the minute nanochannels can improve detection limits by improving resolution. Of course in nanochannels, detection techniques are challenging and some optical ones even impossible to use, but detection limits are imposed by the amount of analyte and not by the channel dimensions.

With the feasibility of nanochannel ITP established, in the future this technology can be developed and applied for the downscaling of several micro capillary and microfluidic analysis techniques. Possible other techniques of interest for further downscaling are hyphenated separation strategies such as ITP-CZE, transient ITP etc. It should be noted that with the demonstrated feasibility of nano-ITP, the application of the method is not limited to samples from single cells only. A targeted approach for one or a few compounds only is of value in many applications that involve rare or expensive compounds. The reported nano-ITP method can then contribute in two straightforward ways. Firstly, for a targeted analysis of one or a few compounds that are available in very low absolute amounts, using the advantage of enhanced separation that ITP in nanochannels offers. Secondly, for the analysis of intrinsically small volumes or small amounts which can be analyzed with nanochannel ITP after a first separation step, which can be achieved with zone electrophoresis, ITP or another separation technique.

At first glance, the minute size of nanochannels may not appear appealing for separations from the perspective of current standard sample volumes and world to chip interfacing challenges. In practice however, loadability of larger initial sample volumes in ITP is conventionally achieved by initiating the separation in a large cross-section while converging inline into a smaller one. This process takes longer but the final resolution is demonstrated to be independent of its history (at the same field strengths), and most importantly the resolution is independent of the original sample volume[60,247]. For the envisioned minute sample amounts ITP can then be started in a (large) microchannel (or capillary, or both, providing multiple steps as needed) converging to a final nanochannel cross-section.

This process will allow for potential sample dilution (from sample pretreatment often required for proper sample handling or hyphenated techniques) or simply for much larger sample sizes that contain a very low amount of the compound of interest. Effectively this means that the nanochannel ITP demonstrated here shows the potential for the analysis of 40 attomole of an analyte, regardless whether the original sample volume was 1 µL or 0.4 pL.

In this thesis ITP was successfully performed in a nanochannel in the presence of a biomatrix. A next step in the application of metabolite profiling can be the analysis of an individual cell. Although the injected volume was 400 fL, the injection was carried out from a larger sample volume because of the dead volume still present in the set-up. Therefore, integration of the sampling procedure and handling on the chip prior to analysis is crucial when analyzing ultra-small samples of less than 1 pL as mentioned in the previous paragraph. The proof of concept of nanoscale ITP was achieved for two labeled amino acids and fluorescent detection. For the analysis of a larger set of analytes in a complex sample however, such as needed for metabolomics of a single cell, the separation has to be coupled to a suitable detection technique. The addition of both very small-scale sampling and detection techniques will determine also the way how to set up the ITP separation. Fluorescence is probably the most suited detection technique at this scale; another candidate, investigated in this thesis is surface enhanced Raman spectroscopy (See Chapter 1).

A limit on miniaturization of ITP, in terms of maximum potential was unexpectedly imposed by a newly discovered nanofluidic phenomenon: electrocavitation[120]. It was discovered that a water column can be broken in a controlled manner in a nanochannel, with negative pressures developing on the order of -2000 bar. The feasibility to use nanochannels as a platform for controlled cavitation studies is currently underway. Positive pressures have also been realized, by straightforwardly reversing the polarity of the voltage, to the limit of breaking the bonding between bottom and top substrate in the chip, delaminating them. Potentially counter intuitively, micro and nanochannels may handle very high pressures: $>$ 1400 bar[248]. This is because pressure is force per area, so that with the very small surface area the force is relatively low. The realization that huge pressures, potentially exceeding 1400 bar, are possible in nanochannels without any pumps is particularly interesting for ultra-high pressure liquid chromatography (UHPLC) applications. Pumps based on the related principle of electro-osmotic flow are actually commercially available from several sources e.g. Dolomite Microfluidics, UK. Normally the application of UHPLC is limited by availability and cost of pumps and interfacing, with currently pressures of up to 1200 bar available, whereas the aforementioned large pressures are developed inside the nanochannels and require in principle no pressure interfacing to the outside world at all. In addition nanochannels, due to their high surface-to-volume ratio are an ideal open-tubular platform for LC[19–21]. This hyphenation of very high pressures and nanochannel open-tubular LC could therefore yield ultra-high pressure open-tubular/nanochannel liquid chromatography.

6.4 Depletion zone Isotachophoresis

In Chapter 4 the advantages of hyphenating microfluidics and nanofluidics for isotachophoretic separations was investigated, which led to the discovery of a new powerful separation method: depletion zone isotachophoresis (dzITP). This microfluidic separation method utilizes a nanochannel/microchannel interface to generate concentration polarization, forming an ion depletion zone in the microfluidic channel. This depletion zone acts similar to a trailing electrolyte allowing the performance of isotachophoresis with a single electrolyte.

dzITP is of high value in metabolomic sample analysis as it inherits from ITP the double function of being both a sample pretreatment and/or purification technique as well as a focusing and separation technique. In addition, its gradient focusing aspect grants a significant greater control of the analyte zone position, while the depletion zone removes the need for a trailing electrolyte. The need for only a single electrolyte adds a very important degree of freedom and experimental simplification to ITP, increasing its applicability.

The focusing abilities of dzITP, on one hand depend on the leading electrolyte, a feature which has been extensively modeled and described for conventional ITP[60,247]. On the other hand it depends on the formation of a depletion zone at the interface of a single nanochannel with a microchannel as has also been investigated and modeled[50,157]. The latter study shows that the rate of depletion zone growth is linear in time at constant current, $\Delta L_{depletion} \approx t$, or as time squared for constant voltage, $\Delta L_{depletion} \approx t^2$. This means that the nanochannel pumps ions at a constant rate over time, and hence that the charge asymmetry over time does not change in the nanochannel, so that the pumping property of the nanochannel can be described with a single value. As already mentioned, an estimate of this value can be based on the model provided in Chapter 2, which allows the charge asymmetry in solution in the nanochannel to be calculated, in charges per nm^2, as a function of pH and ionic strength. This knowledge would for instance allow tuning the EOF in the microchannel to a maximum value while just maintaining the depletion zone, to maximize the accumulation of analytes in, and the sharpness of the focused zones. Still, despite these available pieces of the puzzle and its potential benefits, the combined fundamental principle of dzITP remains to be studied and modeled in more detail.

The electric field in the depletion zone vs. the EOF determines its function similar to a trailing electrolyte, and can be considered therefore to be a very relevant subject for study. In practical applications, if the electric field is known, the mobility cut-off value of the depletion zone can be described in analogy to the trailing ion and assigned a value in terms of a ”virtual” electrophoretic mobility. Also, the field strength in the depletion zone not only depends on fixed parameters such as the channel geometry and chosen parameters such as pH and ionic strength, but also on parameters which can be adjusted such as the applied potentials. Particularly relevant is the field along the microchannel, which determines the EOF, vs. the field over the nanochannel towards ground, which determines the depletion rate per unit time. That means that the value of the depletion zone's ”virtual” electrophoretic mobility may be modulated (and in fact changed under constant potential actuation) by setting the voltages and monitoring the current. More preferably the current is actuated directly as it translates directly into the ionic fluxes. Compared to conventional ITP, where the trailing ion is selected, dzITP would have the added advantage of what is defined here as virtual mobility actuation. Once the current and voltages have been calibrated, the need for visual confirmation or monitoring is not any more needed. This will be relevant for when optical access is impractical, e.g. when the channels are not accessible or compounds do not fluoresce, and particularly for integration with non optical detection techniques such as mass spectrometry.

A more direct mode of selective release for dzITP, effectuated by locally and/or temporarily collapsing the depletion zone, has been demonstrated in our group[249], by leveraging the voltages so that the bulk flow elutes past the depletion zone at a length of focused zone per unit time. This process can be pulsed so that a select length of analyte zone may be released, or controlled so that a specific length per unit time is released. The instability of this process was overcome and tunable release was achieved by means of visual monitoring. Interestingly when elution has been matched to the slowest compound (the compound that focuses nearest the depletion zone), it is no longer focused itself (its flux along the depletion zone is now the same as along the whole channel) and it has taken over the role from the depletion zone as the trailing ion.

Although dzITP reported here uses bulk flow from EOF alone, which is practical as pumps are not needed, this feature is not required, and the combination of EOF with pressure flow would enable all field strengths to be applied over the nanochannel, resulting in a simplified system with a potentially faster analyte focusing speed. Likewise, dzITP is not limited to a depletion zone made at a nanochannel/microchannel interface[68] but its principles should also hold for a depletion zone made by other means, adding to the versatility of the technique, which remains to be fully explored. For instance, with bipolar electrode focusing, where the depletion zone is locally induced by electrodes in the channel[69], also plateau concentrations as function of the background electrolyte concentration were reported, but apparently not considered associated with ITP by the authors. Another example by which a depletion zone focusing was induced is by means of a Nafion membrane, replacing the nanochannel[71], or placed locally on the bottom of a microchannel[72]. In a functionally analogous system, the depletion zone function may also be fulfilled by an organic phase as in electroextraction[250]. Although the EOF is absent in such a system, when the electrolyte into which the ions are extracted is chosen to be a leading electrolyte vs. the desired analytes, the lower mobility ions will focus at the interface, and ions faster than the leading ion will merely stack and travel onwards, creating a cutoff filter for high-mobility ions.

In experiments using just a single nanochannel (during our studies on electrocavitation) a focused analyte plug was maintained at constant position in a long nanochannel under influence of an applied field. It is tentatively hypothesized that this is a fundamental form of dzITP. The EOF in the single nanochannel, like in dzITP provides a net transport of negative analytes towards the cathode down the nanochannel, but is met from the other end by a depletion zone forming at the anode from nanochannel concentration polarization, with focusing at the interface: single nanochannel dzITP (K.G.H. Janssen et al, manuscript in preparation).

6.5 Surface enhanced Raman spectroscopy

In Chapter 5 the first results of a surface enhanced Raman spectroscopy sensor (SERSOR) are reported. In contrast to conventional SERS, dynamic analyte detection can be performed as a coating protects the surface from irreversible binding and/or fouling, while it is thin enough to allow SERS. This strategy is unconventional as it creates a distance between analyte and surface and forgoes the standard drying of the sample on the substrate. Since the measurement is performed in solution, its detection limits are much higher than reported in conventional SERS for dyes. We believe this disadvantage to be more than offset however by the ability to perform Raman spectroscopy at an improved detection limit and to perform dynamic measurements of biological compounds in solution.

A SERSOR has significant potential in miniaturized metabolomic analysis, or bioanalysis in general. Firstly, as it provides vibrational spectra, a SERSOR also supports identification of unlabeled biomolecules while it is more sensitive than Raman alone. Secondly, by its nature as a surface detection technique it detects analytes within only tens of nanometers (Eq 1.9) from its surface, and by its concentration sensitivity (the coating ensuring that the signal predominantly originates from solution), it is intrinsically compatible with minute volume and/or low abundant compound detection.

Although of interest for inline detection or process monitoring in general, including detection in microchannels, the potential advantages of a SERSOR may stand out most as an inline detector for miniaturized separation techniques, particularly for concentration-driven techniques such as ITP or dzITP. Before the SERSOR can fully prove its potential, two aspects need to be improved. First of all, the coating stability needs to be improved beyond the first results reported in Chapter 5, preferably with the new generation of improved colloid coated substrates that has already been achieved (section 5.7). For this purpose a coating based on amine binding to the silver should be evaluated, because the coating inspired by gold coating chemistry, which was based on a thiol group, has likely reacted with the silver upon irradiation, damaging both surface and coating and contributing to the poor initial robustness observed. Secondly the SERSOR needs to be implemented in a micro- or nanochannel. Fortunately, a promising process that may integrate a SERS surface in small channels was already demonstrated, in a nanochannel, in the form of silver mirrors for a Fabry-Perot interferometer manufactured into the side walls of the nanochannel[251].

6.6 Roadmap for nanofluidic tools in metabolomics and bioanalysis

Within bioanalysis in general and metabolomics in particular, the need for miniaturized sample analysis challenges analytical methods and instrumentation. In answer, nanofluidic tools can address these challenges.

Developing a method for metabolomic analysis for samples down to those from a single cell, has proven to be a tremendous multidisciplinary challenge. Ultrasmall volumes have to be handled, which requires working in nanochannels. However, analytical approaches in nanochannels require full understanding of processes originating from the significant surface/volume ratio, for example theoretical modeling of silicon oxide surface chemistry. For the analysis of small volumes, isotachophoresis is a promising analytical method. Designing a nanofluidic chip allowing isotachophoresis of 400 fL injection volumes has proven to be a challenge which can ultimately be solved. It was found that development of a fluidic setup to provide the macro- to nano-interfacing of the fluidic, optical and electrical connections is required to realize such a device. Such a development is actually often neglected. Also, the development of an automated and standardized protocol and the design and manufacturing of devices to allow this is crucial, and requires at the nanofluidic level much attention.

In the described research nanofluidics has been established as a platform capable of supporting the handling of the low sample amounts required for single-cell analysis and for the achievement of separations. Still, single-cell metabolomics can only be realized if the envisioned nanofluidic platform allows integration of sampling, separation and detection steps. As a consequence the following next research steps are: 1) Developing of non-invasive cell-sample extraction on-nanochip or at least compatible with introducing the sub-cellular sample volume into a nanochannel. A device with these properties has been demonstrated by J. Emmelkamp et al.[252]; 2) Interfacing the analysis device with a label-free detection method of metabolites such as mass spectrometry or SERS. If the detection method provides sufficient detection limit, but requires fully resolved compounds, the techniques of transient ITP or ITP-CZE can be considered. Other than these aspects, the required know-how of nanofluidics, interface engineering and separation methods is now available.

We expect that the successful performance of metabolomics down to the single cell level, will grant insight not only into the cell on its own but also its workings as smallest functional component of an organism. The understanding of individual cells is fundamental in processes such as developmental biology from stem cell to tissue or even embryo to organism. A single cell metabolomics method will not only be useful for those cells that are rare or unique but it will for the first time allow the validation of studies that relied so far on the averaging of many cells. The search for mechanisms and pathways relevant in apoptosis, cancer, diabetes, and neuronal diseases could be significantly accelerated if these processes can be investigated in a time resolved manner at the individual cell level. Nanofluidics can greatly contribute to providing the tools for applications like these in metabolomics, not just by the use of smaller channels with lower volume, but since knowledge of fundamental nanofluidic phenomena can help in designing novel analytical approaches, whether at the nanoscale or larger, as was demonstrated in this thesis.

Bibliography

1. A. Deyati, E. Younesi, M. Hofmann-Apitius, and N. Novac, Drug Discovery Today **18**, 614 (2013).
2. G. F. Wu and E. Alvarez, Neurologic Clinics **29**, 257 (2011).
3. R. Hargreaves, Headache **47**, S26 (2007).
4. H. A. van Wietmarschen, Ph.D. thesis, Leiden/Amsterdam Center for Drug Research, Leiden University (2012).
5. J. J. Kamphorst, Ph.D. thesis, Leiden University (2010).
6. A. M. Henney, Embo Reports **10**, S9 (2009).
7. J. van der Greef and R. N. McBurney, Nature Reviews Drug Discovery **4**, 961 (2005).
8. J. van der Greef, S. Martin, P. Juhasz, A. Adourian, T. Plasterer, E. R. Verheij, and R. N. McBurney, Journal of Proteome Research **6**, 1540 (2007).
9. J. de Boer, M. Boomkamp, F. Broekhuijsen, P. Cheung, M. Danz, T. Douma, K. V., M. van Oppenraay, and Schutte, eds., *Farmacotherapeutisch Kompas* (College van Zorgverzekeringen, 2013).
10. J. van der Greef, T. Hankemeier, and R. N. McBurney, Pharmacogenomics **7**, 1087 (2006).
11. T. W.-M. Fan, A. N. Lane, and R. M. Higashi, eds., *The Handbook of Metabolomics* (Humana Press, 2012).
12. W. B. Dunn, D. I. Broadhurst, H. J. Atherton, R. Goodacre, and J. L. Griffin, Chemical Society Reviews **40**, 387 (2011).
13. M. M. Koek, F. Bakels, W. Engel, A. van den Maagdenberg, M. D. Ferrari, L. Coulier, and T. Hankemeier, Analytical Chemistry **82**, 156 (2010).
14. P. Nemes, A. M. Knolhoff, S. S. Rubakhin, and J. V. Sweedler, Acs Chemical Neuroscience **3**, 782 (2012).
15. O. Yanes, Nature Chemical Biology **9**, 471 (2013).
16. R. Trouillon, M. K. Passarelli, J. Wang, M. E. Kurczy, and A. G. Ewing, Ana-

lytical Chemistry **85**, 522 (2013).
17. D. C. Harris, *Quantitative Chemical Analysis* (W. H. Freeman, 2011).
18. M. Noga, F. Sucharski, P. Suder, and J. Silberring, Journal of Separation Science **30**, 2179 (2007).
19. S. Vankrunkelsven, D. Clicq, D. Cabooter, W. De Malsche, J. G. E. Gardeniers, and G. Desmet, Journal of Chromatography A **1102**, 96 (2006).
20. X. Wang, J. Kang, S. Wang, J. J. Lu, and S. Liu, Journal of Chromatography A **1200**, 108 (2008).
21. G. Desmet and S. Eeltink, Analytical Chemistry **85**, 543 (2013).
22. N. J. Petersen and S. H. Hansen, Electrophoresis **33**, 1021 (2012).
23. E. V. Mosharov and D. Sulzer, Nature Methods **2**, 651 (2005).
24. Y. F. Cheng and N. J. Dovichi, Science **242**, 562 (1988).
25. S. C. Terry, J. H. Jerman, and J. B. Angell, Ieee Transactions On Electron Devices **26**, 1880 (1979).
26. A. Manz, N. Graber, and H. M. Widmer, Sensors and Actuators B-chemical **1**, 244 (1990).
27. D. Janasek, J. Franzke, and A. Manz, Nature **442**, 374 (2006).
28. P. Vulto, S. Podszun, P. Meyer, C. Hermann, A. Manz, and G. A. Urban, Lab On A Chip **11**, 1596 (2011).
29. Fluidigm, *Chips and kits* (2013).
30. A. Floris, S. Staal, S. Lenk, E. Staijen, D. Kohlheyer, J. Eijkel, and A. van den Berg, Lab On A Chip **10**, 1799 (2010).
31. S. M. Nie and S. R. Emery, Science **275**, 1102 (1997).
32. D. J. Harrison, K. Fluri, K. Seiler, Z. H. Fan, C. S. Effenhauser, and A. Manz, Science **261**, 895 (1993).
33. L. Chen, J. E. Prest, P. R. Fielden, N. J. Goddard, A. Manz, and P. J. R. Day, Lab On A Chip **6**, 474 (2006).
34. A. Arora, G. Simone, G. B. Salieb-Beugelaar, J. T. Kim, and A. Manz, Analytical Chemistry **82**, 4830 (2010).
35. G. B. Salieb-Beugelaar, G. Simone, A. Arora, A. Philippi, and A. Manz, Analytical Chemistry **82**, 4848 (2010).
36. J. R. Kraly, R. E. Holcomb, Q. Guan, and C. S. Henry, Analytica Chimica Acta **653**, 23 (2009).
37. R. B. Schoch, J. Y. Han, and P. Renaud, Reviews of Modern Physics **80**, 839 (2008).
38. W. Sparreboom, A. van den Berg, and J. C. T. Eijkel, Nature Nanotechnology **4**, 713 (2009).
39. M. L. Kovarik and S. C. Jacobson, Analytical Chemistry **81**, 7133 (2009).
40. L. N. Geng, P. Jiang, J. D. Xu, B. Q. Che, F. Qu, and Y. L. Deng, Progress In Chemistry **21**, 1905 (2009).
41. H. Daiguji, Chemical Society Reviews **39**, 901 (2010).
42. J. C. T. Eijkel and A. van den Berg, Microfluidics and Nanofluidics **1**, 249 (2005).
43. J. Haneveld, H. Jansen, E. Berenschot, N. Tas, and M. Elwenspoek, Journal

of Micromechanics and Microengineering **13**, Natl Inst R&D Microtechnol (2003).

44. F. Detobel, V. Fekete, W. De Malsche, S. De Bruyne, H. Gardeniers, and G. Desmet, Analytical and Bioanalytical Chemistry **394**, 399 (2009).
45. M. Kato, M. Inaba, T. Tsukahara, K. Mawatari, A. Hibara, and T. Kitamori, Analytical Chemistry **82**, 543 (2010).
46. S. Pennathur and J. G. Santiago, Analytical Chemistry **77**, 6772 (2005).
47. S. Pennathur and J. G. Santiago, Analytical Chemistry **77**, 6782 (2005).
48. A. J. Bard and L. R. Faulkner, *Electrochemical Methods, Fundamentals and Applications* (John Wiley & Sons, Inc., New York, USA, 1980).
49. Q. S. Pu, J. S. Yun, H. Temkin, and S. R. Liu, Nano Letters **4**, 1099 (2004).
50. T. A. Zangle, A. Mani, and J. G. Santiago, Chemical Society Reviews **39**, 1014 (2010).
51. Q. Yu and Z. Silber-Li, Microfluidics and Nanofluidics pp. 1–9 (2011).
52. F. Kohlrausch, Annalen der Physik und Chemie **298**, 209 (1897).
53. F. Everaerts, J. Beckers, and T. P. Verheggen, *Isotachophoresis: theory, instrumentation, and applications*, Electrophoresis Library 1 (Elsevier Scientific Publishing Company, Amsterdam, Hoboken, USA, 1976).
54. C. J. Holloway and I. Trautschold, Fresenius Zeitschrift Fur Analytische Chemie **311**, 81 (1982).
55. P. Boček, M. Deml, P. Gebauer, and V. Dolnik, *Analytical Isotachophoresis*, Electrophoresis Library 1 (Wiley-VCH, Weinnheim, Switzerland, 1988).
56. J. Pospichal, P. Gebauer, and P. Boček, Chemical Reviews **89**, 419 (1989).
57. B. Jung, R. Bharadwaj, and J. G. Santiago, Analytical Chemistry **78**, 2319 (2006).
58. T. K. Khurana and J. G. Santiago, Analytical Chemistry **80**, 6300 (2008).
59. M. Bercovici, G. V. Kaigala, C. J. Backhouse, and J. G. Santiago, Analytical Chemistry **82**, 1858 (2010).
60. S. S. Bahga, G. V. Kaigala, M. Bercovici, and J. G. Santiago, Electrophoresis **32**, 563 (2011).
61. P. A. Walker, M. D. Morris, M. A. Burns, and B. N. Johnson, Analytical Chemistry **70**, 3766 (1998).
62. V. Dolnik, S. R. Liu, and S. Jovanovich, Electrophoresis **21**, 41 (2000).
63. K. Sueyoshi, F. Kitagawa, and K. Otsuka, Journal of Separation Science **31**, 2650 (2008).
64. P. Smejkal, D. Bottenus, M. C. Breadmore, R. M. Guijt, C. F. Ivory, F. Foret, and M. Macka, Electrophoresis **34**, 1493 (2013).
65. Y.-C. Wang, A. L. Stevens, and J. Han, Analytical Chemistry **77**, 4293 (2005).
66. J. G. Shackman and D. Ross, Electrophoresis **28**, 556 (2007).
67. J. G. Shackman and D. Ross, Analytical Chemistry **79**, 6641 (2007).
68. S. J. Kim, Y.-A. Song, and J. Han, Chemical Society Reviews **39**, 912 (2010).
69. R. K. Anand, E. Sheridan, D. Hlushkou, U. Tallarek, and R. M. Crooks, Lab On A Chip **11**, 518 (2011).

70. J. Astorga-Wells and H. Swerdlow, Analytical Chemistry **75**, 5207 (2003).
71. M. Shen, H. Yang, V. Sivagnanam, and M. A. M. Gijs, Analytical Chemistry **82**, 9989 (2010).
72. S. H. Ko, Y.-A. Song, S. J. Kim, M. Kim, J. Han, and K. H. Kang, Lab On A Chip **12**, 4472 (2012).
73. R. J. Dijkstra, F. Ariese, C. Gooijer, and U. A. T. Brinkman, Trac-trends In Analytical Chemistry **24**, 304 (2005).
74. M. Fleischmann, P. J. Hendra, and A. J. Mcquillan, Chemical Physics Letters **26**, 163 (1974).
75. M. Moskovits, Reviews of Modern Physics **57**, 783 (1985).
76. M. Moskovits, Journal of Raman Spectroscopy **36**, 485 (2005).
77. K. Kneipp, H. Kneipp, I. Itzkan, R. R. Dasari, and M. S. Feld, Journal of Physics-condensed Matter **14**, PII S0953 (2002).
78. J. Han and H. G. Craighead, J. Vac. Sci. Technol. A **17**, 2142 (1999).
79. J. P. Alarie, H. A.B., S. C. Jacobsoni, A. P. Baddorf, L. Feldman, and J. M. Ramsey, in *7th International conference on miniaturized chemical and biochemical analysts systems* (2003).
80. C. K. Harnett, G. W. Coates, and H. G. Craighead, Journal of Vacuum Science & Technology B **19**, Amer Vacuum Soc; IEEE Electron Device Soc; Opt Soc Amer (2001).
81. H. Cao, Z. N. Yu, J. Wang, J. O. Tegenfeldt, R. H. Austin, E. Chen, W. Wu, and S. Y. Chou, Appl. Phys. Lett. **81**, 174 (2002).
82. N. R. Tas, J. W. Berenschot, P. Mela, H. V. Jansen, M. Elwenspoek, and A. V. den Berg, Nano Lett. **2**, 1031 (2002).
83. X. Chen, R. Ji, M. Steinhart, A. Milenin, K. Nielsch, and U. Gosele, Chem. Mater. **19**, 3 (2007).
84. M. Wang, N. Jing, C. B. Su, J. Kameoka, C. K. Chou, M. C. Hung, and K. A. Chang, Appl. Phys. Lett. **88**, 033106 (2006).
85. J. C. T. Eijkel, J. Bomer, N. R. Tas, and A. V. den Berg, Lab On A Chip **4**, 161 (2004).
86. P. Muller-Buschbaum, E. Bauer, E. Maurer, K. Schlogl, S. V. Roth, and R. Gehrke, Appl. Phys. Lett. **88**, 083114 (2006).
87. D. Mijatovic, J. C. T. Eijkel, and A. V. den Berg, Lab On A Chip **5**, 492 (2005).
88. S. Pennathur and J. G. Santiago, Analytical Chemistry **77**, 6772 (2005).
89. S. Pennathur and J. G. Santiago, Analytical Chemistry **77**, 6782 (2005).
90. S. Ahuja, *Selectivity and Detectability Optimizations in HPLC* (John Wiley & Sons, Inc., New York, 1986).
91. R. E. G. van Hal, J. C. T. Eijkel, and P. Bergveld, Adv. Colloid Interface Sci. **69**, 31 (1996).
92. S. A. Smith and W. A. Pretorius, Water Sa **28**, 395 (2002).
93. H. Diehl and R. Markuszewski, Talanta **36**, 416 (1989).
94. E. W. Washburn, Phys. Rev. Lett. **17**, 273 (1921).
95. N. R. Tas, J. Haneveld, H. V. Jansen, M. Elwenspoek, and A. V. den Berg, Appl. Phys. Lett. **85**, 3274 (2004).

96. P. W. Atkins, *Physical Chemistry* (Oxford University Press, Oxford, 1998).
97. C. G. Armistead, A. J. Tyler, F. H. Hambleton, S. A. Mitchell, and J. A. Hockey, J. Phys. Chem. **73**, 3947 (1969).
98. J. A. Davis, R. O. James, and J. O. Leckie, J. Colloid Interface Sci. **63**, 480 (1978).
99. L. Bousse, Ph.D. thesis, Twente University of Technology, Enschede (1982).
100. T. Hiemstra and W. H. V. Riemsdijk, Colloids Surfaces **59**, 7 (1991).
101. N. F. Bogdanova, A. V. Klebanov, L. E. Ermakova, and M. P. Sidorova, Colloid Journal **64**, 389 (2002).
102. D. P. J. Barz, Microfluidics and Nanofluidics **7**, 249 (2009).
103. G. Garcia-Schwarz, M. Bercovici, L. A. Marshall, and J. G. Santiago, Journal of Fluid Mechanics **679**, 455 (2011).
104. Y. J. Oh, A. L. Garcia, D. N. Petsev, G. P. Lopez, S. R. J. Brueck, C. F. Ivory, and S. M. Han, Lab On A Chip **9**, 1601 (2009).
105. N. F. Y. Durand, C. Dellagiacoma, R. Goetschmann, A. Bertsch, I. Marki, T. Lasser, and P. Renaud, Analytical Chemistry **81**, 5407 (2009).
106. R. B. Schoch, A. Bertsch, and P. Renaud, Nano Letters **6**, 543 (2006).
107. K. G. H. Janssen, H. T. Hoang, J. Floris, J. de Vries, N. R. Tas, J. C. T. Eijkel, and T. Hankemeier, Analytical Chemistry **80**, 8095 (2008).
108. J. E. Prest, S. J. Baldock, P. R. Fielden, N. J. Goddard, and B. J. T. Brown, Journal of Chromatography A **1051**, 221 (2004).
109. T. K. Khurana and J. G. Santiago, Lab On A Chip **9**, 1377 (2009).
110. A. Wainright, S. J. Williams, G. Ciambrone, Q. F. Xue, J. Wei, and D. Harris, Journal of Chromatography A **979**, 69 (2002).
111. D. J. Wang and S. Bodovitz, Trends In Biotechnology **28**, 281 (2010).
112. R. N. Zare and S. Kim, Annual Review of Biomedical Engineering **12**, 187 (2010).
113. D. Cohen, J. A. Dickerson, C. D. Whitmore, E. H. Turner, M. M. Palcic, O. Hindsgaul, and N. J. Dovichi, Annual Review of Analytical Chemistry **1**, 165 (2008).
114. R. H. Templer and O. Ces, Journal of the Royal Society Interface **5**, S111 (2008).
115. J. A. Jankowski, S. Tracht, and J. V. Sweedler, Trac-trends In Analytical Chemistry **14**, 170 (1995).
116. D. L. Taylor, E. S. Woo, and K. A. Giuliano, Current Opinion In Biotechnology **12**, 75 (2001).
117. T. C. Chao and A. Ros, Journal of the Royal Society Interface **5**, S139 (2008).
118. L. M. Borland, S. Kottegoda, K. S. Phillips, and N. L. Allbritton, Annual Review of Analytical Chemistry **1**, 191 (2008).
119. E. Oh, M. N. Hasan, M. Jamshed, S. H. Park, H. M. Hong, E. J. Song, and Y. S. Yoo, Electrophoresis **31**, 74 (2010).
120. K. G. H. Janssen, J. C. T. Eijkel, T. N. R., L. J. de Vreede, T. Hankemeier, and H. J. van der Linden, in *μTas 2011* (2011).

121. G. Nouadje, H. Rubie, E. Chatelut, P. Canal, M. Nertz, P. Puig, and F. Couderc, Journal of Chromatography A **717**, 293 (1995).
122. M. Du, V. Flanigan, and Y. F. Ma, Electrophoresis **25**, 1496 (2004).
123. C. S. Effenhauser, A. Manz, and H. M. Widmer, Analytical Chemistry **65**, 2637 (1993).
124. Y. Chen, L. J. Xu, L. Zhang, and G. N. Chen, Analytical Biochemistry **380**, 297 (2008).
125. M. Mamunooru, R. J. Jenkins, N. I. Davis, and J. G. Shackman, Journal of Chromatography A **1202**, 203 (2008).
126. Y. Chen, L. Zhang, L. J. Xu, J. M. Lin, and G. N. Chen, Electrophoresis **30**, 2300 (2009).
127. N. I. Davis, M. Mamunooru, C. A. Vyas, and J. G. Shackman, Analytical Chemistry **81**, 5452 (2009).
128. M. Pumera, Electrophoresis **28**, 2113 (2007).
129. N. J. Reinhoud, U. R. Tjaden, and J. Van der Greef, Journal of Chromatography A **673**, 239 (1994).
130. K. G. H. Janssen, J. Li, H. T. Hoang, P. Vulto, R. J. B. H. N. van den Berg, H. S. Overkleeft, J. C. T. Eijkel, N. R. Tas, H. J. van der Linden, and T. Hankemeier, Lab On A Chip **12**, 2888 (2012).
131. S. M. Kenyon, M. M. Meighan, and M. A. Hayes, Electrophoresis **32**, 482 (2011).
132. D. Kaniansky, M. Masár, J. Bielčiková, F. Iványi, F. Eisenbeiss, B. Stanislawski, B. Grass, A. Neyer, and M. Jöhnck, Analytical Chemistry **72**, 3596 (2000).
133. D. Bottenus, T. Z. Jubery, Y. X. Ouyang, W. J. Dong, P. Dutta, and C. F. Ivory, Lab on a Chip **11**, 890 (2011).
134. D. Bottenus, T. Z. Jubery, P. Dutta, and C. F. Ivory, Electrophoresis **32**, 550 (2011).
135. J. Wang, Y. Zhang, M. R. Mohamadi, N. Kaji, M. Tokeshi, and Y. Baba, Electrophoresis **30**, 3250 (2009).
136. J. E. Prest, M. S. Beardah, S. J. Baldock, S. P. Doyle, P. R. Fielden, N. J. Goddard, and B. J. T. Brown, Journal of Chromatography A **1195**, 157 (2008).
137. H. Huang, F. Xu, Z. Dai, and B. Lin, Electrophoresis **26**, 2254 (2005).
138. D. Liu, Z. Ou, M. Xu, and L. Wang, Journal of Chromatography A **1214**, 165 (2008).
139. D. Liu, M. Shi, H. Huang, Z. Long, X. Zhou, J. Qin, and B. Lin, Journal of Chromatography B **844**, 32 (2006).
140. A. Persat, L. A. Marshall, and J. G. Santiago, Analytical Chemistry **81**, 9507 (2009).
141. R. B. Schoch, M. Ronaghi, and J. G. Santiago, Lab On A Chip **9**, 2145 (2009).
142. A. Persat and J. G. Santiago, Analytical Chemistry **83**, 2310 (2011).
143. M. Bercovici, G. V. Kaigala, K. E. Mach, C. M. Han, J. C. Liao, and J. G.

Santiago, Analytical Chemistry **83**, 4110 (2011).

144. G. V. Kaigala, M. Bercovici, M. Behnam, D. Elliott, J. G. Santiago, and C. J. Backhouse, Lab on a Chip **10**, 2242 (2010).
145. F. E. Ahmed, Journal of Chromatography B **877**, 1963 (2009).
146. A. García-Campaña, L. Gámiz-Gracia, F. Lara, M. del Olmo Iruela, and C. Cruces-Blanco, Analytical and Bioanalytical Chemistry **395**, 967 (2009).
147. L. Suntornsuk, Analytical and Bioanalytical Chemistry **398**, 29 (2010).
148. M. Urbánek, A. Varenne, P. Gebauer, L. Křivánková, and P. Gareil, Electrophoresis **27**, 4859 (2006).
149. G. I. Abelev and E. R. Karamova, Molecular Immunology **26**, 41 (1989).
150. M. C. Breadmore and J. P. Quirino, Analytical Chemistry **80**, 6373 (2008).
151. M. C. Breadmore, Electrophoresis **29**, 1082 (2008).
152. M. C. Breadmore, Journal of Chromatography A **1217**, 3900 (2010).
153. S. M. Kim, M. A. Burns, and E. F. Hasselbrink, Analytical Chemistry **78**, 4779 (2006).
154. S. R. Park and H. Swerdlow, Analytical Chemistry **75**, 4467 (2003).
155. J. Astorga-Wells, S. Vollmer, S. Tryggvason, T. Bergman, and H. Jörnvall, Analytical Chemistry **77**, 7131 (2005).
156. A. Plecis, R. B. Schoch, and P. Renaud, Nano Letters **5**, 1147 (2005).
157. T. A. Zangle, A. Mani, and J. G. Santiago, Analytical Chemistry **82**, 3114 (2010).
158. K. Zhou, M. L. Kovarik, and S. C. Jacobson, Journal of the American Chemical Society **130**, 8614 (2008).
159. D. Wu and A. J. Steckl, Lab on a Chip **9**, 1890 (2009).
160. B. Scarff, C. Escobedo, and D. Sinton, Lab on a Chip **11**, 1102 (2011).
161. X. Mao, B. R. Reschke, and A. T. Timperman, Electrophoresis **31**, 2686 (2010).
162. H. Yu, Y. Lu, Y.-g. Zhou, F.-b. Wang, F.-y. He, and X.-h. Xia, Lab On A Chip **8**, 1496 (2008).
163. K.-D. Huang and R.-J. Yang, Electrophoresis **29**, 4862 (2008).
164. Y.-C. Wang and J. Han, Lab on a Chip **8**, 392 (2008).
165. L. F. Cheow, S. H. Ko, S. J. Kim, K. H. Kang, and J. Han, Analytical Chemistry **82**, 3383 (2010).
166. J. Lee and J. Han, Microfluidics and Nanofluidics **9**, 973 (2010).
167. J. H. Lee, Y.-A. Song, S. R. Tannenbaum, and J. Han, Analytical Chemistry **80**, 3198 (2008).
168. J. H. Lee, B. D. Cosgrove, D. A. Lauffenburger, and J. Han, Journal of the American Chemical Society **131**, 10340 (2009).
169. A. Sarkar and J. Han, Lab on a Chip **11**, 2569 (2011).
170. J. H. Lee, Y.-A. Song, and J. Han, Lab on a Chip **8**, 596 (2008).
171. S. H. Ko, S. J. Kim, L. F. Cheow, L. D. Li, K. H. Kang, and J. Han, Lab on a Chip **11**, 1351 (2011).
172. S. J. Kim, S. H. Ko, K. H. Kang, and J. Han, Nat Nano **5**, 297 (2010).
173. S. J. Kim, L. D. Li, and J. Han, Langmuir **25**, 7759 (2009).

174. J. Quist, K. G. H. Janssen, P. Vulto, T. Hankemeier, and H. J. van der Linden, Analytical Chemistry **83**, 7910 (2011).
175. X. Lu, M. Rycenga, S. E. Skrabalak, B. Wiley, and Y. Xia, Annual Review of Physical Chemistry **60**, 167 (2009).
176. E. C. Le Ru and E. P. G., *Principles of Surface-Enhanced Raman Spectroscopy, and related plasmonic effects* (Elsevier B.V. Amsterdam, 2009).
177. Z. J. Wang, S. L. Pan, T. D. Krauss, H. Du, and L. J. Rothberg, Proceedings of the National Academy of Sciences of the United States of America **100**, 8638 (2003).
178. K. Kneipp, M. Moskovits, and K. H., *Surface-Enhanced Raman Scattering, Physics and Applications* (Springer-Verlag Berlin Heidelberg, 2006).
179. P. L. Stiles, J. A. Dieringer, N. C. Shah, and R. R. Van Duyne, Annual Review of Analytical Chemistry **1**, 601 (2008).
180. J. P. Camden, J. A. Dieringer, Y. M. Wang, D. J. Masiello, L. D. Marks, G. C. Schatz, and R. P. Van Duyne, Journal of the American Chemical Society **130**, 12616 (2008).
181. S. J. Lee, Z. Q. Guan, H. X. Xu, and M. Moskovits, Journal of Physical Chemistry C **111**, 17985 (2007).
182. J. Kneipp, H. Kneipp, and K. Kneipp, Chemical Society Reviews **37**, 1052 (2008).
183. J. N. Anker, W. P. Hall, O. Lyandres, N. C. Shah, J. Zhao, and R. P. Van Duyne, Nature Materials **7**, 442 (2008).
184. S. Abalde-Cela, P. Aldeanueva-Potel, C. Mateo-Mateo, L. Rodriguez-Lorenzo, R. A. Alvarez-Puebla, and L. M. Liz-Marzan, Journal of the Royal Society Interface **7**, S435 (2010).
185. K. C. Bantz, A. F. Meyer, N. J. Wittenberg, H. Im, O. Kurtulus, S. H. Lee, N. C. Lindquist, S. H. Oh, and C. L. Haynes, Physical Chemistry Chemical Physics **13**, 11551 (2011).
186. R. Dijkstra, Ph.D. thesis, Vrije Universiteit Amsterdam (2004).
187. P. W. Atkins, *Physical Chemistry* (Oxford University Press, 1998).
188. R. A. Alvarez-Puebla, E. Arceo, P. J. G. Goulet, J. J. Garrido, and R. F. Aroca, Journal of Physical Chemistry B **109**, 3787 (2005).
189. J. Workman, M. Koch, B. Lavine, and R. Chrisman, Analytical Chemistry **81**, 4623 (2009).
190. L. O. Brown and S. K. Doorn, Langmuir **24**, 2178 (2008).
191. B. G. Prevo, D. M. Kuncicky, and O. D. Velev, Colloids and Surfaces A-physicochemical and Engineering Aspects **311**, 2 (2007).
192. P. Jiang, C. H. Sun, N. C. Linn, B. J. Ho, and S. Venkatesh, Current Nanoscience **3**, 296 (2007).
193. T. Qiu, X. L. Wu, J. C. Shen, and P. K. Chu, Applied Physics Letters **89**, 131914 (2006).
194. R. G. Freeman, K. C. Grabar, K. J. Allison, R. M. Bright, J. A. Davis, A. P. Guthrie, M. B. Hommer, M. A. Jackson, P. C. Smith, D. G. Walter,, Science **267**, 1629 (1995).

195. S. H. Park, J. H. Im, J. W. Im, B. H. Chun, and J. H. Kim, Microchemical Journal **63**, Korean Chem Soc, Analyt Chem Div (1999).
196. T. Karakouz, A. Vaskevich, and I. Rubinstein, Journal of Physical Chemistry B **112**, 14530 (2008).
197. S. Karabicak, M. Kaya, T. Vo-Dinh, and M. Volkan, Journal of Nanoscience and Nanotechnology **8**, 955 (2008).
198. X. F. Liu, C. H. Sun, N. C. Linn, B. Jiang, and P. Jiang, Journal of Physical Chemistry C **113**, 14804 (2009).
199. A. Jamshidi, S. L. Neale, K. Yu, P. J. Pauzauskie, P. J. Schuck, J. K. Valley, H. Y. Hsu, A. T. Ohta, and M. C. Wu, Nano Letters **9**, 2921 (2009).
200. K. A. Willets and R. P. Van Duyne, Annual Review of Physical Chemistry **58**, 267 (2007).
201. D. Millo, A. Bonifacio, A. Ranieri, M. Borsari, C. Gooijer, and G. van der Zwan, Langmuir **23**, 4340 (2007).
202. J. J. Feng, U. Gernert, M. Sezer, U. Kuhlmann, D. H. Murgida, C. David, M. Richter, A. Knorr, P. Hildebrandt, and I. M. Weidinger, Nano Letters **9**, 298 (2009).
203. J. Henzie, J. Lee, M. H. Lee, W. Hasan, and T. W. Odom, Annual Review of Physical Chemistry **60**, 147 (2009).
204. G. Das, F. Mecarini, F. de Angefis, M. Prasciolu, C. Liberale, M. Patrini, and E. Di Fabrizio, Microelectronic Engineering **85**, 1282 (2008).
205. J. D. Driskell, S. Shanmukh, Y. J. Liu, S. Hennigan, L. Jones, Y. P. Zhao, R. A. Dluhy, D. C. Krause, and R. A. Tripp, Ieee Sensors Journal **8**, 863 (2008).
206. J. G. Fan and Y. P. Zhao, Langmuir **24**, 14172 (2008).
207. H. Cho, B. Lee, G. L. Liu, A. Agarwal, and L. P. Lee, Lab on a Chip **9**, 3360 (2009).
208. J. M. Baik, S. J. Lee, and M. Moskovits, Nano Letters **9**, 672 (2009).
209. N. M. B. Perney, F. J. G. de Abajo, J. J. Baumberg, A. Tang, M. C. Netti, M. D. B. Charlton, and M. E. Zoorob, Physical Review B **76**, 035426 (2007).
210. R. E. Holmlin, X. X. Chen, R. G. Chapman, S. Takayama, and G. M. Whitesides, Langmuir **17**, 2841 (2001).
211. C. D. Heyes, J. Groll, M. Moller, and G. U. Nienhaus, Molecular Biosystems **3**, 419 (2007).
212. R. Narayanan, R. J. Lipert, and M. D. Porter, Analytical Chemistry **80**, 2265 (2008).
213. K. Ryu, A. J. Haes, H.-Y. Park, S. Nah, J. Kim, H. Chung, M.-Y. Yoon, and S.-H. Han, Journal of Raman Spectroscopy **41**, 121 (2010).
214. B. J. Kennedy, S. Spaeth, M. Dickey, and K. T. Carron, Journal of Physical Chemistry B **103**, 3640 (1999).
215. K. T. Carron and B. J. Kennedy, Analytical Chemistry **67**, 3353 (1995).
216. B. J. Kennedy, R. Milofsky, and K. T. Carron, Analytical Chemistry **69**, 4708 (1997).
217. K. T. Carron, K. Mullen, M. Lanouette, and H. Angersbach, Applied Spec-

troscopy **45**, 420 (1991).

218. K. I. Mullen, D. X. Wang, L. G. Crane, and K. T. Carron, Analytical Chemistry **64**, 930 (1992).
219. J. K. Lim and S. W. Joo, Applied Spectroscopy **60**, 847 (2006).
220. X. M. Qian, J. Li, and S. M. Nie, Journal of the American Chemical Society **131**, 7540 (2009).
221. N. C. Shah, O. Lyandres, J. T. Walsh, M. R. Glucksberg, and R. P. Van Duyne, Analytical Chemistry **79**, 6927 (2007).
222. M. H. Harpster, H. Zhang, A. K. Sankara-Warrier, B. H. Ray, T. R. Ward, J. P. Kollmar, K. T. Carron, J. O. Mecham, R. C. Corcoran, W. C. Wilson,, Biosensors & Bioelectronics **25**, 674 (2009).
223. D. A. Stuart, J. M. Yuen, N. S. O. Lyandres, C. R. Yonzon, M. R. Glucksberg, J. T. Walsh, and R. P. Van Duyne, Analytical Chemistry **78**, 7211 (2006).
224. C. E. Talley, L. Jusinski, C. W. Hollars, S. M. Lane, and T. Huser, Analytical Chemistry **76**, 7064 (2004).
225. S. Zong, Z. Wang, J. Yang, and Y. Cui, Analytical Chemistry **83**, 4178 (2011).
226. J. P. Scaffidi, M. K. Gregas, V. Seewaldt, and T. Vo-Dinh, Analytical and Bioanalytical Chemistry **393**, 1135 (2009).
227. W. Xie, L. Su, A. Shen, A. Materny, and J. Hu, Journal of Raman Spectroscopy **42**, 1248 (2011).
228. D. L. Stokes, Z. H. Chi, and T. Vo-Dinh, Applied Spectroscopy **58**, 292 (2004).
229. K. L. Prime and G. M. Whitesides, Science **252**, 1164 (1991).
230. C. S. Weisbecker, M. V. Merritt, and G. M. Whitesides, Langmuir **12**, 3763 (1996).
231. J. Rundqvist, J. H. Hoh, and D. B. Haviland, Journal of Colloid and Interface Science **301**, 337 (2006).
232. D. J. Vanderah, M. L. Walker, M. A. Rocco, and K. A. Rubinson, Langmuir **24**, 826 (2008).
233. X. M. Qian, X. H. Peng, D. O. Ansari, Q. Yin-Goen, G. Z. Chen, D. M. Shin, L. Yang, A. N. Young, M. D. Wang, and S. M. Nie, Nature Biotechnology **26**, 83 (2008).
234. A. Shkilnyy, M. Souce, P. Dubois, F. Warmont, M.-L. Saboungi, and I. Chourpa, Analyst **134**, 1868 (2009).
235. N. Papen-Botterhuis, Ph.D. thesis, Technische Universiteit Eindhoven (2008).
236. A. Królikowska and J. Bukowska, Journal of Raman Spectroscopy **38**, 936 (2007).
237. P. C. Lee and D. Meisel, Journal of Physical Chemistry **86**, 3391 (1982).
238. A. Rodes, M. Rueda, F. Prieto, C. Prado, J. M. Feliu, and A. Aldaz, Journal of Physical Chemistry C **113**, 18784 (2009).
239. H. E. Bennett, R. L. Peck, D. K. Burge, and J. M. Bennett, Journal of Applied Physics **40**, 3351 (1969).
240. Y. Han, R. Lupitskyy, T.-M. Chou, C. M. Stafford, H. Du, and S. Sukhishvili,

Analytical Chemistry **83**, 5873 (2011).

241. C. Caro, C. López-Cartes, P. Zaderenko, and J. A. Mejías, Journal of Raman Spectroscopy **39**, 1162 (2008).
242. M. B. Andersen, J. Frey, S. Pennathur, and H. Bruus, Journal of Colloid and Interface Science **353**, 301 (2011).
243. W. Piasecki and R. Charmas, Adsorption-journal of the International Adsorption Society **19**, 653 (2013).
244. R. B. H. Veenhuis, E. J. van der Wouden, J. W. van Nieuwkasteele, A. van den Berg, and J. C. T. Eijkel, Lab On A Chip **9**, 3472 (2009).
245. S. M. Stavis, E. A. Strychalski, and M. Gaitan, Nanotechnology **20**, 165302 (2009).
246. J. Luo and Y. Wan, Journal of Membrane Science **438**, 18 (2013).
247. S. S. Bahga, M. Bercovici, and J. G. Santiago, Electrophoresis **33**, 3036 (2012).
248. M. T. Blom, N. R. Tas, G. Pandraud, E. Chmela, J. G. E. Gardeniers, R. Tijssen, M. Elwenspoek, and A. van den Berg, Journal of Microelectromechanical Systems **10**, 158 (2001).
249. J. Quist, P. Vulto, H. van der Linden, and T. Hankemeier, Analytical Chemistry **84**, 9065 (2012).
250. J. Stichlmair, J. Schmidt, and R. Proplesch, Chemical Engineering Science **47**, 3015 (1992).
251. K. M. van Delft, J. C. T. Eijkel, D. Mijatovic, T. S. Druzhinina, H. Rathgen, N. R. Tas, A. van den Berg, and F. Mugele, Nano Letters **7**, 345 (2007).
252. J. Emmelkamp, Ph.D. thesis, Twente University of Technology, Enschede (2007).

Samenvatting

Dit proefschrift beschrijft nieuwe en geminiaturiseerde bioanalysetechnieken voor de levenswetenschappen. De drijvende kracht hierachter is het mogelijk maken van de analyse van sub-picoliter volumes in het algemeen, en voor metabolomics in het bijzonder. Centraal staat het verkennen van nanokanalen hiervoor, wat op zijn beurt de ontdekking van nieuwe fundamentele fysisch-chemische eigenschappen in de nanofluidica oplevert.

In **Hoofdstuk 1** wordt uiteengezet hoe systeembiologie, en metabolomics in het bijzonder, een grote bijdrage kunnen leveren aan het inzicht in ziekte en gezondheid. Daarmee kan het een belangrijke impuls aan de ontwikkeling van nieuwe behandelmethodes en medicijnen geven en de efficiëntie van bestaande vergroten. Om het potentieel van metabolomics te verwezenlijken, is het van belang ook de stofwisseling op meerdere niveaus en hun interacties in kaart te brengen, waaronder in weefsels en zelfs binnen één cel. Hiervoor zijn analyses nodig die om kunnen gaan met subcellulaire volumina, ofwel kleiner dan 1 picoliter (10^{-12} L), met een dus zeer beperkt aantal analietmoleculen.

Zulke kleine hoeveelheden zijn buiten het bereik van bestaande methodes. Het Lab-on-a-Chip concept, de miniaturisatie van scheidingstechnieken in microkanalen in een zogenaamde fluïdische chip, lijkt een geschikt uitgangspunt om dit aan te pakken. Verdere miniaturisatie is dan wel nodig naar kanalen die met de gewenste ordegroottes qua volume zouden kunnen omgaan, en wel kanalen met een diepte in de orde van tientallen nanometers: nanokanalen. De praktische inzetbaarheid van nanokanalen in fluïdische chips lijkt in eerste instantie echter erg ongunstig; sterke verdunningen zijn mogelijk nodig naar minimaal microliters voor sampletransport van de buitenwereld naar het minuscule kanaal. Ten opzichte van picoliters betekent dit een verdunningsfactor van een miljoen, waarmee het voordeel van nanokanalen komt te vervallen. Daarnaast zijn nanokanalen niet zomaar kleinere kanalen, op deze schaal is sprake van een ander regime met eigen fysica en chemie; het onderwerp van het opkomende vakgebied nanofluidica.

In de introductie van dit proefschrift worden ook scheidingstechnieken geïnventariseerd. De door een elektrisch veld gedreven technieken in het bijzonder, want deze zijn intrinsiek compatibel met miniaturisatie. Een daarvan, isotachophorese (ITP) heeft als kenmerkende eigenschap dat het stoffen scheidt door ze op te concentreren in aangrenzende zones tot aan een bepaalde eindconcentratie. Voor ITP is een concentrerende factor van 1 miljoen in de literatuur gerapporteerd. Daarnaast geldt voor ITP een synergie met miniaturisatie. Dit komt doordat in kanalen met een kleinere doorsnee minder analiet-moleculen nodig zijn voor dezelfde eindconcentratie. Dit levert naar rato van miniaturisatie van de doorsnee langere zones op, wat een betere scheiding betekent. De combinatie van grote belaadbaarheid synergie met kleinere kanalen, maakt ITP een goede kandidaat voor miniaturisatie. Deze techniek is echter nog niet op nanoschaal toegepast.

Het doel van dit proefschrift is het onderzoeken van de uitdagingen en grenzen van de miniaturisatie van bioanalyses. Hiervoor zullen nanokanalen en hun eigenschappen bestudeerd worden als platform. Voor de compatibiliteit met grotere volumes zullen de grenzen van de miniaturisatie van isotachophorese verkend worden.

Hoofdstuk 2 beschrijft de ontdekking van de onverwachte dominantie van de zure eigenschappen van glas in nanokanalen. Deze eigenschap kwam naar voren bij het laten vullen van nanokanalen met vloeistof door middel van capillaire werking. De stof fluoresceïne, aanwezig in de oplossing, fluoresceert normaal zeer sterk. Het was toegevoegd om het vulproces te verduidelijken, maar was niet zichtbaar in het eerste deel van de vloeistof. Bij nader inzien bleek de fluorescente activiteit van deze stof sterk afhankelijk van de zuurtegraad (pH). Bekend is ook dat glas zwakzure silanol groepen (SiOH) aan zijn oppervlak heeft. De realisatie echter dat de hoeveelheid oppervlak ten opzichte van het volume in het kanaal, extreem genoeg kan zijn om de oplossing deels te titreren, ondanks een molair aan buffer, kan als tegenintuïtief ervaren worden. Het donkere en oplichtende deel van de vloeistof zijn te verklaren doordat de vloeistof die als eerste het kanaal instroomde werd getitreerd, waarna de vloeistof daaropvolgend een reeds van protonen uitgeputte wand tegenkwam en wel gewoon fluoresceerde. De verhouding tussen het wel en niet fluorescerende deel van de vloeistof in het kanaal bleek een maat voor de hoeveelheid protonen die per oppervlakte door de wand waren afgegeven, en de verhouding (tussen de twee delen) hing af van de hoeveelheid zouten en de pH van de oplossing.

Deze experimentele gegevens geven inzage in het gedrag van de overgangslaag tussen glas en de vloeistof; de elektrochemische dubbellaag. Hiermee kon een kwantitatief model dat het gedrag van deze elektrochemische dubbellaag beschrijft opgesteld worden. Siliciumoxides, zoals glas en kwarts, zijn een belangrijk materiaal in Lab-on-a-Chip toepassingen, en deze bevindingen zijn dan ook relevant voor de verdere miniaturisatie van microfluïdische chips, alsook voor microkanalen, capillairen, membranen, en zelfs in zand en gesteentes.

Hoofdstuk 3 beschrijft hoe met nanokanalen de grenzen van de miniaturisatie opgezocht worden door ITP toe te passen op 0.4 en 0.2 pL volumes, de kleinste volumes ooit gerapporteerd met deze techniek. Uitgevoerd in respectievelijk 20 µm bij 50 nm en 3 µm bij 330 nm kanalen. Deze volumes zijn van belang omdat deze in de orde zijn van ongeveer 5% respectievelijk 2.5% van het volume van een 25 µm doorsnee cel, of ongeveer het volume van 1 bacterie. Het sample bestond uit een oplossing van cel-extract met 2 fluorescent gelabelde aminozuren (respectievelijk 40 en 20 attomol analiet in 0.4 en 0.2 pL). In de 330 nm diepe kanalen werden de stoffen ook duidelijk geconcentreerd en gescheiden. In de 50 nm diepe kanalen lukte het opconcentreren met ITP wel maar het scheiden niet omdat de elektrische veldsterkte niet even hoog gemaakt kon worden.

Deze onverwachte grens voor de miniaturisatie van ITP werd opgelegd door een nieuw fenomeen: electrocavitatie. Afhankelijk van de elektrische veldsterkte kon de waterkolom in het kanaal gecontroleerd gebroken worden; hoe ondieper het kanaal, des te lager de benodigde veldsterkte. Een te ondiep nanokanaal legt dus een praktische grens op aan de maximale veldsterkte bij ITP, en daarmee de scheidingsefficiëntie. Op basis van een voorlopige berekening kan worden geschat dat dit veroorzaakt wordt door een onderdruk in de orde van 2000 atmosfeer. Het verkennen van de mogelijkheid om daarmee nanokanalen te gebruiken voor gecontroleerde cavitatie-experimenten is momenteel gaande. Overigens kon dit effect ook omgekeerd worden, zodat ook positieve drukken gegenereerd werden van dezelfde orde, iets wat mogelijk erg interessant kan zijn voor ultra-high pressure liquid chromatography (UHPLC) toepassingen.

In **Hoofdstuk 4** wordt de nieuwe scheidingstechniek depletiezone isotachophorese (dz-ITP) gepresenteerd. Deze techniek is een voorbeeld van de synergie van een nanofluidisch fenomeen met microfluidica (voor een uitleg over dz-ITP in detail zie sectie 1.4.4). Een nanokanaal wordt gebruikt om door middel van concentratie-polarisatie een deel van de vloeistof van de lokaal (bij de ingang naar het nanokanaal) te ontzouten. Haaks daarop loopt daar een microkanaal langs, waardoor in het microkanaal heel lokaal achtergrondbuffer wordt weggepompt en een gradiënt in zoutsterkte ontstaat, en dus in de lokale elektrische veldsterkte. Op het grensvlak tussen het ontzoutte gedeelte en de buffer vindt dan zogenaamde gradiëntopconcentrering plaats. Het ontzoutte deel vervult de rol die lijkt op die van het zogeheten trailing elektrolyt in ITP, de achtergrondbuffer fungeert dan als de leading buffer. Dit betekent dat de isotachophorese wordt uitgevoerd met slechts één elektrolyt. Dit is een groot voordeel van deze techniek, wat in de praktijk een belangrijke simplificatie en toename van de keuzevrijheid betekent. Nu beperkt een gebrek aan keuzes nog de inzet en de toegankelijkheid van isotachophorese. Deze belangrijke verbeteringen maken deze nieuwe techniek van grote waarde voor de bio-analyse, waar analyse van vaak complexe samples nodig is. Het heeft namelijk niet alleen de mogelijkheden van gewone ITP zoals techniek voor monstervoorbewerking, opzuivering en/of concentratie en scheidingstechniek. Daarnaast is, in tegenstelling tot standaard ITP, in dz-ITP de positionering statisch en is door middel van het variëren van de veldsterktes een grote controle over het systeem mogelijk. Een demonstratie van deze eigenschappen worden gegeven in het hoofdstuk.

Surface enhanced Raman spectroscopy (SERS) is een techniek waarmee op nanometers vanaf een zilveren oppervlak met grote gevoeligheid (bio)moleculen gemeten kunnen worden, van sommige stoffen is één molecuul detecteerbaar. Hierbij worden vibratiespectra gemeten, die zijn informatierijk wat betreft het molecuul en ondersteunen identificatie. Dit zijn ideale eigenschappen voor een detectieprincipe in een nanokanaal. Op dit moment is SERS op die manier niet inzetbaar: het oppervlak vervuilt en SERS wordt daarom nu ingezet voor eenmalig gebruik. Om SERS hiervoor toch inzetbaar te maken worden in **Hoofdstuk 5** de eerste resultaten van een dynamische SERS-sensor (SERSOR) beschreven. Een coating van polyethyleenglycol beschermt het oppervlak tegen irreversibele binding en vervuiling, maar is tegelijkertijd dun genoeg om analiet-moleculen dicht genoeg bij het zilver te laten voor SERS. Voordat de SERSOR zijn potentieel waar kan maken moet echter de stabiliteit van de coating-procedure worden verbeterd. Op het vlak van de coatingchemie is er daarvoor al veel kennis voorhanden. Ten tweede zal de SERSOR geïmplementeerd moeten worden in een micro- of nanokanaal. Gelukkig is er al een essentiële stap reeds gedemonstreerd in de vorm van een zilverspiegel gefabriceerd in de wanden van het nanokanaal[251] (voor een Fabry-Perot interferometer)

In **Hoofdstuk 6** wordt de inhoud van de voorgaande hoofdstukken beschouwd en worden enkele conclusies gegeven en aanbevelingen gedaan over de mogelijke vervolgonderzoeken.

Tot slot mag geconcludeerd worden dat met dit onderzoek op het vlak van fysica, chemie en platformontwikkeling een stap is gezet in het verleggen van de grenzen van bioanalyses naar de nanoschaal. Het hiervoor verkennen van nanofluidische chips heeft de analyse van het kleinste volume ooit met isotachophorese opgeleverd. De haalbaarheid van isotachophorese op deze schaal is belangrijk voor de analyse van kleine volumes in het algemeen en complexe biologische monsters zoals in metabolomics in het bijzonder. Onderweg werden ook nieuwe fysische inzichten verkregen door fenomenen die optraden in nanokanalen. Behalve nanokanalen en kennis van hun bijzondere fenomenen, zijn voor de praktische haalbaarheid van een sub-pL bioanalysemethode twee andere aspecten essentieel. Ten eerste een techniek als isotachophorese, om de noodzakelijke brug te slaan tussen de kleine volumes in een nanokanaal en de buitenwereld via welke het sample vanaf de monsterafname, doorgaans in grote volumes getransporteerd wordt. Ten tweede, de integratie van een meettechniek zoals een SERSOR die gevoelig biomoleculen in een nanokanaal zou moeten kunnen meten. Het doorontwikkelen van deze nanofluidische gereedschapsset zal een meettechniek mogelijk maken die het metabolisme en de ontwikkeling van een enkele cel kan volgen, zoals van een stamcel, neuron, of eicel.

Curriculum Vitae

Kjeld Gertrudus Hendrikus Janssen was born 1979, May 26 in Nijmegen, The Netherlands. In 1997 he completed his pre-university secondary degree (Gymnasium) at the Dominicus College, Nijmegen. That year he started studying physics at the University of Nijmegen. Following his first year (Propedeutic exam), he continued with his masters degree in biophysics. During his studies he became very impressed by the elegant, seemingly effortless complexity of Biology, particularly on the molecular and single-cell level; and became motivated to explore their workings with new methods available from developments in physics. This directed him to perform an internship (one year), on surface enhanced Raman spectroscopy (SERS) on single neural cells under the supervision of dr. R.J. Dijkstra and prof.dr. J.J. ter Meulen (Molecular and Laser Physics group), and dr. W.J.J.M. Scheenen (Department of Cellular Animal Physiology), at the University of Nijmegen. A second additional internship of half a year, was performed in France, under the supervision of dr. S. Dukic and Prof.dr. M. Manfait (Unité Médian CNRS U.M.R. 6142, University of Reims), that included measuring the distribution of the chemotherapy-drug doxorubicin between healthy and tumor brain tissue with SERS. Following his graduation, the author briefly worked as a teaching assistant for a physics course at the University of Nijmegen. Following his interest in measuring on the scale of single cells he began the work included in this thesis in November 2004 with Prof.dr. T. Hankemeier (Department of Analytical Biosciences, Leiden Amsterdam Center for Drug Research, Leiden University), in collaboration with dr. N.R. Tas and prof.dr. J.C.T. Eijkel (MESA+, University of Twente). From January 2009 to December 2011 he worked as a postdoctoral fellow in Leiden. Currently he is a projectleader in Research with Medimate B.V. a company that developed and markets a Lab-on-a-Chip platfrom for point of care tests, including the concentration of lithium in blood.

Publications

Kjeld G. H. Janssen, Hanh T. Hoang, Jan Floris, Jeroen de Vries, Niels R. Tas, Jan C. T. Eijkel and Thomas Hankemeier.
Solution Titration by Wall Deprotonation during Capillary Filling of Silicon Oxide Nanochannels. *Analytical Chemistry*, **80**, 8095–8101 (2008).

Jos Quist[†], Kjeld G. H. Janssen[†], Paul Vulto, Thomas Hankemeier and Heiko J. van der Linden. [†]*Equally contributing first authors.*
Single-Electrolyte Isotachophoresis Using a Nanochannel-Induced Depletion Zone. *Analytical Chemistry* **83**, 7910–7915 (2011).
Selected for the cover of that edition of Analytical Chemistry.

Kjeld G. H. Janssen, Jiajie Li, Hanh T. Hoang, Paul Vulto, Richard J. B. H. N. van den Berg, Herman S. Overkleeft, Jan C. T. Eijkel, Niels R. Tas, Heiko J. van der Linden, Thomas Hankemeier.
Limits of miniaturization: Assessing ITP performance in sub-micron and nanochannels. *Lab On A Chip* **12** , 2888–2893 (2012).

Kjeld G. H. Janssen, Sebastiaan J. Trietsch, Zunfeng Liu, Heiko J. van der Linden, Jan Pieter Abrahams and Thomas Hankemeier. From SERS to SERSOR: Investigation of PEG-thiol coatings to make a dynamic Surface-Enhanced Raman Scattering sensOR. In preparation for publication.

Patent

Kjeld G. H. Janssen and Thomas Hankemeier. Raman spectrometer, sensor element for a raman spectrometer and a method for obtaining a raman spectrum using the sensor element. US20130050694 A1.

Not in this thesis:

Zunfeng Liu, Federica Galli, Kjeld G. H. Janssen, Linhua Jiang, Heiko J. van der Linden, Daniël C. de Geus, Patrick Voskamp, Maxim E. Kuil, Ren C. L. Olsthoorn, Tjerk H. Oosterkamp, Thomas Hankemeier and Jan Pieter Abrahams.
Stable Single-Walled Carbon NanotubeStreptavidin Complex for Biorecognition. *The Journal of Physical Chemistry C,* **133** 4345-4352 (2010).

Peer reviewed conference contributions

Kjeld G. H. Janssen, Hanh T. Hoang, Jan Floris, Jeroen de Vries, Niels R. Tas, Jan C. T. Eijkel and Thomas Hankemeier.
Solution Titration by Wall Deprotonation During Capillary Filling of Silicon Oxide Nanochannels. *NanoBioTech Montreux,* Oral Presentation (2008).

Kjeld G. H. Janssen, Jiajie Li, Hanh T. Hoang, Niels R. Tas, Heiko J. van der Linden and Thomas Hankemeier.
Downscaling Quantitative Isotachophoresis: Limits at the sub-picoliter scale. *μTas* (2010).

Jos W. Quist, Kjeld G. H. Janssen, Heiko J. van der Linden and Thomas Hankemeier. Depletion Zone Isotachophoresis: a New Micro/nanofluidic Elektrokinetic Method. *μTas* (2010).

Kjeld G. H. Janssen, Jan C. T. Eijkel, Niels R. Tas, Lennart J. de Vreede, Thomas Hankemeier, Heiko J. van der Linden.
Electrocavitation in Nanochannels. *μTas* (2011).

Jos W. Quist, Kjeld G. H. Janssen, Paul Vulto, Heiko J. van der Linden and Thomas Hankemeier. Depletion Zone Isotachophoresis (dzITP): Beating the Simplicity of Electrophoresis. *μTas* (2011).

Kjeld G. H. Janssen, Jos Quist, Paul Vulto, Thomas Hankemeier, Heiko J. van der Linden. Single-Electrolyte Isotachophoresis Using a Nanochannel-Induced Depletion Zone. *NanoBioTech Montreux* (2011)

Kjeld G. H. Janssen, Jan C. T. Eijkel, Niels R. Tas, Lennart J. de Vreede, Thomas Hankemeier and Heiko J. van der Linden. Electrocavitation in Nanochannels. *NanoBioTech Montreux.* (2011)